UNIVERSITAT ROVIRA I VIRGILI

NEW ORGANIC ELECTROCHEMICAL SENSING PLATFORMS FOR THE POINT-OF-NEED

Adil Ait Yazza

ADVERTIMENT. L'accés als continguts d'aquesta tesi doctoral i la seva utilització ha de respectar els drets de la persona autora. Pot ser utilitzada per a consulta o estudi personal, així com en activitats o materials d'investigació i docència en els termes establerts a l'art. 32 del Text Refós de la Llei de Propietat Intel·lectual (RDL 1/1996). Per altres utilitzacions es requereix l'autorització prèvia i expressa de la persona autora. En qualsevol cas, en la utilització dels seus continguts caldrà indicar de forma clara el nom i cognoms de la persona autora i el títol de la tesi doctoral. No s'autoritza la seva reproducció o altres formes d'explotació efectuades amb finalitats de lucre ni la seva comunicació pública des d'un lloc aliè al servei TDX. Tampoc s'autoritza la presentació del seu contingut en una finestra o marc aliè a TDX (framing). Aquesta reserva de drets afecta tant als continguts de la tesi com als seus resums i índexs.

ADVERTENCIA. El acceso a los contenidos de esta tesis doctoral y su utilización debe respetar los derechos de la persona autora. Puede ser utilizada para consulta o estudio personal, así como en actividades o materiales de investigación y docencia en los términos establecidos en el art. 32 del Texto Refundido de la Ley de Propiedad Intelectual (RDL 1/1996). Para otros usos se requiere la autorización previa y expresa de la persona autora. En cualquier caso, en la utilización de sus contenidos se deberá indicar de forma clara el nombre y apellidos de la persona autora y el título de la tesis doctoral. No se autoriza su reproducción u otras formas de explotación efectuadas con fines lucrativos ni su comunicación pública desde un sitio ajeno al servicio TDR. Tampoco se autoriza la presentación de su contenido en una ventana o marco ajeno a TDR (framing). Esta reserva de derechos afecta tanto al contenido de la tesis como a sus resúmenes e índices.

WARNING. Access to the contents of this doctoral thesis and its use must respect the rights of the author. It can be used for reference or private study, as well as research and learning activities or materials in the terms established by the 32nd article of the Spanish Consolidated Copyright Act (RDL 1/1996). Express and previous authorization of the author is required for any other uses. In any case, when using its content, full name of the author and title of the thesis must be clearly indicated. Reproduction or other forms of for profit use or public communication from outside TDX service is not allowed. Presentation of its content in a window or frame external to TDX (framing) is not authorized either. These rights affect both the content of the thesis and its abstracts and indexes.

New Organic Electrochemical Sensing Platforms For The Point-Of-Need

DOCTORAL THESIS

ADIL AIT YAZZA

Tarragona, 2022

UNIVERSITAT
ROVIRA i VIRGILI

ADIL AIT YAZZA

New Organic Electrochemical Sensing Platforms For The Point-Of-Need

Doctoral Thesis

Supervised by

Dr. Francisco J. Andrade and Dr. Pascal Blondeau

Department of Analytical Chemistry and Organic Chemistry

UNIVERSITAT
ROVIRA i VIRGILI

Tarragona, 2022

ADIL AIT YAZZA

New Organic Electrochemical Sensing Platforms For The Point-Of-Need

Tribunal members:

Tarragona, 2022

UNIVERSITAT
ROVIRA i VIRGILI

UNIVERSITAT
ROVIRA i VIRGILI

I STATE that the present study, entitled “.New organic electrochemical sensing platforms for the point-of-need.”, presented by *Adil Ait Yazza* for the award of the degree of Doctor, has been carried out under my supervision at the Department of Analytical and Organic Chemistry of this university.

[Tarragona], [04/11/2022]

Doctoral Thesis Supervisor/s

[Francisco Javier Andrade]

[Pascal Blondeau]

Acknowledgements

This doctoral thesis would have not been accomplished without the support, guidance, and encouragement of a number of people for whom I hold a great deal of gratitude and respect.

First, I would like to express my sincere gratitude to my supervisor Dr. Francesco Javier Andrade, who embarked me in this endeavour. Dr. Andrade welcomed me to his lab since my master thesis, and provided the opportunity to discover the world of bio- and chemical sensors. Throughout my Ph.D. study, he offered an exciting, encouraging, and evolving environment, particularly, during our many discussions. Dr. Andrade cultivated in me the qualities of being a good scientist, and most importantly, a good critical thinker. It was a very enriching experience with abundant pleasure for me to be part of his group and conduct this dissertation under his supervision. I am grateful for his motivation, inspiration, guidance, and for keeping the door of his office always open for us despite his responsibilities.

I am also in great deal of debt to Dr. Pascal Blondeau for accepting to co-supervise this thesis. I am grateful for his support, patience, guidance, and optimism throughout these years, which have made a huge difference, especially, in difficult moments. I am also thankful to him for willing to share is knowledge in chemical sensors, and for our fruitful and insightful discussions throughout this Ph.D thesis, which have always been like food for my mind.

My very special gratitude goes to my parents Mbark and Aicha, and to my sisters Nadia and Sana, their children, and to all my family members, may Allah always protect them and bless them with health, happiness, prosperity and longevity. Their unconditional love and trust have always been for me a source of inspiration and motivation.

I must also address my appreciation and thanks to Dr. Santiago Macho with whom I shared office, for his much appreciated support and advices whenever I encountered technical problems.

I also express special thanks to all my lab colleagues, those who left, Marta, Anissa, and Mohammed for their collaboration and deer friendship. Also, those who still working on their Ph.D, especially, Andres, Ariadna, and Mark, for all the valuable moments we shared during my thesis. My appreciation also goes to Carlos and Adrian for their valuable advices. To all of them and others, I wish abundance of success and happiness in their personal lives and careers.

Special thanks is also in order, to the all SERVEI personnel at URV, particularly, Eric and Marianna for their support, patience, and valuable advices throughout this endeavour.

I will always remain grateful to my childhood friends Samir and Ibrahim for our valuable talks, and for always believing in my ability to overcome my challenges and reach my goals.

Table of Contents

Summary

In a nutshell, the objective of this doctoral thesis is to explore new thick film organic electrochemical devices on paper substrate, by means of conducting polymer inks and nanomaterials. The devices are based on two solid-state technologies: the organic electrochemical transistor (OECT) and the chemiresistor, and utilize facile fabrication and functionalization procedures, which enables the detection of relevant biomolecules.

To lay down the motivations behind this work, it is essential to take a close look at some key changes our society is undertaking. In the last few years, healthcare monitoring and diagnostic tools such as point-of-need (PON) and point-of-care (POC) witnessed a blooming demand from care providers as well as the general population. The widespread of wearable technology and the ongoing shift in healthcare paradigms made society very receptive to such tools. Furthermore, the increasing tendency of the world population's lifespan is expected to place healthcare systems under heavy strain in the long-term. For this reason, healthcare systems are growingly integrating best practices that promote awareness and prevention, in contrast to reaction and curation. Analytical chemistry contributes to this paradigm that is becoming more and more cross-disciplinary, by providing simple, reliable, and user-friendly analytical tools capable of transforming chemical signals to meaningful information.

On the other hand, solid-state devices featuring organic conducting polymers and nanomaterials are expected to offer an attractive alternative to conventional electrochemical methods such as potentiometry and amperometry. Among these devices, organic electrochemical transistors (OECTs) and chemiresistors, are two promising technologies due to their low power consumption, facile fabrication, and ion-to-electron transduction. These technologies rely heavily on sophisticated fabrication techniques that require controlled environments and expensive equipment, such as photolithography and inkjet printing to create functional thin films. However, less emphasis has been made on paper-based thick film devices. Therefore, the objective of this doctoral thesis is to develop versatile thick film OECTs and chemiresistors based on conducting polymer composites made of poly(3,4-ethylenedioxythiophene) doped with polystyrene sulfonate (PEDOT:PSS) and nanomaterials, toward the detection of different analytes. In this regard, this doctoral thesis is divided into nine chapters:

Chapter 1 sets up the global context for this Doctoral Thesis, and highlights also the general and specific objectives.

Chapter 2 lays out the foundations and the state-of-the-art of organic electrochemical transistors (OECTs) and their siblings' chemiresistors. It focuses on bio- and chemical sensing applications.

Chapter 3 deals with the experimental part, including the reagents, materials, methods, instruments and techniques employed through this work.

Chapter 4 demonstrates the construction and the optimization of thick-film PEDOT:PSS OECTs by drop casting technique.

Chapter 5 introduces a simple yet powerful approach for constructing a paper-based thick film organic electrochemical transistors for the detection of hydrogen peroxide and glucose.

Chapter 6, is dedicated to the development and characterization of OECTs with PEDOT:PSS/Nanomaterials composites for the detection of hydrogen peroxide.

Chapter 7 presents PEDOT:PSS/PtNPs composite chemiresistor, and demonstrates the detection of glucose and lactate in artificial sweat.

Chapter 8 presents a chemiresistive sensor for the detection of chloride.

Chapter 9 points out the final conclusions, and discusses future works and improvements.

1 Introduction

Summary

The objective of this chapter is to place the Ph.D thesis in the context of the current transformations that healthcare systems are undergoing. The continuous adoption of telehealth services, the widespread of wearable devices, and the rise of organic electronics has created a need for reliable, novel, and cost effective decentralized analytical tools such as point-of-need (PON) and point-of-care (POC) devices.

1.1 Motivations for decentralized point-of-need devices

1.1.1 Decentralized analytical tools

Traditionally, the approach of healthcare systems to the treatment of diseases has been based on the diagnosis of a set of common symptoms, and the prescription of a treatment accordingly[1]. Patients usually receive medication after they manifest recognizable symptoms. This reactive approach may render the treatment process long and costly. It may also make the patient go through unnecessary trauma, especially, when the disease is life-threatening such as cancer[2]. Indeed, it is now well accepted that this approach lacks a proactive aspect. Proactive integrated approaches (Figure 1.1) such as the one advocated by predictive, preventive and personalized medicines (3Ps), focus on promoting health and well-being by providing tailored healthcare services before the onset of diseases[3, 4].

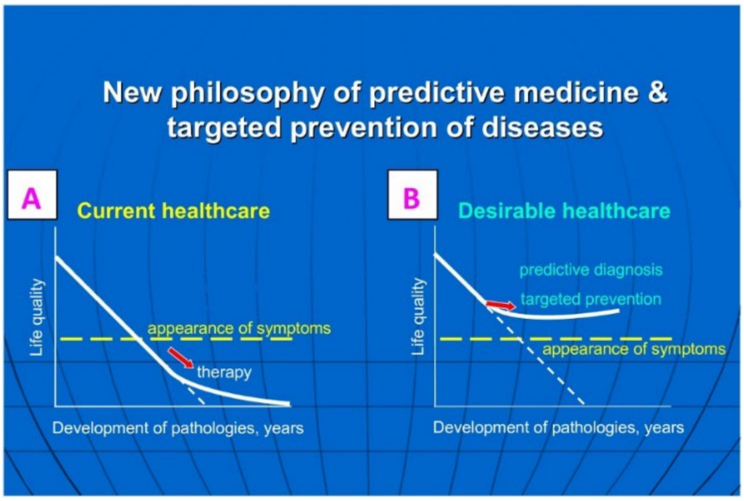

Figure 1.1. Models of traditional and preventive healthcare approaches. Image obtained from Golubnitschaja et al.[4]

The objective is to prevent common conditions or delay their appearance, and provide the necessary tools for the early diagnosis, treatment, and monitoring of diseases. With the advances achieved, among other fields, in analytical chemistry, immunology, proteomics[5], metabolomics[6], and organic electronics, the philosophy of healthcare systems is steadily evolving towards this ultimate goal. In order to support this evolution of healthcare systems, three fundamental challenges must be urgently addressed. First, the regulatory framework related to healthcare services need to be harmonized in a way that ensures the safety of patients and facilitates the use of novel technologies[7]. Second, the identification and validation of key metabolites and biomarkers that indicate reliably the onset of diseases[8]. To this end, research on relevant biomarkers in body fluids have shown a promising progress for the diagnosis of certain types of cancer[9], diabetes[10, 11], kidney diseases[12], etc. Finally, the development of simple analytical tools capable of detecting and quantifying these metabolites and biomarkers reliably, accurately, and easily[13]. Decentralized analytical tools, such as biosensor point-of-need technology, can fulfil this role and accelerate the transition of healthcare systems from treatment-centred approach to prevention-focused approach.

For this reason, there is an ever-increasing need for simple, rapid, accurate, and affordable analytical devices for healthcare monitoring and diagnosis of diseases. An example that is still in our short-term memory is the worldwide spread of Covid-19 pandemic, and the induced saturation of hospital services[14]. This unprecedented situation has accelerated the deployment of tele-diagnosis and tele-medicine solutions (i.e. healthcare services carried out via information and communication technologies) in many countries around the world[15]. Since the beginning of the pandemic, all the three major types of tele-medicine, namely, synchronous, asynchronous, and remote monitoring have seen a significant growth[16]. Synchronous refers to online healthcare services provided by a doctor over a distance, directly to a patient. In an asynchronous scenario, the patient sends to the doctor all relevant information pertaining to his health condition, and the doctor sends back his diagnosis and recommendations. Finally, remote monitoring stands for the continuous monitoring of the patient's health status by remotely collecting his health data. As an example, Figure 1.2 illustrates this new trend where in the USA alone, the number of telemedical consultations has surged by a factor of 38 from February 2020 to February 2021, compared to the pre-pandemic usage[17]. In Spain, for a major health services provider, teleconsultations increased from 3 % before the pandemic to 25 % a year later[18]. The same trend was observed in France, where the number of tele-consultations in 2019 represented 0.04 % of the total medical consultations recorded in the country. By June 2021, this number increased to 4.4 %[19]. Furthermore, the wide utilization of rapid disposable tests for the diagnosis of covid-19 has greatly reduced the time and cost of diagnosis, helped in breaking the contagion chain, and alleviated the overload of emergency services and testing facilities, particularly during peak periods[20]. Consequently, there is a growing believe that this transformation of the healthcare system will continue for the next coming years in favour of more decentralization, even after the end of the pandemic.

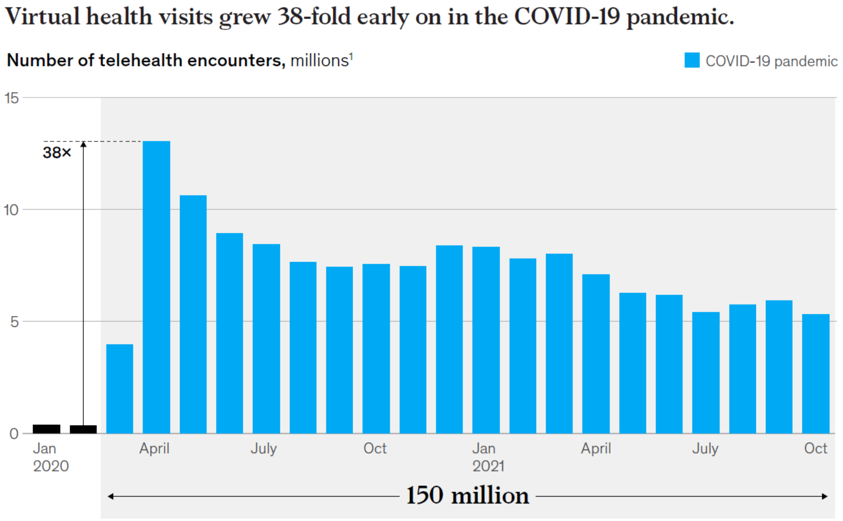
Virtual health visits grew 38-fold early on in the COVID-19 pandemic.

[1]Includes evaluation and management visits only; excludes emergency-department, hospital inpatient, and physiatry inpatient claims; excludes certain low-volume specialties; extrapolated to the commercial market.
Source: Compile Health database; McKinsey analysis

Figure 1.2. Telehealth usage in the USA before and after COVID-19 appearance. Image obtained from McKinzey & Company[17].

Decentralized analytical tools including point-of-care[21], disposable tests[22], and wearable sensors[23] can contribute efficiently to the improvement of health by collecting vital information about the patients, and making it available for healthcare specialists. The need for this kind of tools is becoming more obvious with the expected rise of the life span of the world population in the future, and the increasing demand for simple tools to monitor and manage chronic conditions. In the near future, decentralized analytical tools are expected to become a corner-stone of modern healthcare systems.

Additionally, decentralized healthcare tools can promote and democratize the access to healthcare services, especially in remote areas and countries where large populations have limited access to healthcare services[24]. Typical centralized medical laboratories, very often, require expensive equipment, which in turn necessitate highly qualified personal. In contrast, decentralized and disposable healthcare devices are easy to use, require a small amount of reagents, and can be integrated with portable and wearable devices such as smartphones.

Last, but not least, this shift of healthcare from treatment to prevention promotes the development of systems focused on enhancing the wellbeing of people. Therefore, the scope of monitoring systems is expected to extend beyond the “patients”, to include the general population that is increasingly willing to minimize health risks. Athletes (professional and amateurs) are a good example of the type of activities where monitoring parameters may help to reduce risk and enhance performance. Similarly, companies are offering today devices for continuous glucose monitoring to people willing to lose weight, as a way to improve the process while avoiding health issues.[25] Biosensors for the point of need will be a valuable tool, not only to control disease, but also to enhance the overall wellbeing of people.

1.1.2 Biosensors as analytical tools

In their seminal work covering pH and oxygen electrodes, in 1962, C. Clark and C. Lyons were the first to report the concept of a biosensor for the detection of glucose in blood[26]. In their work, they suggested the use of an enzyme entrapped in a dialysis membrane to convert glucose, and monitoring the change of pH or O_2 caused by the reaction. This major leap has paved the way for a new generation of (bio)analytical tools. It was not, however, until 1977 that K. Cammann introduced the term “biosensor” for the first time[27]. In 1992, The International Union of Pure and Applied Chemistry (IUPAC), has officially adopted the term biosensor, which defines as “a device that uses specific biochemical reactions mediated by isolated enzymes, immunosystems, tissues, organelles or whole cells to detect chemical compounds usually by electrical, thermal or optical signals”[28]. In an attempt to keep up with the rapid progress of biosensors research, the IUPAC published two technical reports in 2001 and 2010, providing additional definitions for electrochemical biosensors[29, 30]. Figure 1.3 describes the core elements of a typical biosensor. In addition to that, the term encompasses a set of characteristics that all analytical devices are expected to demonstrate, such as reproducibility, selectivity, sensitivity and ease of operation[31].

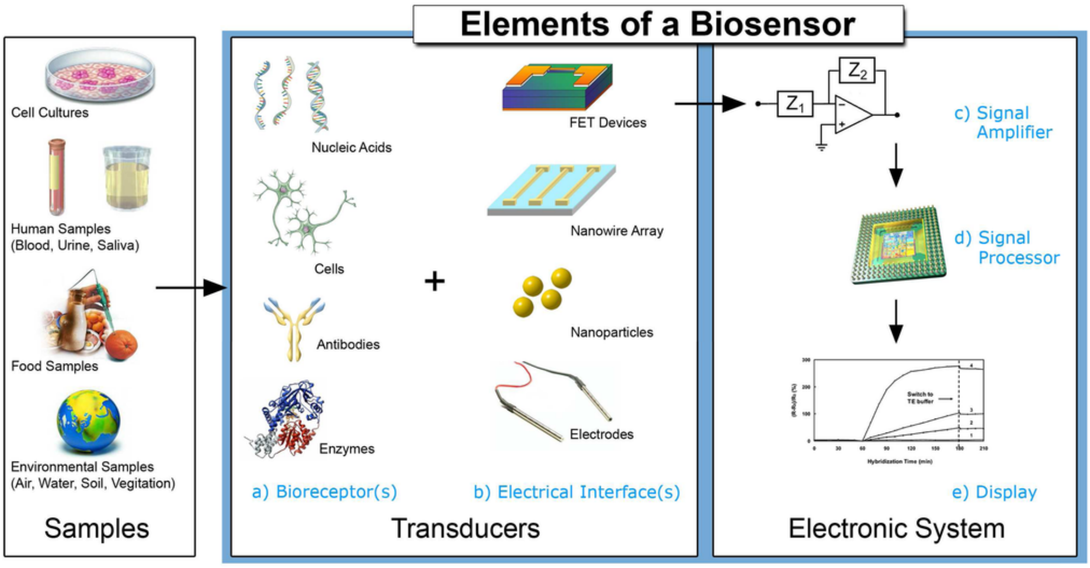

Figure 1.3. Basic elements of a biosensor. Image obtained from D. Grieshaber et al.[32]

Over the years, biosensor technology has evolved rapidly and become a multidisciplinary field at the interface of chemistry, medicine, and electronics. The technological advances and the challenges that society is facing, have provided a fertile soil for biosensors research to expand and cover a wide range of applications, including food quality[33], environment[34], homeland security[35], drugs screening[36], and healthcare[37]. Healthcare biosensors are of particular interest because they are intimately related to the wellbeing, health and safety of people. The last two decades have witnessed the development of a plethora of biosensors for the detection of relevant biomolecules and metabolites such as DNA[38], antibodies, amino acids[39], cholesterol[40], lactic acid[41], dopamine[42], and creatinine[43]. A part from biomolecules, biosensors are also designed to detect chemical species relevant for healthcare, such as potassium[44], calcium[45], ammonium[46], and chloride[47], among many others.

Furthermore, biosensors have benefited considerably from the progress achieved in materials science and nanotechnology. An important aspect of nanomaterials is that their properties can be tuned by controlling their size. For example, different biosensors were designed with novel catalytic[48], electrical, optical[49] and magnetic[50] properties by incorporating metallic and carbon nanomaterials such as gold nanoparticles (AuNPs)[51], platinum nanoparticles (PtNPs)[52], silver nanoparticles (AgNPs)[53], iron oxide[54], carbon nanotubes and graphene[55].

To construct biosensors, numerous transduction approaches have been developed, including electrochemical, optical, piezoelectric, quartz crystal microbalance, transistor-based sensors, and chemiresistive sensors. Based on these principles, multiple biosensors can be combined to build more complex systems, such as arrays[56], microfluidics[57], and lab-on-a-chip[58]. Another emerging platform, the organ-on-a-chip, which comprises biosensors along with living cells that emulate the functions of different human organs, all in one microfluidic device[59]. The organ-on-chips are designed for drugs screening, analysis, and modelling of the tissues response to new drugs via direct detection of biomolecules of interest released by the tissues[60].

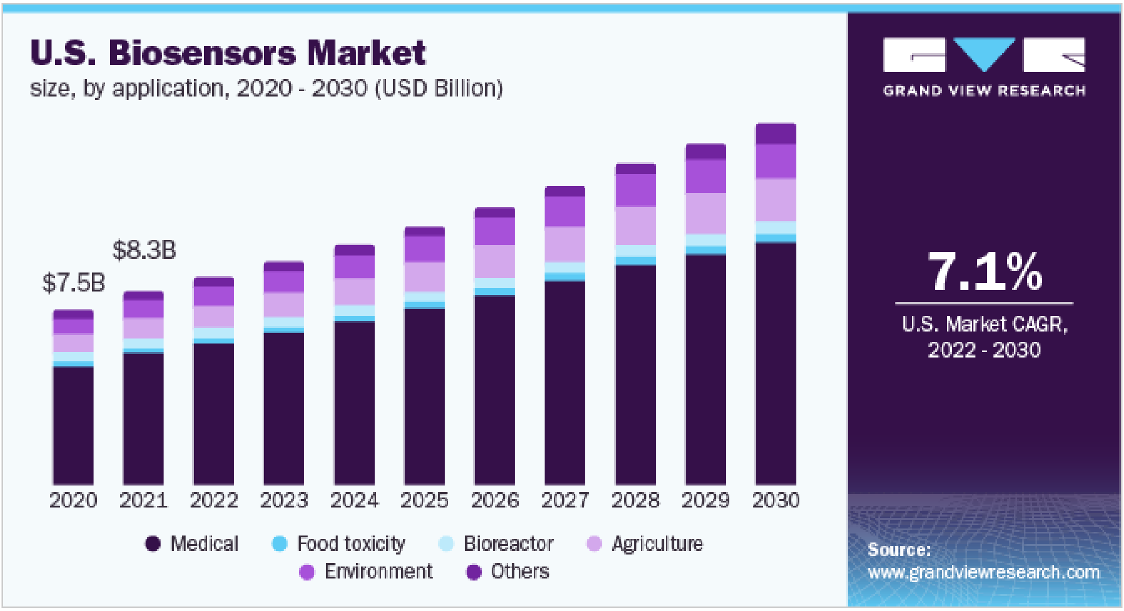

Figure 1.4. Evolution of USA biosensors market. Image obtained from ref.[61]

Despite the enormous potential of biosensors market (Figure 1.4) and the progress achieved in biosensors technologies in terms of performance, size, and fabrication, only a limited number of biosensors has left the laboratory bench and reached the market. This is usually attributed to a number of factors that range from the complexity of the detection mechanism, incompatibility with current mass production methods, to the failure to demonstrate reproducible performance in real-life settings[62].

1.1.3 Organic electronics: The technology of tomorrow

The high cost associated with the processing of metals and inorganic semiconductors has encouraged the scientific community to explore new alternative materials. Driven by the idea of low-cost, abundant, and synthetic conductive materials, these efforts have led H. Shirakawa, A. Heeger, and A. MacDiarmid in the late 70s to develop the first doped conductive polymer[63]. H. Shirakawa and his colleagues were able to increase the conductivity of polyacetylene from 10^{-5} $S.cm^{-1}$ to 100 $S.cm^{-1}$ by doping polyacetylene with halogens[64], an achievement that warrants Nobel Prize in 2000. It was rapidly realized that such novel materials would be an excellent alternative for inorganic semiconductors, core materials used to build electrical circuits and employed in a variety of applications. The integration of conductive polymers in electronic devices during the early 80s was the first seed that gave birth later to a new field called organic electronics[65].

In a broad sense, organic electronics is now well established field (with many new emerging areas) that aims at combining low-cost organic conductive materials, electronic devices, and large area production techniques for designing novel end user applications. The high impact of this emerging field has been the driving force for the growth of the entire chain value of organic electronics. A recent roadmap published by the Organic Electronic Association (OE-A), an internationally recognized body that counts more than 200 companies and research institutions, has identified six strategic industry sectors that drive research in organic electronics[66, 67]. As summarized in Figure 1.5, these sectors cover industries ranging from automotive to consumer electronics, via healthcare; from packaging, via smart buildings to Internet of Things (IoT)[66]. Within each sector, the roadmap has determined a number of emerging applications that are anticipated to evolve. In the near future, the key applications that are expected to lead the healthcare market include OLED (organic light-emitting diode) light therapy, smart patches and bandages for wound care and health monitoring, and wearable and off-body sensors for medical diagnosis.

OE-A Roadmap for Organic and Printed Electronics Applications 2020

	Existing 2020	Short Term 2021-2023	Medium Term 2024-2026	Long Term 2027+	
	Foldable displays for phones; Reflective EPD	large flexible OLED-Displays; rollable TV; curved display for automotive interior	In-mold electronic (IME) Displays;	Flexible QD-Displays; flexible µLED-Displays	**Flexible & OLED Displays**
OPV	OPV objects; portable chargers; OPV-R2R products	Opaque OPV for BIPV; Large area OPV foil; OPV power supply	Semitransparent OPV for BIPV; OPV for autonomous sensors	Color and shape on demand; OPV on “all” surfaces (e.g. wallpaper, mobile devices) combined with thin film battery	
	Printed devices: memory, RFID antenna, primary battery, active backplane, piezoelectric elements; Sensors: glucose, pressure, temperature, humidity; printed phone case integrated antenna; thin flexible Si-chips	light sensor; stretchable conductors / resistors; 3D touch sensors; OTFT backplanes for low energy displays and OPD; 3D & large area flexible electronics; active touch sensors	Printed secondary ion battery; printed super caps; gesture sensors	Complex stretchable electronics; Printed complex logic;	**Electronics & Components**
Integrated Smart Systems	Smart label sensors (humidity, temperature); Sensors for blood analysis; NFC labels; Hybrid systems (printed components + flexible ICs); HMIs (sensors)	Ambient monitoring (e.g. humidity); sensors embedded in molded parts (automotive); on-skin human monitoring patches for sports; ambient intelligence (connected); Sleep disturbance monitoring;	On-skin human monitoring patches in clinical environment; Single article tagging (food)	Smart labels with geo localization; Breath analyzer for medical prevention	
	Flexible white OLED modules; rigid red OLEDs for automotive applications	Flexible red OLEDs (segmented) for automotive applications; transparent OLEDs; OLEDs for interior lighting of automotive	3D OLEDs; OLED signage; OLED for medical applications	OLED for aircraft and railway interior application	**OLED Lighting**

Figure 1.5. OE-A roadmap summarizing the key organic and printed electronics applications and their forecasts. Image obtained from OE-A Roadmap[67].

OLEDs for light therapy

The study of the effects of light on different biological tissues is an active area of research. One of the earliest experiments can be traced to E. Mester in 1967, when he reported the beneficial effect of low-power laser on hair growing and wound healing in rats[68]. In the last decade, OLEDs have attracted significant interest as light sources because of their high efficiency, low-cost, low power consumption, flexibility, and robustness. The simplest architecture of an OLED, as illustrated in Figure 1.6A, comprises at least, an organic conductive material sandwiched between two electrodes, namely, the cathode and the anode. One of the electrodes is made transparent to collect the light generated. When a voltage is applied between the two electrodes, opposite charge carriers (a hole and an electron) diffuse through the electrodes and recombine in the conductive polymer, generating visible/infrared light in the process[69, 70]. Recent works have demonstrated the potential of utilising OLEDs in various photobiomodulation applications (Figure 1.6B), such as wound healing[71], antimicrobial[72], immunomodulation and optogenetics[73]. However, the lack of long-term cytotoxicity studies and clinical trials represent the major challenge that hinders the progress of OLED therapeutic applications.

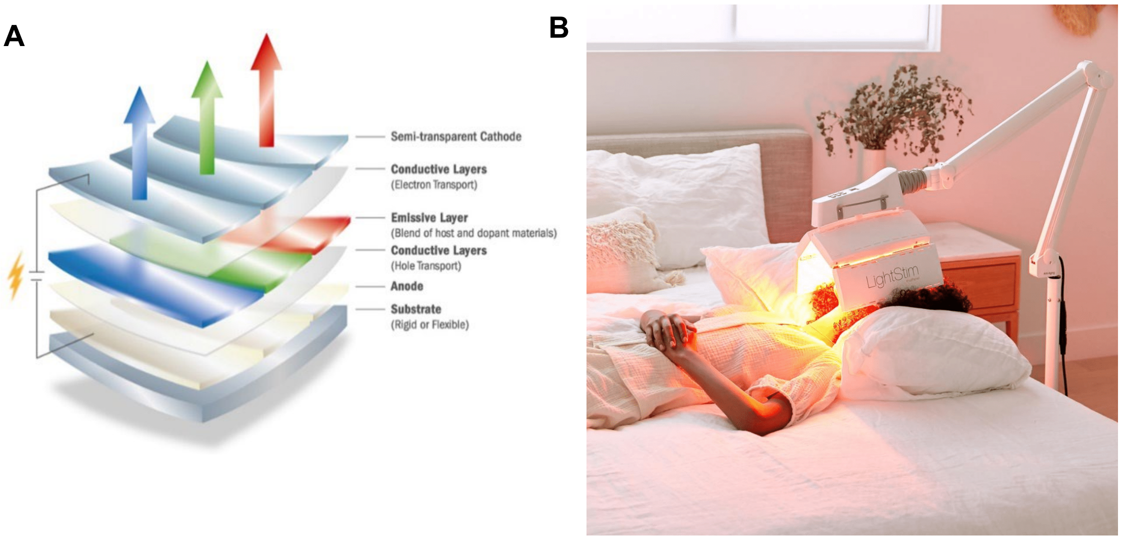

Figure 1.6. A) Scheme of an OLED. Image from B) LED device for anti-aging, acne or pain, approved by the Food and Drug Administration (FDA)[74].

Smart bandages and patches

Bandages and patches are among the promising healthcare applications that combine organic electronics and biosensors. The ability to process flexible and biocompatible materials capable of coupling the shape of the body while maintaining functionality, makes organic electronics an attractive technology for building smart bandages. The main role of a typical bandage is to prevent the infection and promote the healing of wounds. With the help of conductive polymers, smart bandages take this role steps further by tracking the healing process via local monitoring of various wound-health indicators, such as temperature, pH, humidity, and oxygen[75]. For instance, F. Mariani *et al.* demonstrated a smart dressing for real-time monitoring of pH by incorporating iridium oxide particles in conducting polymer[76]. Furthermore, A. Khademhosseini *et al.* successfully fabricated an advanced electrochemical-based bandage that takes an active role in the treatment of chronic non-healing wounds, a condition that is usually associated with diabetic patients[77]. The designed bandage was able to locally release antibiotic drugs when pH and temperature reach specific limits.

Wearable and off-body biosensors

Wearable biosensors are another major area where organic electronics is expected to push the limits towards high scalability, low-cost, and ease of integration. Conducting polymers are increasingly utilized in the fabrication of wearable devices because they impart sensors with the flexibility needed to withstand motion-related deformations[78]. Wearable biosensors enable the real-time detection of a wide range of biomarkers in biological fluids such as blood, saliva, sweat, and urine[37, 79]. For instance, sweat is an ideal candidate for non-invasive wearable sensors because it contains a variety of biomarkers that can be correlated to health conditions and diseases[80]. Apart from regulating the temperature of the body, sweat contains among others, glucose, lactate, uric acid, sodium, and potassium. As an example, P. Pirovano et al. has developed an electrochemical wearable sensor based on poly(3,4-ethylenedioxythiophene) (PEDOT) that could specifically detect sodium and potassium in sweat[81]. In addition to electrolytes, sweat alone contains a large pool of biomolecules, comprising more than 860 unique proteins, which makes a very attractive non-invasive source of potential biomarkers[82].

1.1.4 Organic Thin-Film Transistors

Organic Thin-Film Transistors (OTFT) are a subgroup of organic electronic devices, which originate from the Field Effect Transistor (FET). The FET is a solid-state device that modulates an electrical current flowing through an inorganic semiconductive film, via an induced capacitive effect[83]. Since it was invented by Bell Laboratories in 1948, the transistor has become the focus of a tremendous amount of research in both academia and industry. As a result, the FET underwent a continuous development in every aspect of its manufacturing, including its fabrication process, materials, size, performance, and design. Consequently, transistors became smaller, faster, and less expensive, as the number of transistors per unit area increased exponentially.

In 1984, White et al. pioneered the first Organic Electrochemical Transistor (OECT)[84]. Instead of an inorganic film, the first OECT was comprised of a conductive polymer film made of polypyrrole, whose conductivity was controlled by applying a gate voltage through an electrolyte. Over the years, the family of organic transistors has expanded to include the Organic Field Effect Transistors (OFETs), and the Electrolyte-Gated Organic Field Effect Transistors (EGOFETs)[85]. Organic electrochemical transistors (OECTs) are notorious for having low operating voltages, high amplification, and high switching speeds. The key feature that endows OECTs with such properties is the high volumetric capacitance demonstrated by the conductive polymers typically used to build OECTs[86]. Figure 1.7 illustrates the major differences between OECTs, OFETs, and EGOFETs. The OECTs involve the injection of ions inside the channel, whereas EGOFET and OFET involve the accumulation of ions on the surface of the channel.

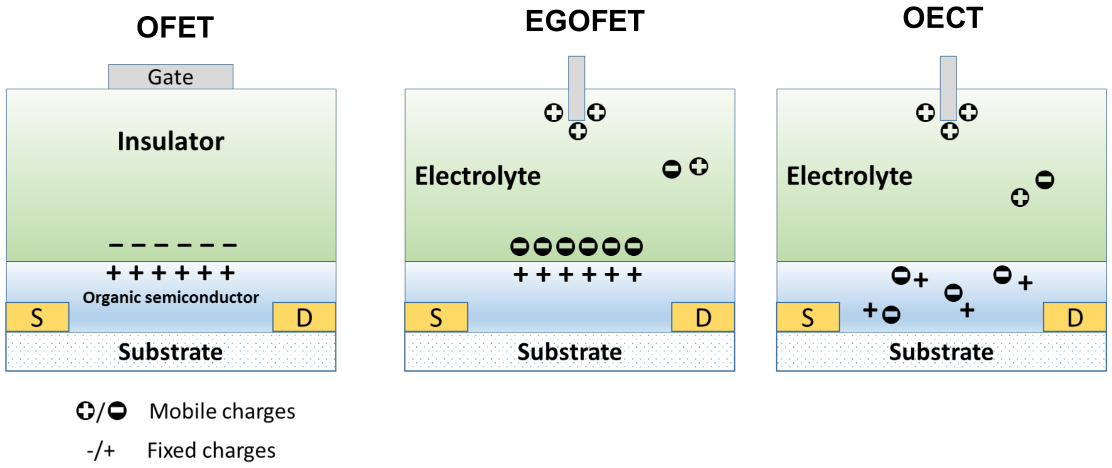

Figure 1.7. Description of three organic transistors: OFET, EGOFET, and OECT. Image adapted from Sun et al.[87]

In the last decade, organic electrochemical transistors have been the focus of an extensive research for biosensing applications[85, 88]. The most attractive feature of these devices is that they provide an alternative path for signal transduction in electrochemical sensing, with high amplification of the signal but avoiding the charge-transfer related problems. Further details about the working principle and the sensing mechanism of OECTs is included in Chapter 2.

Interestingly, the published research shows that -unlike other electrochemical tools- a good part of the research in organic transistors stems from electronic engineering and materials science. Analytical journals have published considerably less works on these tools. Thus, there is still significant room to explore strategies for optimization and analytical applications of these devices.

1.2 Objectives & Outline of the thesis

So far, thin-film technology is the standard for building solid-state biosensors such as organic electrochemical transistors (OECTs) and chemiresistors.[89-91] This technology, in principle, utilizes complex protocols and requires expensive facilities and equipment (e.g. cleanroom, inkjet printer, etc.) to achieve conducting polymers films with a thickness in the nanoscale range. However, less emphasis has been made on the analytical performance of thick-film OECTs and chemiresistors constructed via facile methods. The ultimate goal of this thesis was to develop new thick-film organic electrochemical devices, based on PEDOT:PSS and its composites, via simplified and efficient protocols of construction. In a nutshell, this work has been focused on exploring the use of poly(3,4-ethylenedioxythiophene) polystyrene sulfonate (PEDOT:PSS) ink to build organic electrochemical transistors (OECTs) and chemiresistors as solid-state platforms for (bio)chemical sensing in the point-of-need. Therefore, the objectives of this thesis are:

- To investigate the effect of geometry, partcularly width-to-length variation, on the key properties of thick-film OECTs that have high relevance to bio- and chemical sensing.
- To construct paper-based thick film OECTs for the detection of H_2O_2 and evaluate their electrical and analytical performance.
- To build and characterize thick-film OECTs with sensitized channels utilizing different PEDOT:PSS/nanomaterials composites, and evaluate their performance for the detection of H_2O_2.
- To explore the possibility to construct biochemical chemiresistors based on PEDOT:PSS/nanoparticles composites.
- To extend the channel sensitization to construct cheniresistors for the detection chloride ions.

1.3 References

[1] Nardini, C.; Osmani, V.; Cormio, P. G.; et al., *Per Med*, **2021**, 18, 283-294.

[2] Leano, A.; Korman, M. B.; Goldberg, L.; et al., *Can Oncol Nurs J*, **2019**, 29, 141-146.

[3] Flores, M.; Glusman, G.; Brogaard, K.; et al., *Per Med*, **2013**, 10, 565-576.

[4] Golubnitschaja, O.; Kinkorova, J.; Costigliola, V., *EPMA J*, **2014**, 5, 6.

[5] Jain, K. K. Role of Proteomics in the Development of Personalized Medicine. Elsevier, 2016; 41-52.

[6] Buergel, T.; Steinfeldt, J.; Ruyoga, G.; et al., *Nat Med*, **2022**, 1-32.

[7] Goetz, L. H.; Schork, N. J., *Fertil Steril*, **2018**, 109, 952-963.

[8] Mandrekar, S. J.; Sargent, D. J., *J Biopharm Stat*, **2009**, 19, 530-542.

[9] Masucci, G. V.; Cesano, A.; Hawtin, R.; et al., *J Immunother Cancer*, **2016**, 4, 2-17.

[10] Dorcely, B.; Katz, K.; Jagannathan, R.; et al., *Diabetes Metab Syndr Obes*, **2017**, 10, 345-361.

[11] Long, J.; Yang, Z.; Wang, L.; et al., *BMC Endocr Disord*, **2020**, 20, 174.

[12] Rysz, J.; Gluba-Brzozka, A.; Franczyk, B.; et al., *Int J Mol Sci*, **2017**, 18, 1702.

[13] Castelli, F. A.; Rosati, G.; Moguet, C.; et al., *Anal Bioanal Chem*, **2022**, 414, 759-789.

[14] *Creating surge capacity for acute and intensive care*; WHO/EURO:2020-670-40405-54163; https://apps.who.int/iris/bitstream/handle/10665/332562/WHO-EURO-2020-670-40405-54163-eng.pdf?sequence=1&isAllowed=y.

[15] Mann, D. M.; Chen, J.; Chunara, R.; et al., *J Am Med Inform Assoc*, **2020**, 27, 1132-1135.

[16] Wosik, J.; Fudim, M.; Cameron, B.; et al., *J Am Med Inform Assoc*, **2020**, 27, 957-962.

[17] Singhal, S.; Vinjamoori, N.; Radha, M. *The next frontier of healthcare delivery*. 2022. https://www.mckinsey.com/industries/healthcare-systems-and-services/our-insights/the-next-frontier-of-care-delivery-in-healthcare (accessed July 5, 2022).

[18] Morcillo Serra, C.; Aroca Tanarro, A., *Med Clin (Barc)*, **2022**, 158, 122-124.

[19] *La téléconsultation séduit un nombre toujours plus important de Français [Teleconsultation is attracting an ever-increasing number of French people]*. Le Figaro, 2021. https://sante.lefigaro.fr/article/la-teleconsultation-seduit-un-nombre-toujours-plus-important-de-francais/ (accessed July 5, 2022).

[20] Vandenberg, O.; Martiny, D.; Rochas, O.; et al., *Nat Rev Microbiol*, **2021**, 19, 171-183.

[21] Vashist, S. K., *Biosensors (Basel)*, **2017**, 7, 10-13.

[22] Dincer, C.; Bruch, R.; Costa-Rama, E.; et al., *Adv Mater*, **2019**, 31, e1806739.

[23] Sempionatto, J. R.; Jeerapan, I.; Krishnan, S.; et al., *Anal Chem*, **2020**, 92, 378-396.

[24] *Enhancing access to healthcare with point-of-care diagnostics technology*. 2022. https://www.healtheuropa.com/enhancing-access-to-healthcare-with-point-of-care-diagnostics-technology/113501/ (accessed January 5, 2022).

[25] Vidmar, A. P.; Naguib, M.; Raymond, J. K.; et al., *Nutrients*, **2021**, 13, 3697.

[26] Clark, L. C., Jr.; Lyons, C., *Ann N Y Acad Sci*, **1962**, 102, 29-45.

[27] Cammann, K., *Fresenius' Zeitschrift für analytische Chemie*, **1977**, 1-9.

[28] Gold, V. The IUPAC Compendium of Chemical Terminology. International Union of Pure and Applied Chemistry, 2019.

[29] Thévenot, D. R.; Toth, K.; Durst, R. A.; et al., *Biosens Bioelectron*, **2001**, 16, 121-131.

[30] Labuda, J.; Brett, A. M. O.; Evtugyn, G.; et al., *Pure Appl Chem*, **2010**, 82, 1161-1187.

[31] Bhalla, N.; Jolly, P.; Formisano, N.; et al., *Essays Biochem*, **2016**, 60, 1-8.

[32] Grieshaber, D.; MacKenzie, R.; Voros, J.; et al., *Sensors (Basel)*, **2008**, 8, 1400-1458.

[33] Dwidar, M.; Yokobayashi, Y., *Sci Rep*, **2019**, 9, 16659.

[34] Perez-Fernandez, B.; Costa-Garcia, A.; Muniz, A. E., *Biosensors (Basel)*, **2020**, 10, 32.

[35] Liu, R.; Li, Z.; Huang, Z.; et al., *TrAC, Trends Anal Chem*, **2019**, 118, 123-137.

[36] Tao, Y.; Chen, L.; Pan, M.; et al., *ACS Sens*, **2021**, 6, 3146-3162.

[37] Kim, J.; Campbell, A. S.; de Avila, B. E.; et al., *Nat Biotechnol*, **2019**, 37, 389-406.

[38] Dong, S.; Zhao, R.; Zhu, J.; et al., *ACS Appl Mater Interfaces*, **2015**, 7, 8834-8842.

[39] Moulaee, K.; Neri, G., *Biosensors (Basel)*, **2021**, 11, 502.

[40] Sekretaryova, A. N.; Beni, V.; Eriksson, M.; et al., *Anal Chem*, **2014**, 86, 9540-9547.

[41] Xuan, X.; Perez-Rafols, C.; Chen, C.; et al., *ACS Sens*, **2021**, 6, 2763-2771.

[42] Gualandi, I.; Tonelli, D.; Mariani, F.; et al., *Sci Rep*, **2016**, 6, 35419.

[43] Karakuzu, B.; Tarim, E. A.; Oksuz, C.; et al., *ACS Omega*, **2022**, 7, 25837-25843.

[44] Liu, X.; Ye, C.; Li, X.; et al., *Materials (Basel)*, **2018**, 11, 399.

[45] van der Linden, F. H.; Mahlandt, E. K.; Arts, J. J. G.; et al., *Nat Commun*, **2021**, 12, 7159.

[46] Bollmann, A.; Revsbech, N. P., *Sens Actuators B: Chem*, **2005**, 105, 412-418.

[47] Dong, H.; Zhang, L.; Liu, W.; et al., *ACS Chem Neurosci*, **2017**, 8, 339-346.

[48] Brondani, D.; Scheeren, C. W.; Dupont, J.; et al., *Sens Actuators B: Chem*, **2009**, 140, 252-259.

[49] Fothergill, S. M.; Joyce, C.; Xie, F., *Nanoscale*, **2018**, 10, 20914-20929.

[50] Haun, J. B.; Yoon, T. J.; Lee, H.; et al., *Wiley Interdiscip Rev Nanomed Nanobiotechnol*, **2010**, 2, 291-304.

[51] Shen, Y.; Shen, G., *ACS Omega*, **2019**, 4, 5083-5087.

[52] Zhai, D.; Liu, B.; Shi, Y.; et al., *ACS Nano*, **2013**, 7, 3540-3546.

[53] Nantaphol, S.; Chailapakul, O.; Siangproh, W., *Sens Actuators B: Chem*, **2015**, 207, 193-198.

[54] Patel, S. K. S.; Anwar, M. Z.; Kumar, A.; et al., *Biochem Eng J*, **2018**, 132, 1-8.

[55] Zhu, Z., *Nanomicro Lett*, **2017**, 9, 25.

[56] Park, J.; Sempionatto, J. R.; Kim, J.; et al., *ACS Sens*, **2020**, 5, 1363-1373.

[57] Xiao, J.; Liu, Y.; Su, L.; et al., *Anal Chem*, **2019**, 91, 14803-14807.

[58] Luka, G.; Ahmadi, A.; Najjaran, H.; et al., *Sensors (Basel)*, **2015**, 15, 30011-30031.

[59] Ferrari, E.; Palma, C.; Vesentini, S.; et al., *Biosensors (Basel)*, **2020**, 10, 110.

[60] Jodat, Y. A.; Kang, M. G.; Kiaee, K.; et al., *Curr Pharm Des*, **2018**, 24, 5471-5486.

[61] *Biosensors Market Size, Share & Trends Analysis Report*. https://www.grandviewresearch.com/industry-analysis/biosensors-market (accessed August 13, 2022).

[62] Liu, G., *Front Bioeng Biotechnol*, **2021**, 9, 707615.

[63] Shirakawa, H., *Angew Chem Int Ed*, **2001**, 40, 2574-2580.

[64] Chiang, C. K.; Park, Y. W.; Heeger, A. J.; et al., *J Chem Phys*, **1978**, 69, 5098-5104.

[65] Potember, R. S.; Hoffman, R. C.; Hu, H. S.; et al., *Polym J*, **1987**, 19, 147-156.

[66] Bonnassieux, Y.; Brabec, C. J.; Cao, Y.; et al., *Flex Print Electron*, **2021**, 6, 023001.

[67] OE-A. *Executive Summary - OE-A Roadmap for Organic and Printed Electronics*; 2020.

[68] Mester, E.; Szende, B.; Gartner, P., *Radiobiol Radiother (Berl)*, **1968**, 9, 621-626.

[69] Murawski, C.; Gather, M. C., *Adv Opt Mater*, **2021**, 9, 2100269.

[70] Hong, G.; Gan, X.; Leonhardt, C.; et al., *Adv Mater*, **2021**, 33, e2005630.

[71] Wu, X.; Alberico, S.; Saidu, E.; et al., *Wound Repair Regen*, **2015**, 23, 104-114.

[72] Lian, C.; Piksa, M.; Yoshida, K.; et al., *npj Flex Electron*, **2019**, 3, 1-6.

[73] Jeon, Y.; Choi, H.-R.; Lim, M.; et al., *Adv Mater Technol*, **2018**, 3, 1700391.

[74] *Lightsim*. https://lightstim.com/products/lightstim-propanel (accessed March 25, 2022).

[75] Derakhshandeh, H.; Kashaf, S. S.; Aghabaglou, F.; et al., *Trends Biotechnol*, **2018**, 36, 1259-1274.

[76] Mariani, F.; Serafini, M.; Gualandi, I.; et al., *ACS Sens*, **2021**, 6, 2366-2377.

[77] Mostafalu, P.; Tamayol, A.; Rahimi, R.; et al., *Small*, **2018**, 14, e1703509.

[78] Tran, V. V.; Lee, S.; Lee, D.; et al., *Polymers (Basel)*, **2022**, 14, 3730.

[79] Windmiller, J. R.; Wang, J., *Electroanalysis*, **2013**, 25, 29-46.

[80] Brunmair, J.; Gotsmy, M.; Niederstaetter, L.; et al., *Nat Commun*, **2021**, 12, 5993.

[81] Pirovano, P.; Dorrian, M.; Shinde, A.; et al., *Talanta*, **2020**, 219, 121145.

[82] Yu, Y.; Prassas, I.; Muytjens, C. M.; et al., *J Proteom*, **2017**, 155, 40-48.

[83] Klauk, H., *Chem Soc Rev*, **2010**, 39, 2643-2666.

[84] White, H. S.; Kittlesen, G. P.; Wrighton, M. S., *Journal of the American Chemical Society*, **2002**, 106, 5375-5377.

[85] Lin, P.; Yan, F., *Adv Mater*, **2012**, 24, 34-51.

[86] Proctor, C. M.; Rivnay, J.; Malliaras, G. G., *J Polym Sci, Part B: Polym Phys*, **2016**, 54, 1433-1436.

[87] Sun, H.; Gerasimov, J.; Berggren, M.; et al., *J Mater Chem C*, **2018**, 6, 11778-11784.

[88] Strakosas, X.; Bongo, M.; Owens, R. M., *J Appl Polym Sci*, **2015**, 132, 41735.

[89] Wang, N.; Yang, A.; Fu, Y.; et al., *Acc Chem Res*, **2019**, 52, 277-287.

[90] Patel, V.; Kruse, P.; Selvaganapathy, P. R., *Biosensors (Basel)*, **2020**, 11, 1-33.

[91] Kumar, A.; Goyal, A. K.; Gupta, N., *ECS J Solid State Sci Technol*, **2020**, 9, 115022.

2 Foundations of OECTs and Chemiresistors

Summary

This chapter provides a description of the working principle of OECTs, as well as a brief presentation of chemiresistors. The objective is to present and describe the main elements and figure of merit of OECTs that are relevant to bio- and chemical sensors. Common fabrication methods and models usually used to predict the response of OECTs are also discussed.

2.1 Organic Electrochemical Transistors (OECTs)

2.1.1 Working principle of OECTs

An organic electrochemical transistor (OECT) is a device made of three electrodes and a conducting polymer channel[1]. As illustrated in Figure 2.1, two of the electrodes, the source (S) and the drain (D), are separated by a gap L, and connected by an organic conducting polymer film (referred to as the channel) with a given thickness (t), and width (W). The conducting polymer is also in contact with an electrolyte solution in which the third electrode, the gate, is immersed.

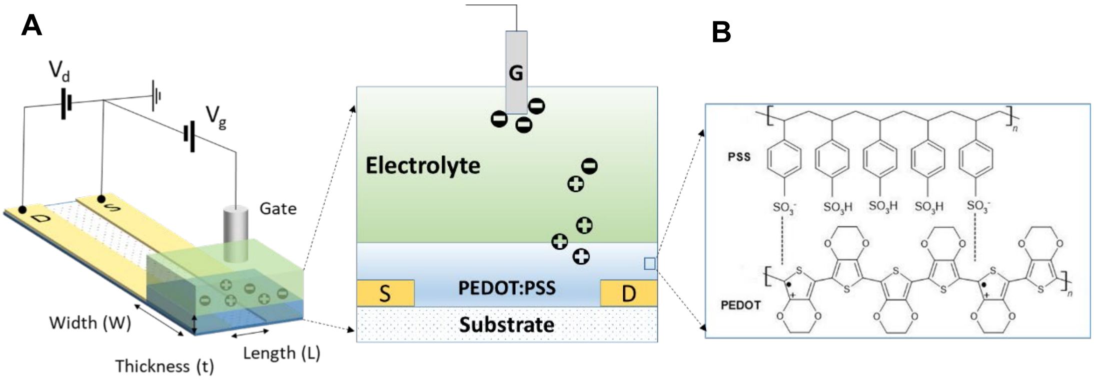

Figure 2.1. A) Description of an OECT and B) the structure of PEDOT:PSS.

A voltage V_d applied between the source and the drain, creates an electrical current, the drain current (I_d) that flows through the channel. The value of I_d depends mainly on the conductivity of the channel, which is the result of the degree of oxidation of the conducting polymer. This can be modulated by applying a voltage (V_g) at the gate electrode. The change in I_d depends, among other factors, on the sign and magnitude of V_g, geometry of the device, and the properties of the conducting polymer[2]. Details of the mechanism are well described in the literature[3]. Equation 2.1 captures the working mechanism of the most common positive type OECT. In essence, when a conducting polymer such as PEDOT:PSS is used (Figure 2.1B), a positive gate voltage causes cations to be injected from the electrolyte into the channel (de-doping)[4]. These cations shield the stabilizing effect that the sulfonate anions have on the oxidized form (PEDOT$^+$), shifting the state of the polymer to its reduced state (less conductive), as represented by Equation 2.1. This decreasing on the bulk conductivity of PEDOT:PSS is measured as a decrease in I_d [5]. In contrast, a negative gate voltage results in the extraction of cations, which leads to an increase in the oxidation (and therefore conductivity) of PEDOT:PSS (doping), and eventually an increase in I_d.

$$\mathrm{PEDOT^+:PSS^-} + \mathrm{A^+} + \mathrm{e^-} \Leftrightarrow \mathrm{PEDOT^0} + \mathrm{PSS^-:A^+} \qquad \text{Equation 2.1}$$

Where PEDOT$^+$ and PEDOT^0 are the oxidised and the reduced form of the conducting polymer, respectively, and A$^+$ is a cation.

2.2 Components of OECTs

2.2.1 Conductive polymer channel

Conductive polymers (CPs) are carbon-based π-conjugated materials with an intrinsic conductivity comparable to that of metals due to the presence of alternating single/double bonds[6]. An important characteristic of conducting polymers is that the reversal of their single/double bonds results in two structures that have different energies. Being loosely attached to atoms, π electrons can be delocalized along the backbone of the polymer, giving rise to electrical conductivity. The molecular orbital theory, traditionally used to describe energy levels in molecules, can be equally applied to conductive polymers. In these polymers, the allowed energy levels form two distinct bands: the lowest unoccupied molecular orbital (LUMO), and the highest occupied molecular orbital (HOMO), separated by a small energy gap[7] (Figure 2.2A). The charge transport in conductive polymers is largely affected by the synthesis method, crystallinity, and chemical doping, which makes the study of charge transport challenging[8-10]. However, hopping is widely accepted as the main mode of charge transport, where charge hop from one chain to another[8]. The concept of polaron/ bipolaron is also widely used to describe charge carriers in conductive polymers[11]. When the main chain of the conjugated polymer is oxidized, an electron is removed from the HOMO, leaving a hole in its place. As a result, a quasi-particle referred to as polaron is formed. The removal of an additional electron in a polymer chain, already containing a polaron, results in the formation of a bipolaron[11, 12].

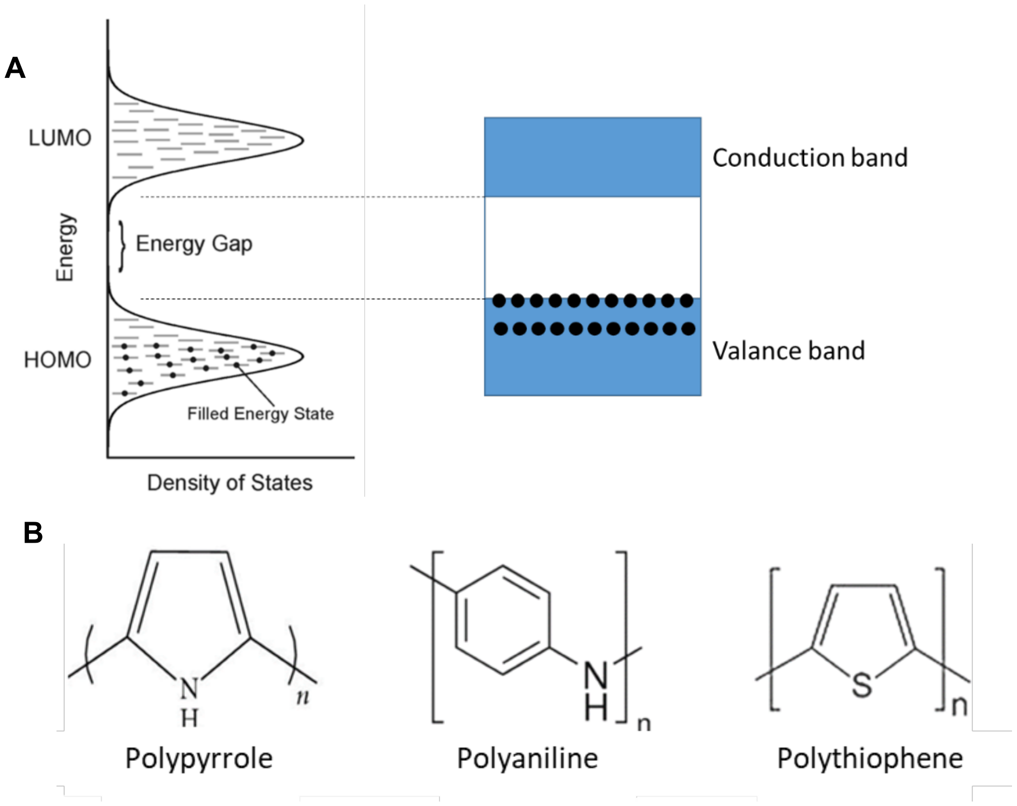

Figure 2.2. A) Energy levels of a conductive polymer, and B) three of the most common conductive polymers. Images adapted from

Figure 2.2B shows the most important families of CPs which include polypyrrole, polyaniline, and poly(3,4-ethylenedioxythiophene) PEDOT. Their conductivity can be further increased via positive or negative doping process, that is, the oxidation (p-doping) or reduction (n-doping) of the conjugated polymer[13]. For instance, the neutral PEDOT is less conductive and insoluble in aqueous solutions. For this reason, PEDOT is oxidised to $PEDOT^+$ and stabilised with a polyanion such as polystyrene sulfonate (PSS^-)[14]. The negatively charged sulfonate groups compensate the positively charged PEDOT, improving its conductivity, stability, and solubility in water (Figure 2.1B). Within the framework of solid-state physics, PEDOT:PSS is commonly referred to as a p-type organic semiconductive polymer. That is to say, the charge carriers responsible for its conductivity are positively charged holes (h^+), in contrast to n-type semiconductors where the charge carriers are electrons (e^-).

Different methods have been suggested to improve the conductivity of thin film PEDOT:PSS, including treatment with ethanol[15], phosphoric acid[16], DMSO[17], ethylene glycol[18], sorbitol[19], and ionic liquids[20]. As a result, PEDOT:PSS with conductivities over 2600 $S.cm^{-1}$ have been reported[21]. For this reason, PEDOT:PSS become the conductive polymer of choice for building the channel due to its low-cost, high conductivity, stability, and solution processability[22].

2.2.2 Source/Drain electrodes

The role of the source (S) and drain (D) electrodes is to provide a biased voltage through the channel, allowing an efficient injection and extraction of charge carriers[23]. In general, the source corresponds to the electrode from which the charge carrier is injected into the channel, whereas the drain corresponds to the electrode that extracts the charge carrier[24]. Hence, the material used to make the two electrodes affects the overall performance of the OECT. For this reason, the ideal material should demonstrate a number of characteristics: (i) have an excellent conductivity (ii) ensure a negligible contact resistance with the channel (iii) be chemically stable in aqueous environments[25]. Different materials have been used to build the source and the drain including gold, PEDOT:PSS, and carbon inks. Despite being a noble metal, gold remains the most common material used to build the source and the drain electrodes.

2.2.3 Gate electrode

The nature and the size of the gate electrode have a significant impact on the response of OECTs[26]. Two types of electrodes are typically used to construct the gate, depending on the nature of the interface they produce when immersed in an electrolyte, polarizable and non-polarizable electrodes[27]. When an ideal polarizable electrode, such a platinum or gold, is subjected to a varying potential, no current flows at the interface electrode/electrolyte, and its behaviour is usually approximated by a simple capacitor. In contrast, a non-polarizable electrode such as Ag/AgCl, frequently used for electrochemical tests, shows very low capacitance, and exhibits a behaviour similar to a resistor[5, 27, 28]. Ag/AgCl is typically used for the electrical characterization of OECTs.

2.2.4 Substrate

To construct OECTs, various materials have been used as a substrate, including glass[29], plastic[30], elastomer[31], textile[32], and paper[33]. The choice of the substrate is usually dictated by the fabrication method and the application intended of the device. Paper has a particular interest as a substrate, since it is abundant, affordable, flexible, and customizable. In addition, its 3D cellulose structure gives it excellent mechanical properties, lightweight, and biocompatibility. This allows not only OECTs to be built from paper substrate, but also complex microfluidic systems can be designed and patterned on paper using modern technologies such as inkjet printing and laser cutting[34, 35]. For example, an inkjet printed disposable breathalyser based on paper OECT has been reported for the qualitative detection of alcohol in breath[36]. Field-effect transistors logic circuits and biosensors with competitive performance have also been patterned on paper[37]. Therefore, paper is a promising material that can promote the widespread of biosensors and point-of-need devices.

2.3 Characteristics of OECTs

2.3.1 Transfer and output characteristics

The response of OECTs is commonly characterized by constructing two plots, the transfer curve and the output response[3]. Figure 2.3A represents a typical transfer curve (I_d vs V_d) which displays I_d as a function of V_g, and is measured by sweeping V_g at constant V_d. On the other hand, Figure 2.3B shows an example of the output curve (I_d vs V_d), which demonstrates the relationship between I_d and V_d, and is obtained by sweeping V_d while maintaining V_g at a constant value.

The output curve features two distinct regions, a linear and saturation region. In the former, the current changes linearly with voltage, and it is valid for low drain voltages. At high drain voltages, the current reaches a saturation plateau and becomes independent of the voltage applied[5, 38, 39].

2.3.2 Transconductance

One of the main features of OECTs is their ability to amplify small changes of the gate voltage into large variations of the drain current[40]. The transconductance (g) is a key parameter of OECTs, because it measures the magnitude by which the transistors amplify the signal. Furthermore, this parameter is closely related to the analytical sensitivity, particularly when the devices are employed for biosensing[41]. The transconductance is defined as $g = \frac{\partial I_d}{\partial V_g}$ usually expressed in milli Siemens (mS), and is determined by calculating the first derivative of the transfer curve I_d-V_g.

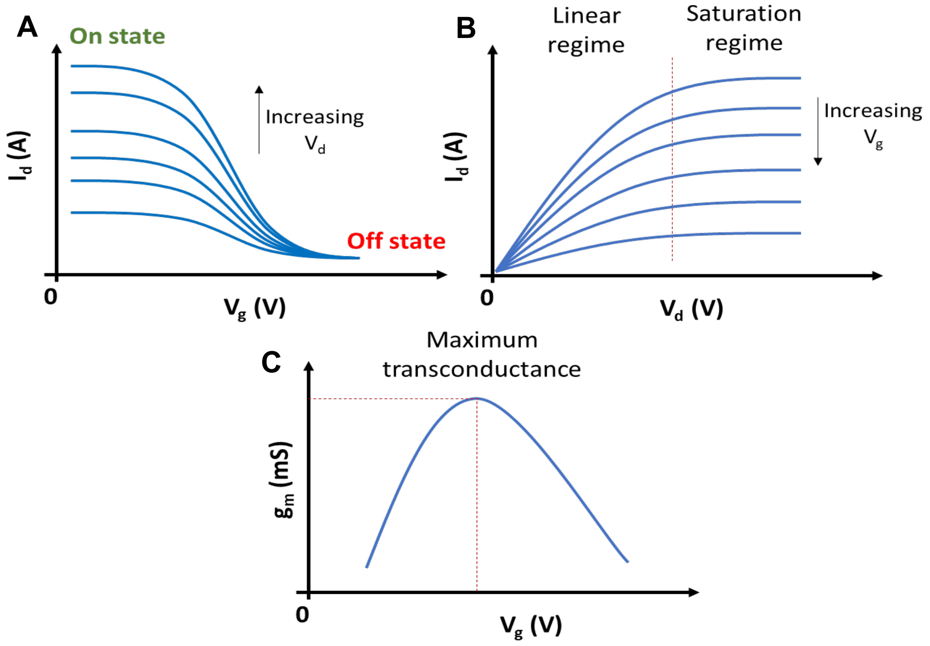

Figure 2.3. Typical characteristics of an OECT, A) transfer I_d-V_g curves, and B) output I_d-V_d, and C) transconductance-V_g plot.

The determination of the *g* for different values of V_g allows the construction of the transconductance curve *g*-V_g (Figure 2.3C), and provides a straightforward way to predict the performance of OECTs. The curve is also helpful in determining the maximum transconductance g_m and the corresponding drain and gate voltages for optimal operation of the OECT.

Several works have shown that the transconductance depends on the device geometry (Equation 2.2), particularly the width (W), length (L), and the thickness (d) of the channel[42-45]. For this reason, during the last decade, the effect of these parameters on the performance of thin-film OECTs have been extensively investigated[3, 46].

$$g_m \propto \frac{W.d}{L} \qquad \text{Equation 2.2}$$

2.3.3 ON-OFF current ratio

Another feature of OECTs is their ability to switch upon imposing a gate voltage. The response of the transistors shift from an ON state where a current is flowing between the source and the drain ($V_g = 0$ V), to an OFF state where the current is orders of magnitude smaller ($V_g > 0$ V). This switching ability is commonly quantified by determining the ratio of the nominal values of these currents. In general, the ON-OFF ratio of OECTs is lower compared to OFETs by 3-4 orders of magnitude[47]. However, the normalized ON-OFF ratio per gate voltage may, for instance, offer the OECT an attractive advantage over the OFET, since the former generally operates at low drain and gate voltages (< 1V), while the latter operates at voltages up to 30 V. This is true particularly for wearable biosensors and point-of-need devices, where the energy consumption of the device is equally important. High ON-OFF ratio is seldom the only parameter that counts when designing OECTs. For a specific application, very often, it is a matter of finding a compromise between different features such speed, stability, and energy consumption, which may not necessarily result in high ON-OFF ratio.

2.4 Modeling OECTs response

The objective of modeling the response of OECTs is, first, to predict quantitatively the drain current I_d as a function of the voltages applied V_d and V_g, geometry of the channel, and the properties of the conductive polymer. Secondly, to provide a direct way to determine key parameters of the device (i.e. charge carrier mobility, pinch-off voltage, etc.) from experimental data[48, 49]. Based on the well-established model of the FET, Bernards et al. have proposed a model that describes the steady-state and transient response of OECTs[5]. In the proposed model, illustrated in Figure 2.4, the OECT was divided into two elementary circuits: an ionic, and an electronic circuit. The ionic circuit was represented by a resistor in series with a capacitor. The role of the capacitor is to capture the transport of ions from the electrolyte into the channel when a gate voltage is applied. On the other hand, the electronic circuit, which represents the flow of the electronic current through the channel, was modeled by Ohm's law. Later, Rivnay et al.[42] suggested that the doping/dedoping of the channel, which results from applying a gate voltage, occurs over the bulk volume of the conductive polymer, giving rise to a volumetric capacitance[50-52]. The model, given by Equation 2.3, provides the expression of I_d in both regions: the linear regime where the current changes linearly with the gate voltage, and the saturation regime where I_d becomes constant and independent of V_g.

$$\begin{cases} \mathrm{I}_d = \dfrac{\mathrm{G}}{\mathrm{V}_p} \cdot \left(\mathrm{V_p} - \mathrm{V_g} + \dfrac{\mathrm{V_d}}{2}\right)\mathrm{V_d} \\ \mathrm{I}_d = \dfrac{\mathrm{G.V}_{sat}^2}{2\mathrm{V}_p} \end{cases}$$ Equation 2.3

Where $G = \mu . C^* \frac{W.t}{L}$ is the initial electrical conductance of the channel, μ is charge mobility ($cm^2.V^{-1}.s^{-1}$). C*, W, L, and t are the volumetric capacitance, width, length and thickness of the channel, respectively. V_p is the transistor pinch-off voltage, i.e., the value of V_g at which the channel is almost fully de-doped.

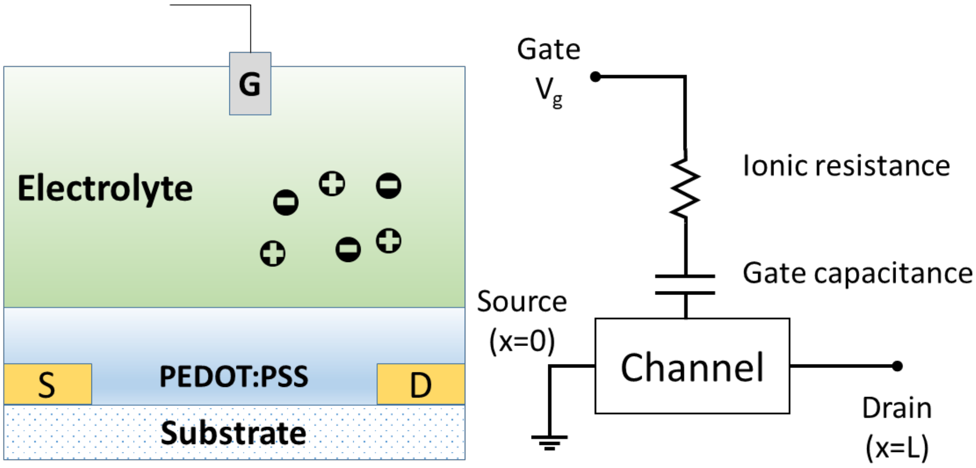

Figure 2.4. Equivalent ionic and electronic circuits of an OECT. Image adapted from Bernards et al.[5]

2.5 Fabrication techniques

Planar configuration is commonly adopted to build OECTs. In this configuration, the electrodes and the channel are patterned on the same planar substrate. Various technologies have been employed to design, deposit, and pattern OECTs with enhanced performance from solution-processed conducting polymers[22]. The major methods of fabrication are represented in Figure 2.5, and include, among many others, spin-coating, inkjet-printing, drop-casting, and dip coating. In addition,

Table 2.1 summarizes the main characteristics that facilitates the choice of the deposition method.

2.5.1 Spin-coating

Spin-coating is widely used for the deposition of the channel from solution processed conductive polymers[53, 54]. The technique allows the deposition of uniform thin films under centrifuge force relatively easily and reproducibly. PEDOT:PSS thin films in the range of 100 nm can be obtained by optimizing the viscosity and the composition of the conductive polymer, in addition to the rotation speed[55]. Spin-coating is usually combined with photolithography for deposition of the channel and the patterning of the electrodes. However, the major drawback of photolithography is that it involves the use of costly equipment and requires facilities with controlled environment such a clean room, both of which are expensive to maintain.

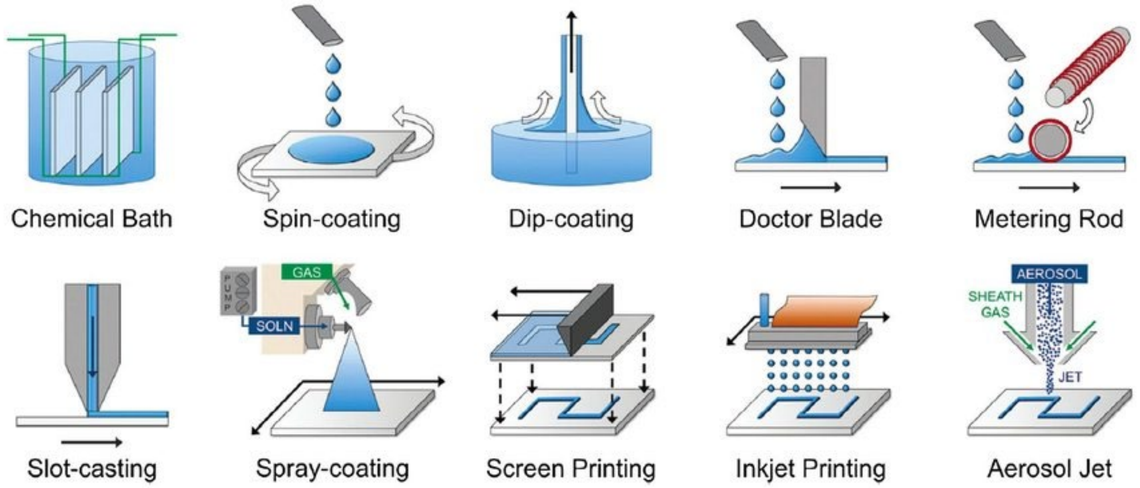

Figure 2.5. Techniques used for deposition of conducting polymer films. Image obtained from ref.[56]

2.5.2 Inkjet printing

This is one of the most popular techniques employed for large scale organic electronic devices[57]. Inkjet printing can be used to print the source/drain, the gate, and the channel for a wide range of biosensing applications [58, 59]. Different inks are commercially available for printing organic electronic devices including metallic and dielectric inks[60]. For optimal results, conductive polymer inks used for inkjet printing are expected to have a dynamic viscosity between 1-30 cP[61]. To achieve this viscosity without sacrificing performance, the formulation of conductive polymers inks is usually optimized by adding, solvents, viscosity modifiers, and/or adhesion enhancers[62]. Thick channels with a thickness ranging from hundreds of nanometers to few micrometers can be obtained by printing successive layers of the conductive polymer. The main advantages of inkjet printing over photolithography includes low-cost, convenience for flexible substrates such as paper and plastic, suitability for large area printing and mass production.

2.5.3 Drop casting

Drop casting is a simple technique that involves casting the CP solution on the surface of the substrate. As the solvent evaporates, a thin film is formed on the surface of the substrate. The method has been utilized in various applications including solar cells[63, 64], modified electrodes[65], and energy storage[66].The thickness of the film obtained depends on several parameters including, the volume drop-cast, wettability of the substrate, evaporation rate of the solvent, and drying conditions[67]. Films with a thickness of several micrometres can be achieved by successive drop cast and drying. The reproducibility and controllability of drop-casting method can be further enhanced by combining it with ultrasound. Eslamian et al. have reported an ultrasound assisted drop-casting method, which allows reproducible coatings of large surfaces by coalescence of multi-droplets[68, 69].

2.5.4 Dip coating

Dip-coating consists of dipping a substrate in a bath containing the conductive polymer solution. While the substrate is extracted vertically from the bath, a thin layer of the conductive polymer forms on the substrate. The method does not require expensive equipment, which makes it ideal for coating large areas. The thickness of the films prepared can be fairly controlled by modifying the viscosity of the solution, the roughness of the substrate, and the speed of withdrawal[70]. For this reason, dip coating is suitable for the fabrication of thin films, particularly, for solar cells[71] and self-assembled nanostructures[72]. In controlled conditions, it is possible to achieves thicknesses as low as 40 nm[73].

2.6 OECTs-based biochemical sensors

2.6.1 Importance of Hydrogen peroxide

Hydrogen peroxide H_2O_2 is one of the reactive oxygen species that has attracted a significant interest among the scientific community, because it is involved in several vital electrochemical and biological processes[74]. The molecule is considered as an important agent in intracellular signalling, metabolism, and oxidative stress[75, 76]. As a biochemical messenger, hydrogen peroxide plays an important role in the early response of the immune system to infections by eliminating pathogens and initiating inflammation[77]. Furthermore, at least 30 human enzymes, covering a wide range of functions, generate H_2O_2 as by-product[78]. Apart from its medical value, hydrogen peroxide is also utilized in industry for wood pulp, food oxidizing agent, water treatment, and textile bleaching[79]. Therefore, the detection of hydrogen peroxide is essential for medical and industrial applications.

Several catalytic materials have been employed for the electrochemical detection of H_2O_2, including platinum[80], reduced graphene oxide[81], and Prussian blue[82]. The molecule can undergo oxidation, reduction, and/or decomposition depending on the catalytic material used and the potential applied[83, 84].

$$\mathrm{H_2O_2} \leftrightharpoons \mathrm{O_2} + 2\mathrm{H^+} + 2\mathrm{e^-} \qquad \text{Equation 2.4}$$

$$\mathrm{H_2O_2} + 2\mathrm{H^+} + 2\mathrm{e^-} \leftrightharpoons 2\mathrm{H_2O} \qquad \text{Equation 2.5}$$

$$2\mathrm{H_2O_2} \leftrightharpoons 2\mathrm{H_2O} + \mathrm{O_2} \qquad \text{Equation 2.6}$$

Table 2.1. Main characteristics of Different deposition methods of conducting polymers.

Technique	**Large scale compatibility**	**Material waste**	**Thickness**	**Reproducibility**
Spin coating	-	Very high	< 1 µm	Very high
Inkjet printing	+	Low	>100 nm	High
Screen ptinting	+	Low	> 1 µm	High
Spray coating	+	Low to moderate	>1 µm	Moderate
Drop-casting	+	Low	>600 nm	Low to moderate
Dip-coating	+	Moderate	>1 µm	Low
Blade coating	+	Low to moderate	>1 µm	Low

2.6.2 Enzymatic sensors

Working principle

Enzymes are natural biomolecules that catalyse specific biochemical reactions in a selective and efficient way. For this reason, enzymes are extensively used to build biosensors that enable selective detection of a wide range of biomarkers[85]. A typical enzyme-based OECT consists of immobilizing the enzyme on the gate electrode[30, 86-89]. The drain current I_d is then monitored while the drain and gate voltages (V_d and V_g) are maintained at constant values. In the absence of the analyte, a steady-state current I_d is measured between the source and the drain electrodes. The addition of the analyte initiates a chemical reaction at the gate electrode, which induces a potential change at the gate/electrolyte interface, hence, altering the magnitude of I_d. The induced change in potential can be viewed as an effective gate voltage that modulates I_d[90, 91]. Therefore, a relationship can be established either between I_d and the concentration of the analyte, or between the gate voltage and the concentration of the analyte.

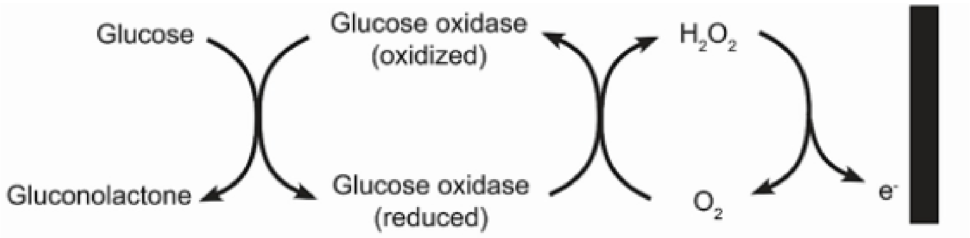

Figure 2.6. Detection mechanism of an enzymatic OECT for glucose.

The detection of relevant biomolecules such as glucose, cholesterol, and lactate is achieved by taking advantage of the specificity of their corresponding enzymes glucose oxidase (GOx), cholesterol oxidase (ChOx), and lactate oxidase (LOx), respectively[92-95]. These enzymes, which are known as “oxidoreductase” enzymes, catalyze the oxidation of their substrate, and generate hydrogen peroxide. For instance, an OECT glucose sensor can be built by physically entrapping the GOx on the surface of a platinum electrode gate[96]. As described in Figure 2.6, the glucose is oxidised to gluconic acid while GOx is reduced, producing two electrons and two protons. The next step involves the reduction of oxygen in the presence of the protons and electrons generated earlier, and the formation of hydrogen peroxide, while GOx is oxidised back to its original state. The hydrogen peroxide is then oxidised on the surface of platinum to water.

Immobilization techniques

Different techniques have been used to immobilize enzymes on the gate electrode including, physical adsorption, entrapment, and covalent bonding (Figure 2.7).[97] The objective is to immobilize the enzyme in a way that prevents any possible leak, and ensures an easy access to the analyte while maintaining the activity of the enzyme[98]. The simplest, but less efficient way of immobilization, is achieved through physical adsorption of the enzyme on the surface of the electrode by means of weak forces, such as electrostatic forces and hydrogen bonds[99]. On the other hand, the most common immobilization method consists of entrapping the enzyme in a polymeric layer. Nafion and chitosan are widely used for this purpose because of their biocompatibility, porosity and commercial availability[100]. The immobilization of enzymes can also be realized chemically, by either crosslinking or covalently binding the enzyme to a chemically modified surface through specific chemical groups[101]. The main drawback of this method is that chemical binding may alter the structure of the enzyme and hinders the access of the substrate to the active sites, hence, reducing the enzyme activity.

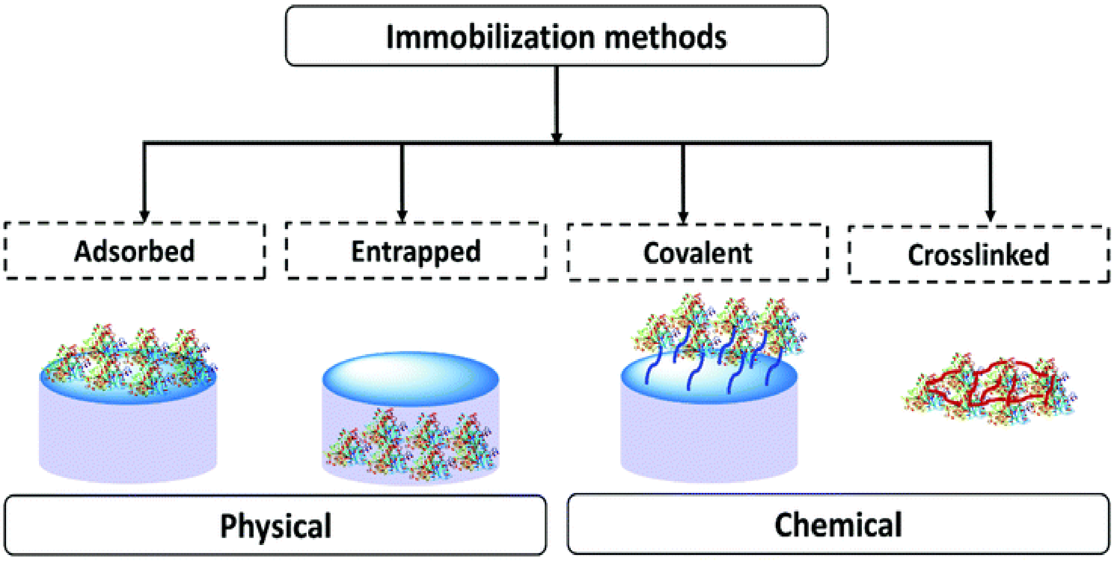

Figure 2.7. Different techniques used for immobilization of enzymes. Image obtained from ref.[97]

Apart from the immobilization method, the activity of enzymes is effected by three major factors: pH, temperature, and the concentration of the enzyme[102]. Acidic or alkaline environments may ionize some functional groups on the enzyme, which alters the enzyme-substrate interactions. For this reason, the optimal pH is typically near the isoelectric point of the enzyme, that is, the pH value at which the net charge of the enzyme is zero. On the other hand, high temperature causes the denaturation of proteins and enzymes, which leads to significant loss of their activity. As for the concentration, high enzyme loading may prevent the substrate from reaching the active sites. Therefore, an optimization step is usually necessary to determine the optimal conditions for high analytical performance.

2.6.3 Ion-selective OECTs

PEDOT:PSS-based OECTs are inherently sensitive to electrolytes, since ions can dope or de-dope the conductive polymer via injection (or extraction) of cations into (out of) the channel[103]. To provide OECTs with selective detection to a particular ion, the channel is either functionalized with an ion-selective membrane[32, 104], or functionalized with functional groups that interact directly with the target ion[105].

Ion-selective membranes are a well-established technology in potentiometry that consists of four basic elements: ionophore, ion-exchanger, plasticizer, and polymer matrix (ex. polyvinyl chloride). In a typical IS-OECT, as described in Figure 2.8, the ion-selective membrane is located on top of the organic polymer channel and in direct contact with electrolyte. As in ion selective electrodes, the liquid membrane can be readily deposited by simple drop casting method and left to dry. Under suitable drain and gate voltages, the cations of interest bind selectively to the ionophore and pass through the membrane, leading to the dedoping of the channel[106]. Several works have reported the use OECTs for the detection of ions including pH[107], chloride[108], calcium[109], potassium. Table 2.2 shows a selection of the most recent works that tackled ion-selective OECTs and their key performances.

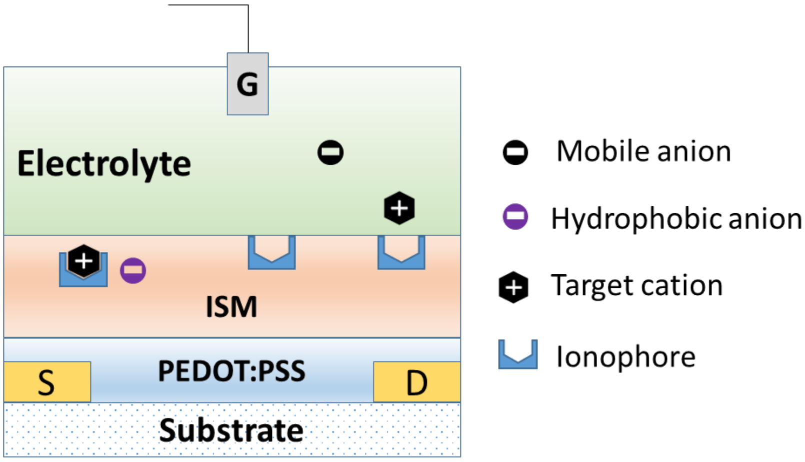

Figure 2.8. Description of an ion-selective OECT. Image adapted from ref.[110]

Wustoni et al. have reported an OECT capable of detecting K^+ and Na^+, with a selective conductive polymer prepared by simultaneous electropolymerization of EDOT and different crown-ethers[105]. Gualandi et al. have developed an OECT for chloride sensing via the electrodeposition of Ag/AgCl on the gate the channel[111]. The sensor was employed successfully to test chloride in different water samples, and was used also as textile sensor for the detection of chloride is sweat.

Table 2.2. Recent works published about ion-selective OECTs.

Channel	**Device**	**Analyte**	**Sensitivity**	**Linear range**	**Voltages (Vg/Vd)**	**Ref.**
PEDOT:PSS	IS-OECT	K^+	46 µA.dec^{-1}	-4 to -1	0 V / -0.7 V	[106]
PEDOT:PSS	Textile IS-OECT	Ca^+	6.64 M^{-1}	-4 to -1	1 V /-0.05 V	[32]
PEDOT:PSS	Multiplex IS-OECT	NH_4^+, Ca^+	≈20 µA.dec^{-1} ≈12 µA.dec^{-1}	-5 to -1	0 V / +0.2 V	[109]
PEDOT:PSS	IS-OECT	K^+	233 µA.dec^{-1}	-4 to -1	0.2 V / -0.4 V	[112]
PEDOT:PSS or PEDOT:PSS/AgCl	OECT	Cl^-	0.05 dec^{-1}	-4 to 0	0 V / 0.05 V	[108]

2.7 Chemiresistive sensors for H_2O_2 detection

Chemiresistor were originally designed as gas sensors, in which the sensing material was made of a metal oxide semiconductor that detects CO_2 at high temperatures. Chemiresistors have rapidly found their route to (bio) chemical sensing in aqueous solutions. The devices are now regarded as a subgroup of (bio) chemical sensors wherein the electrical resistance of a sensitive conducting material is monitored, while the material is in direct contact with the analyte of interest. The conductive material is deposited between two conducting electrodes separated by a small gap. Compared to OECTs, chemiresistors offer numerous advantages such as simple design and detection mechanism, as well as ease of customization. In addition to metal oxides, a variety of sensing materials have been used to construct the chemiresistive channel, including conducting polymers and their composites, graphene, and carbon nanotubes.

2.7.1 Conducting polymer composite chemiresistors

Conducting polymers (CPs) are interesting materials for building chemiresistors, since they can be deposited at room temperature via simple deposition methods as mentioned earlier. An effective way to impart CPs with catalytic properties is to create composites in which CPs are combined with nanomaterial that have the desired catalytic properties. Therefore, the composite obtained demonstrates both electrical and catalytic properties.

The excellent electrochemical and charge transfer properties of PEDOT:PSS allows it to be utilized for bioelectronics devices not only in pristine form, but also as a composite material in combination with metallic or carbon nanomaterials.[113] In addition, several works have reported the functionalization of PEDOT:PSS chain with different biomolecules for the selective detection of DNA, proteins, and enzymes. Various reviews papers are devoted to PEDOT:PSS composites and their applications.[114-116]

Chemiresistors can operate in either a resistance mode or current mode. In the former, a constant DC current is applied between the electrodes, and the voltage is measured. According to Ohm law, the ratio of the voltage and current allows the accurate measurement of the resistance. In the current mode, a constant DC voltage is applied while the current is measured.

The resistance is commonly measured either by two-point or four-point methods. In two-point method, the total resistance obtained include both the resistance of the bulk channel and the resistance of the contacts. This becomes an issue when the resistance of the contacts are higher compared to the bulk channel.

2.8 Analytical performance of biosensors

The study of the analytical performance of sensors is carried about by determining a number of attributes that informs about whether the device will satisfactorily fulfil its primary function. These attributes include sensitivity, selectivity, limit of detection, linear range, and response time.

Sensitivity

Sensitivity is the ratio between the measured signal and the concentration of the target analyte. The sensitivity shows how much the response of a sensor changes when a known quantity of the analyte is added. It can be determined from a calibration curve by measuring the response of the sensor to a known concentration of the analyte. In this case, sensitivity represents the slop of the calibration curve within the linear range.

Linear range

It refers to the concentration interval of the analyte in which the response of the sensor is linear with respect to the measured response.

Selectivity

It indicates whether a sensor can respond selectively to the target analyte or it responds also to other analytes.

Limit of detection (LOD)

The LOD is the smallest concentration of the analyte that the sensor can detect under specific conditions with reasonable certainty. The method used for the determination of the LOD in potentiometric sensors was adopted for OECTs and chemiresistors. In this method, the LOD corresponds to the intersection of the two extrapolated linear ranges (lower and higher) of the calibration curve[117].

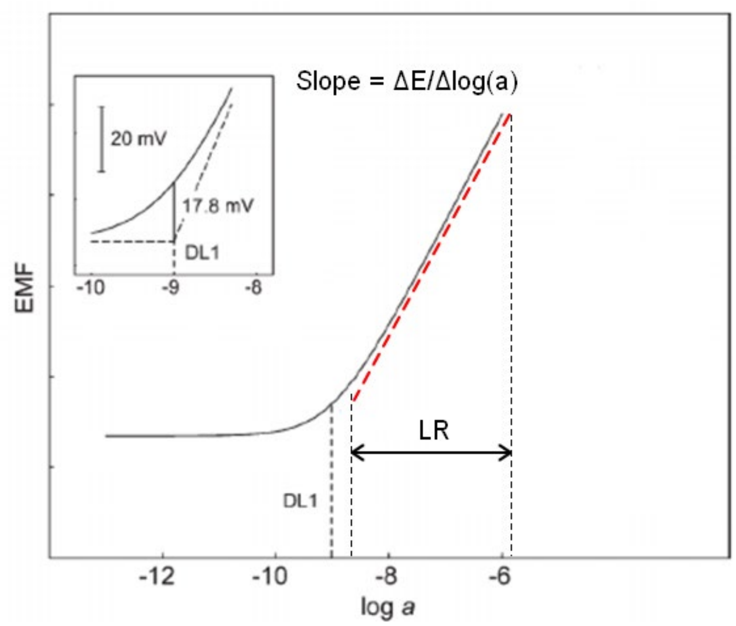

Figure 2.9. Graph showing the determination of the detection limit (DL), linear range (LR), and sensitivity (slope) from a calibration curve obtained via potentiometry. Image adapted from ref.[117]

Response time

It is defined as the time needed for the sensor to reach 90% of the total response when a specific concentration of the analyte is added.

Recovery time

It indicates the time it takes the sensor to reach its initial baseline when the concentration changes from a certain value to zero.

2.9 References

[1] Rivnay, J.; Inal, S.; Salleo, A.; et al., *Nat Rev Mater*, **2018**, 3, 1-14.

[2] Hütter, P. C.; Rothländer, T.; Haase, A.; et al., *Appl Phys Lett*, **2013**, 103, 1-5.

[3] Friedlein, J. T.; McLeod, R. R.; Rivnay, J., *Org Electron*, **2018**, 63, 398-414.

[4] Paulsen, B. D.; Tybrandt, K.; Stavrinidou, E.; et al., *Nat Mater*, **2020**, 19, 13-26.

[5] Bernards, D. A.; Malliaras, G. G., *Adv Funct Mater*, **2007**, 17, 3538-3544.

[6] Facchetti, A., *Chem Mater*, **2010**, 23, 733-758.

[7] Heeger, A. J., *J Phys Chem B*, **2001**, 105, 8475-8491.

[8] Roth, S.; Bleier, H.; Pukacki, W., *Faraday Discuss Chem Soc*, **1989**, 88, 223-233.

[9] K, N.; Rout, C. S., *RSC Adv*, **2021**, 11, 5659-5697.

[10] Le, T. H.; Kim, Y.; Yoon, H., *Polymers (Basel)*, **2017**, 9, 150.

[11] Bredas, J. L.; Street, G. B., *Acc Chem Res*, **2002**, 18, 309-315.

[12] Moliton, A.; Hiorns, R. C., *Polym Int*, **2004**, 53, 1397-1412.

[13] A. G. MacDiarmid; R. J. Mammone; R. B. Kaner; et al., *Philosophical Transactions of the Royal Society of London Series A: Mathematical and Physical Sciences*, **1997**, 314, 3-15.

[14] Stöcker, T.; Köhler, A.; Moos, R., *J Polym Sci, Part B: Polym Phys*, **2012**, 50, 976-983.

[15] Rwei, S. P.; Lee, Y. H.; Shiu, J. W.; et al., *Polymers (Basel)*, **2019**, 11, 134.

[16] Meng, W.; Ge, R.; Li, Z.; et al., *ACS Appl Mater Interfaces*, **2015**, 7, 14089-14094.

[17] Deetuam, C.; Weise, D.; Samthong, C.; et al., *J Appl Polym Sci*, **2015**, 132, 42108.

[18] Cui, H.-Q.; Peng, R.-X.; Song, W.; et al., *Chin J Polym Sci*, **2019**, 37, 760-766.

[19] Onorato, A.; Invernale, M. A.; Berghorn, I. D.; et al., *Synth Met*, **2010**, 160, 2284-2289.

[20] Yun, D.-J.; Jung, J.; Kim, K.-H.; et al., *Appl Surf Sci*, **2021**, 553, 149584.

[21] Song, J.; Ma, G.; Qin, F.; et al., *Polymers (Basel)*, **2020**, 12, 450.

[22] Wen, Y.; Xu, J., *J Polym Sci, Part A: Polym Chem*, **2017**, 55, 1121-1150.

[23] Koch, N.; Elschner, A.; Schwartz, J.; et al., *Appl Phys Lett*, **2003**, 82, 2281-2283.

[24] Xu, Y.; Li, Y.; Li, S.; et al., *Adv Funct Mater*, **2019**, 30, 1-23.

[25] Kaphle, V.; Liu, S.; Al-Shadeedi, A.; et al., *Adv Mater*, **2016**, 28, 8766-8770.

[26] Tarabella, G.; Santato, C.; Yang, S. Y.; et al., *Appl Phys Lett*, **2010**, 97, 123304.

[27] Picca, R. A.; Manoli, K.; Macchia, E.; et al., *Adv Funct Mater*, **2019**, 30, 1904513.

[28] Torricelli, F.; Adrahtas, D. Z.; Bao, Z.; et al., *Nat Rev Methods Primers*, **2021**, 1, 2-24.

[29] Giovannitti, A.; Nielsen, C. B.; Sbircea, D. T.; et al., *Nat Commun*, **2016**, 7, 13066.

[30] Macchia, E.; Romele, P.; Manoli, K.; et al., *Flex Print Electron*, **2018**, 3, 034002.

[31] Liu, D.; Tian, X.; Bai, J.; et al., *Adv Sci (Weinh)*, **2022**, 9, e2203418.

[32] Coppedè, N.; Giannetto, M.; Villani, M.; et al., *Org Electron*, **2020**, 78, 105579.

[33] Ait Yazza, A.; Blondeau, P.; Andrade, F. J., *ACS Appl Electron Mater*, **2021**, 3, 1886-1895.

[34] Abdollahi-Aghdam, A.; Majidi, M. R.; Omidi, Y., *Bioimpacts*, **2018**, 8, 237-240.

[35] Ghosh, R.; Gopalakrishnan, S.; Savitha, R.; et al., *Sci Rep*, **2019**, 9, 7896.

[36] Bihar, E.; Deng, Y.; Miyake, T.; et al., *Sci Rep*, **2016**, 6, 27582.

[37] Bushra, K. A.; Prasad, K. S., *Talanta*, **2022**, 239, 123085.

[38] Robinson, N. D.; Svensson, P.-O.; Nilsson, D.; et al., *J Electrochem Soc*, **2006**, 153, H39-H44.

[39] Kaphle, V.; Paudel, P. R.; Dahal, D.; et al., *Nat Commun*, **2020**, 11, 2515.

[40] Khodagholy, D.; Rivnay, J.; Sessolo, M.; et al., *Nat Commun*, **2013**, 4, 2133.

[41] Bai, L.; Elosegui, C. G.; Li, W.; et al., *Front Chem*, **2019**, 7, 313.

[42] Rivnay, J.; Leleux, P.; Ferro, M.; et al., *Sci Adv*, **2015**, 1, e1400251.

[43] Fan, J.; Rezaie, S. S.; Facchini-Rakovich, M.; et al., *Org Electron*, **2019**, 66, 148-155.

[44] Polyravas, A. G.; Schaefer, N.; Curto, V. F.; et al., *Appl Phys Lett*, **2020**, 117, 073302.

[45] Paudel, P. R.; Kaphle, V.; Dahal, D.; et al., *Adv Funct Mater*, **2020**, 31, 2004939.

[46] Kumar, P.; Yi, Z.; Zhang, S.; et al., *Applied Physics Letters*, **2015**, 107, 6-11.

[47] Tang, W.; Huang, Y.; Han, L.; et al., *J Mater Chem C*, **2019**, 7, 790-808.

[48] Paudel, P. R.; Tropp, J.; Kaphle, V.; et al., *J Mater Chem C*, **2021**, 9, 9761-9790.

[49] Colucci, R.; Barbosa, H. F. d. P.; Günther, F.; et al., *Flex Print Electron*, **2020**, 5, 013001.

[50] Proctor, C. M.; Rivnay, J.; Malliaras, G. G., *J Polym Sci, Part B: Polym Phys*, **2016**, 54, 1433-1436.

[51] Sahalianov, I.; Singh, S. K.; Tybrandt, K.; et al., *RSC Adv*, **2019**, 9, 42498-42508.

[52] Sahalianov, I.; Say, M. G.; Abdullaeva, O. S.; et al., *ACS Appl Energy Mater*, **2021**, 4, 8629-8640.

[53] Valtakari, D.; Liu, J.; Kumar, V.; et al., *Nanoscale Res Lett*, **2015**, 10, 386.

[54] Vedovatte, R. M.; Saccardo, M. C.; Costa, E. L.; et al., *J Mater Sci - Mater Electron*, **2019**, 31, 317-323.

[55] Yan, H.; Jo, T.; Okuzaki, H., *Polym J*, **2009**, 41, 1028-1029.

[56] Pasquarelli, R. M.; Ginley, D. S.; O'Hayre, R., *Chem Soc Rev*, **2011**, 40, 5406–5441.

[57] Teichler, A.; Perelaer, J.; Schubert, U. S., *J Mater Chem C*, **2013**, 1, 1910–1925.

[58] Basiricò, L.; Cosseddu, P.; Scidà, A.; et al., *Org Electron*, **2012**, 13, 244-248.

[59] Manoli, K.; Magliulo, M.; Mulla, M. Y.; et al., *Angew Chem Int Ed Engl*, **2015**, 54, 12562-12576.

[60] Nayak, L.; Mohanty, S.; Nayak, S. K.; et al., *J Mater Chem C*, **2019**, 7, 8771-8795.

[61] Lemarchand, J.; Bridonneau, N.; Battaglini, N.; et al., *Angew Chem Int Ed Engl*, **2022**, 61, e202200166.

[62] Dybowska-Sarapuk, L.; Kielbasinski, K.; Arazna, A.; et al., *Nanomaterials (Basel)*, **2018**, 8, 602.

[63] Zuo, C.; Scully, A. D.; Tan, W. L.; et al., *Commun Mater*, **2020**, 1, 1-10.

[64] Zuo, C.; Ding, L., *Angew Chem Int Ed Engl*, **2021**, 60, 11242-11246.

[65] Perez-Rafols, C.; Bastos-Arrieta, J.; Serrano, N.; et al., *Sensors (Basel)*, **2017**, 17, 1458.

[66] Cha, S. M.; Nagaraju, G.; Chandra Sekhar, S.; et al., *J Mater Chem A*, **2017**, 5, 2224-2234.

[67] Kaliyaraj Selva Kumar, A.; Zhang, Y.; Li, D.; et al., *Electrochem Commun*, **2020**, 121, 106867.

[68] Eslamian, M.; Zabihi, F., *Nanoscale Res Lett*, **2015**, 10, 462.

[69] Eslamian, M., *Nanomicro Lett*, **2017**, 9, 3.

[70] Grosso, D., *J Mater Chem*, **2011**, 21, 17033.

[71] Adnan, M.; Lee, J. K., *Sci Rep*, **2018**, 8, 2168.

[72] Garcia Nunez, C.; Navaraj, W. T.; Liu, F.; et al., *ACS Appl Mater Interfaces*, **2018**, 10, 3058-3068.

[73] Kuemmel, M.; Allouche, J.; Nicole, L.; et al., *Chem Mater*, **2007**, 19, 3717-3725.

[74] Lushchak, V. I., *Chem Biol Interact*, **2014**, 224, 164-175.

[75] Veal, E. A.; Day, A. M.; Morgan, B. A., *Mol Cell*, **2007**, 26, 1-14.

[76] Sies, H., *Redox Biol*, **2017**, 11, 613-619.

[77] Sies, H., *J Biol Chem*, **2014**, 289, 8735-8741.

[78] Go, Y. M.; Chandler, J. D.; Jones, D. P., *Free Radic Biol Med*, **2015**, 84, 227-245.

[79] Larrañaga, M. D.; Lewis, R. J.; Lewis, R. A. Hawley's Condensed Chemical Dictionary. 16th ed., Wiley, 2016.

[80] Guo, X.; Cao, Q.; Liu, Y.; et al., *Anal Chem*, **2020**, 92, 908-915.

[81] Liao, C.; Zhang, M.; Niu, L.; et al., *J Mater Chem B*, **2013**, 1, 3820-3829.

[82] Currano, L. J.; Sage, F. C.; Hagedon, M.; et al., *Sci Rep*, **2018**, 8, 15890.

[83] Katsounaros, I.; Schneider, W. B.; Meier, J. C.; et al., *Phys Chem Chem Phys*, **2012**, 14, 7384-7391.

[84] Shao, M.; Chang, Q.; Dodelet, J. P.; et al., *Chem Rev*, **2016**, 116, 3594-3657.

[85] Rocchitta, G.; Spanu, A.; Babudieri, S.; et al., *Sensors (Basel)*, **2016**, 16, 780.

[86] Liao, C., *MPhil Thesis*, **2014**,

[87] Leleux, P.; Rivnay, J.; Lonjaret, T.; et al., *Adv Healthc Mater*, **2015**, 4, 142-147.

[88] Strakosas, X.; Bongo, M.; Owens, R. M., *J Appl Polym Sci*, **2015**, 132, 41735.

[89] Yang, A.; Li, Y.; Yang, C.; et al., *Adv Mater*, **2018**, 30, e1800051.

[90] Bernards, D. A.; Macaya, D. J.; Nikolou, M.; et al., *J Mater Chem*, **2008**, 18, 116-120.

[91] Venkatraman, V.; Friedlein, J. T.; Giovannitti, A.; et al., *Adv Sci (Weinh)*, **2018**, 5, 1800453.

[92] Nguyen, H. H.; Lee, S. H.; Lee, U. J.; et al., *Materials (Basel)*, **2019**, 12, 121.

[93] Lamas-Ardisana, P. J.; Loaiza, O. A.; Anorga, L.; et al., *Biosens Bioelectron*, **2014**, 56, 345-351.

[94] Li, J.; Peng, T.; Peng, Y., *Electroanalysis*, **2003**, 15, 1031-1037.

[95] Nair, R. R., *Flex Print Electron*, **2020**, 5, 015001.

[96] Tang, H.; Yan, F.; Lin, P.; et al., *Adv Funct Mater*, **2011**, 21, 2264-2272.

[97] Imam, H. T.; Marr, P. C.; Marr, A. C., *Green Chem*, **2021**, 23, 4980-5005.

[98] Mohamad, N. R.; Marzuki, N. H.; Buang, N. A.; et al., *Biotechnol Biotechnol Equip*, **2015**, 29, 205-220.

[99] Jesionowski, T.; Zdarta, J.; Krajewska, B., *Adsorption*, **2014**, 20, 801-821.

[100] Guzik, U.; Hupert-Kocurek, K.; Wojcieszynska, D., *Molecules*, **2014**, 19, 8995-9018.

[101] Govardhan, C. P., *Curr Opin Biotechnol*, **1999**, 10, 331-335.

[102] Robinson, P. K., *Essays Biochem*, **2015**, 59, 1-41.

[103] Rebetez, G.; Bardagot, O.; Affolter, J.; et al., *Adv Funct Mater*, **2021**, 32, 2105821.

[104] Romele, P.; Gkoupidenis, P.; Koutsouras, D. A.; et al., *Nat Commun*, **2020**, 11, 3743.

[105] Wustoni, S.; Combe, C.; Ohayon, D.; et al., *Adv Funct Mater*, **2019**, 29, 1-10.

[106] Sessolo, M.; Rivnay, J.; Bandiello, E.; et al., *Adv Mater*, **2014**, 26, 4803-4807.

[107] Scheiblin, G.; Coppard, R.; Owens, R. M.; et al., *Adv Mater Technol*, **2017**, 2, 1-5.

[108] Gualandi, I.; Tessarolo, M.; Mariani, F.; et al., *Front Bioeng Biotechnol*, **2019**, 7, 1-13.

[109] Keene, S. T.; Fogarty, D.; Cooke, R.; et al., *Adv Healthc Mater*, **2019**, 8, e1901321.

[110] Pierre, A.; Doris, S. E.; Lujan, R.; et al., *Adv Mater Technol*, **2019**, 4, 1800577.

[111] Gualandi, I.; Tessarolo, M.; Mariani, F.; et al., *Sens Actuators B: Chem*, **2018**, 273, 834-841.

[112] Han, S.; Yamamoto, S.; Polyravas, A. G.; et al., *Adv Mater*, **2020**, 32, e2004790.

[113] Jayaram, A. K.; Pitsalidis, C.; Tan, E.; et al., *Front Chem*, **2019**, 7, 363.

[114] Yang, J.; Liu, Y.; Liu, S.; et al., *Mater Chem Front*, **2017**, 1, 251-268.

[115] Zhao, Z.; Richardson, G. F.; Meng, Q.; et al., *Nanotechnology*, **2016**, 27, 042001.

[116] Kaur, G.; Adhikari, R.; Cass, P.; et al., *RSC Advances*, **2015**, 5, 37553-37567.

[117] Bakker, E.; Pretsch, E., *Trends Analyt Chem*, **2005**, 24, 199-207.

3 Experimental

Summary

This chapter will describe materials, processes and instrumentation that are common to all the experiments or that appear in many different chapters. Particular experimental aspects will be presented in each chapter.

3.1 Materials

Paper

The paper that served as substrate to build the OECTs and chemiresistors was microporous luster photography-quality paper with a weight of 200 g/m^2, thickness 205 ± 12 µm. The paper was purchased from a local supplier.

Nanomaterials

The platinum nanoparticles were stabilized by triphenylphosphine (PPh_3) and had an average diameter of 2.9 ± 0.9 nm. The nanoparticles were provided by the group of Inorganic Chemistry from Universitat Rovira i Virgili and were prepared according to reference [1].

Reduced. graphene oxide powder (rGO) containing, Carbon ≥75 wt. %, Nitrogen >5 wt. %, and Oxygen <22 wt. %, was purchased from Sigma Aldrich.

Zinc oxide nanoparticle suspension 2.5 wt. % with particle size between 8-16 nm was purchased from Sigma Aldrich.

Other reagents

All chemicals used were analytical grade and were purchased from Sigma-Aldrich (Merck, Spain). 3-4% aqueous solution of high conductivity grade PEDOT:PSS was used for making the conductive films. Fresh H_2O_2 standard solutions were prepared daily from a commercial 30 % (v/v) stock. A solution of 5 % wt Nafion® in aliphatic alcohols and water (15-20 % water) was used to make the gate electrode. Glucose Oxidase (from Aspergillus Niger Type X-S) lyophilized powder, 100-250 kU/g was used to prepare a stock solution in deionized water (20 mg/mL). Phosphate-buffered saline solution (PBS 0.1 M at pH = 7.4) was prepared by dissolving 0.100 M Na_2HPO_4, 0.018 M KH_2PO_4, 0.1 M NaCl and 0.003 M KCl. All solutions were prepared using doubly deionized water (Millipore Corporation, Bedford, MA).

3.2 Instrumentation

This section includes the most important instruments that were employed for the construction and the characterization of the sensors studied through this thesis.

Keysight E3631A

Triple Output Power Supply that generates 6V, 5A & ±25V, 1A. It is low-noise power supply that was used primarily for the electrical characterization of OECTs and chemiresistors, especially, for establishing the transfer curves and the output responses. The device was controlled by a desktop computer via a home-made program.

Keithley 6514 & Keithley 2100

The device are digital high-performance system electrometer. They were used to measure voltage, current, resistance and charge.

CHI 660C Electrochemical Workstation

It is a general purpose workstation for electrochemical measurements. It supports, among others, a number of electrochemical methods such as, cyclic voltammetry (CV), chronoamperometry, and Electrochemical Impedance Spectroscopy (EIS). The system is equipped with a fast digital function generator, high speed data acquisition circuitry, potentiostat, and a galvanostat capable of controlling potentials of ±10 V, and currents of ±250 mA.[2]

Transmission electron microscope (TEM) JEOL 1011, Japan

The JEM-1011 is a compact high performance TEM with advanced features and functions. The microscope is equipped with high contrast objective lens polepiece, which allows it to deliver images with high contrast, brightness, and optimum resolution. The microscope can operate at relatively high voltages up to 100 kV, and utilizes a tungsten filament to generate the electron beam. TEM was used for the characterization of nanoparticles dispersions.

Field Emission Scanning Electron Microscope (FESEM) Scios™ 2 DualBeam -Thermo Scientific, USA

The Thermo Scientific Scios 2 DualBeam is a microscope with ultra-high-resolution equipped with ion beam scanning electron microscopy (FIB-SEM) system based on gallium, which enables it to carry out sample preparation of a wide range of samples. The FESEM comes also with an X-ray spectroscopy detector, a micromanipulator and 4 gas injector systems that enhances its ability to visualize nano-structures.

Sputtering system ATC Orion UHV from AJA International Inc, Massachusetts - USA

The device is a magnetron sputtering system that that operates under vacuum, and utilizes a magnetic field to accelerate positive ions generated from a plasma source. The accelerated ions bombard a target sample, which results in the deposition of films with controlled deposition rate. The device was employed for sputtering gold and platinum on paper substrate to make source/drain and gate electrodes, respectively. Below are the settings used for the deposition of gold and platinum.

For depositing 100 nm gold in two steps process: strike (Pressure= 30 mTorr, Gas flow rate = 20 sccm (Argon), Power= 50W, Time= 10 s), and deposition (Pressure= 3 mTorr, Gas flow rate = 20 sccm (Argon), Power= 200 W, Coat time= 384 s).

For sputtering 100 nm platinum, the parameters of the two steps were: strike Pressure= 30 mTorr, Gas flow rate = 20 sccm, Power= 30 W, Time= 5 s), and deposition (Pressure=3 mTorr, Gas flow rate = 20 sccm, Power= 300 W, Coat time= 256 s).

3.3 Characterization

3.3.1 Electrical characterization

Output and transfer curves

The electrical characterization of the OECTs was performed in a standard solution of NaCl (0.1 M), in 5 mL test cell. The tests were conducted using an Ag/AgCl pallet as a gate electrode, if not otherwise specified. Figure 3.1A shows the measurement setup used for the characterization of the devices. The output curve (I-V_d) and the transfer curve (I-V_g) were automatically obtained by applying voltage sweeps using a low-noise power supply, and the current was measured using a digital electrometer. The two instruments were controlled and synchronized by a customized program. The data were recorded for further analysis using Excel and Originlab. The source and the drain were connected vertically to two crocodile clips, while the Ag/AgCl el softwareectrode in connected to a third crocodile clip. Dry characterization of the channels was conducted in air at room temperature using the same setup, without gate electrode and without electrolyte.

Measurement of the resistance

Four-point probe method was employed to measure the resistance of the PEDOT:PSS channels, with Keithley 2100, at dry and wet conditions. It consists of applying a known

DC current between two outer probes, and measuring the voltage drop between two inner probes. The method allows accurate measurements of the resistance by eliminating the effect of contact resistance. Knowing the geometry of the channel, the sheet resistance R_s expressed in Ω/square (to avoid confusion with bulk resistance), can be calculated from the measured resistance using Equation 3.1.

$$R_s = R \times \frac{W}{L}$$ Equation 3.1

Where R is the resistance in Ω, W and L are the width and the length of the channel in mm, respectively.

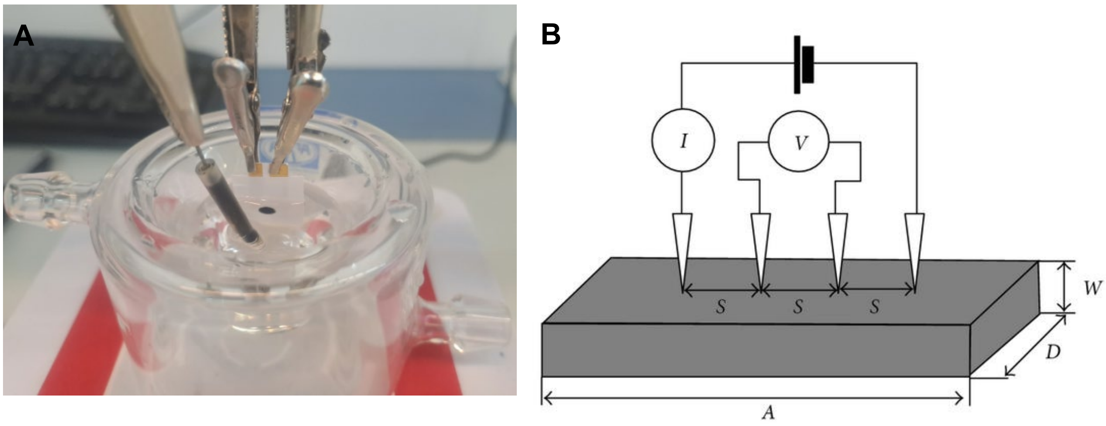

Figure 3.1. A) Measurement setup used for the characterization of the devices. B) Schematic of four-point probe method for the measurement of the resistance.

3.3.2 Electrochemical characterization

Cyclic voltammetry (CV)

Cyclic voltammetry of the channels was conducted in PBS (0.1 M), with or without 5 mM of potassium ferri/ferrocynide $[Fe(CN)_6]^{3-/4-}$ redox couple, in a three-electrode cell using CHI 660C Electrochemical Workstation. The source and the drain were shorted and connected to the working electrode terminal. A platinum wire and Ag/AgCl electrode were used as counter and reference electrodes, respectively. Figure 3.2 represents a typical cyclic voltammogram of an electroactive specie obtained by varying linearly the potential applied versus the reference electrode, and recording the current that flows through the counter electrode. The CV displays two peak currents representing the oxidation and reduction peaks I_{pa} and I_{pc}, which correspond to the anodic and cathodic currents, respectively.

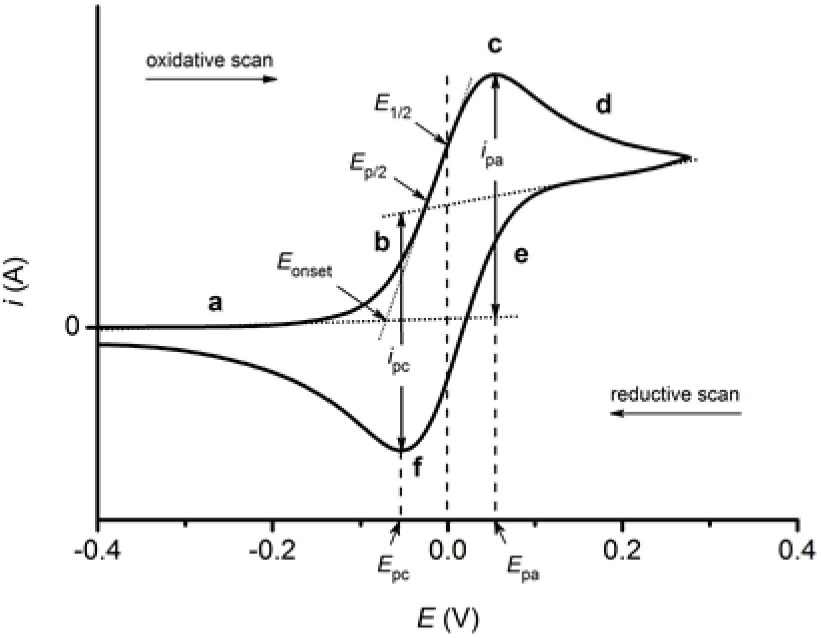

Figure 3.2. Example of a cyclic voltammogram showing duck-like shape with an oxidation/reduction peaks, and the different parameters of that can be extracted from the curve.

Electrochemical Impedance Spectroscopy (EIS)

Electrochemical impedance measurements were also carried out in a three-electrode cell using CHI 660C Electrochemical Workstation, with the same configuration described in the cyclic voltammetry section.

The tests were conducted in PBS (0.1 M), unless specified otherwise. A small alternative voltage with a magnitude of 5 mV was applied to the working electrode, and the impedance was recorded as a function of frequency. Finally, the obtained data were fitted to a simple Randles circuit to extract the corresponding capacitance and resistance.

The impedance, widely employed in electronics and electrical engineering, is a general concept that refers to the ability of an electrical circuit to resist (or impede) the flow of an alternating current (AC). The impedance denoted by “Z” and has the same unit as the electrical resistance (ohm), is expressed as a complex number that has two parts: real and imaginary parts.

EIS is widely used to characterize and study electrochemical systems and their interfaces. It consists of applying small AC voltages to the system under study, and analysing the resulting AC current generated by the system. Very often, the objective is to model the electrical response of complex systems by means of a simple equivalent electrical circuit built using basic components such as a resistor and a capacitor.

In the same way the electrical resistance of a metallic wire is measured (Ohm`s law: R = V/I), the impedance of an electrochemical system can be determined by calculating the ratio the AC voltage applied and the AC current recorded. A typical EIS setup requires three-electrode cell: working electrode, counter electrode, and a reference electrode. In this setup, the working electrode represents the system under study, and the AC voltage is applied between the working electrode and the reference electrode. The AC current response is allowed to flow between the counter electrode and the working electrode.

3.4 Procedures

3.4.1 Paper-based electrodes

Paper-based electrodes were made by sputtering suitable metals on either filter or photography paper. Gold was used for the source/drain electrodes, as described in Figure 3.3, since it is well known that this metal reduces the contact resistance. The gate electrode was made with platinum, unless stated otherwise.

3.4.2 Construction of the channel for OECTs and chemiresistors

Figure 3.3 illustrates the fabrication steps of the devices. The fabrication process of the OECTs can be broken down into two major steps: patterning of the source/drain electrodes and deposition of the channel, and fabrication of the gate electrode. First, a photography paper was cut into a circle of 10 cm diameter. Next, parallel strips (0.5 mm wide) of an adhesive masking tape were deposited to the paper with 8 mm gap in between. Next, 100 nm thick layer of Au was sputtering on top of the paper. After sputtering, the adhesive strips were removed, leaving 0.5 mm gap which was the length of the channel. Finally, 0.8 cm x 1.5 cm gold pads were cut to make the source and drain electrodes.

Two methods were used for depositing the channel. Drawing of a PEDOT:PSS channel by dip-pen procedure. f) Protection of the gold pads by an adhesive tape leaving a window for the channel. g) A Standard tweezer (PELCO 5113 Carbofib Tip Tweezer) equipped with 0.5 x 0.6 mm (Width x Thickness) carbon fiber tip used to draw the channel.

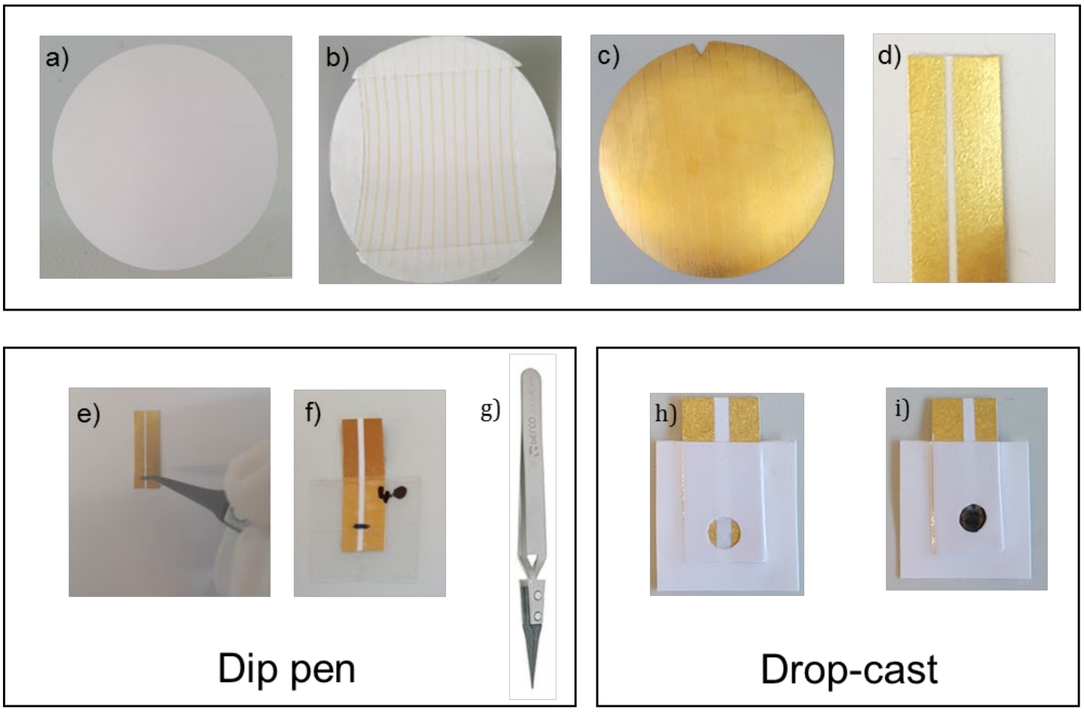

Figure 3.3. Fabrication steps of the source/drain electrodes, and deposition of the PEDOt:PSS by dip-pen and drop-cast methods.

3.4.3 Sample preparation for microscopic characterization

For TEM

Transmission electron microscope was employed to estimate the size and asses the dispersion of platinum and Prussian blue nanoparticles in PEDOT:PSS composites. After the preparation of the samples, a small volume (≈ 1 µL) was drop-casted on a standard TEM flat grid, and left dry at 60°C for 15 min. The samples were then analysed without further treatment.

For SEM

The thickness of the channels was measured from cross-section pictures acquired by FESEM. Prior to analysis, 20 nm thin layer of gold was deposited on the surface of the samples by sputtering. Next, successive thin layers of platinum were deposited to mark the testing area, and prevent any damage that may occur by the milling step. Finally, germanium ion beam was used to etch 5 µm x 5 µm area with 5 µm depth to expose the full thickness of the sample.

3.5 References

[1] GIL J. L.; VICENTE V. I.; GUAL G. A.; et al. Alkane dehydrogenation nanocatalyst and process for its preparation. 2022.

[2] *CH Instruments, Inc. Electrochemical Instrumentation.* https://www.chinstruments.com/ (accessed September,3, 2022).

4 Construction And Characterization Of Thick-Film PEDOT:PSS Channels On Paper

Summary

The present chapter deals with the fabrication and characterization of thick-film OECTs via drop cast. Thick-film PEDOT:PSS channels with different width-to-length ratios (W/L) were fabricated and their morphological and electrical properties were characterized. The objective is to understand how W/L affects key parameters such as Transconductance, response time, and ohmic behaviour.

4.1 Introduction

Analytical chemistry has recognized the benefits of paper since the early stages of its development[1]. For instance, litmus paper has been used by scientists for centuries to check the acidity of solutions, which is still considered today as the simplest method to test pH qualitatively[2]. Paper chromatography is another popular technique that illustrates the versatility of paper in analytical chemistry. In this method, mixtures are separated based on the partition of their compounds between two liquid phases, while moving through a paper support by capillarity[3]. Moreover, the technological advances in the fabrication processes of paper has facilitated the development of several types of paper, featuring tunable properties such as, pore sizes, roughness, thickness, and hydrophobicity[2, 4]. Additionally, the increasing need for simple point-of-care and disposable bio-chemical sensors has prompted scientists to search relentlessly for affordable materials that can be employed as the basis for their devices. Lateral flow systems are a very important area of research with a massive social impact[5]. More recently, paper-based microfluidic devices were pioneered by Whitesides et al[6]. Following this seminal work, the development of paper-based electrochemical cell has been profusely studied. For these reasons, unlike plastic, paper has proved to be an attractive material for building biosensors, owing to its biocompatibility, abundance in nature, low-cost, and specific strength[7, 8].

In the last two decades, paper has been integrated in several bio- and chemical sensing platforms, including electrochemical sensors[9, 10], immunoassays[11], chemiresistors[12], and organic electrochemical transistors (OECTs)[13, 14]. Although, several works have reported paper based OECTs, only a limited focus has been devoted to paper-based thick film OECTs for bio- and chemical sensing applications[15]. For instance, E. Bihar et al. have demonstrated a paper-based OECT as breathalyzer for the detection of alcohol in human breath. The sensor utilized a PEDOT:PSS channel and a gel electrolyte comprised of alcohol dehydrogenase enzyme and bovine gelatin[14].

A mentioned in Chapter 2, the transconductance is an essential parameter that reflects the ability of OECTs to amplify small voltage changes to high changes in current[16]. The transconductance can be enhanced in several ways: by (i) optimizing the channel and gate electrode geometry, (ii) increasing the charge mobility of the conducting polymer, (iii) increasing the number of charge carriers, and/or (iv) optimizing the ratio of channel and gate capacitances[17-21].

It is well known that thin film channels (thickness below 1 µm) demonstrate a number of characteristics such as, quick response time, high On/Off current ratio, and a transconductance that scales with the width-to-length ratio of the channel (W/L)[22-24]. The latter, in particular, has a significant impact on the response of OECTs, therefore, the W/L ratio can be utilized efficiently to enhance the performance of the devices[25].

Channels with large W/L ratios increase the surface area of the conducting polymer that is in contact with the electrolyte, hence, providing more paths for ions to diffuse through the channel. However, this increase in amplification may come at the expanse of much higher leakage current and response time[26]. For this reason, a compromise is usually required in order to make OECTs practical for real-life applications. In this work, we have built thick film OECTs on paper by drop cast using commercial PEDOT:PSS. The devices were fully characterized and their key parameters of the devices were determined. The OECTs constructed showed an excellent transconductance comparable to the state-of-the-art OECTs published in the literature, along with high current density, low gate currents, and high on/off current ratio.

4.2 Construction of the channels

The fabrication method employed in this chapter consists of assembling the patterned source/drain electrodes, the hydrophobic mask, and the PEDOT:PSS layer, As described in Figure 4.1. The gold electrodes were patterned on photography-quality paper as described in Section 3.3.2, whereas the length of all the channels (L) was set to 0.5 mm. Therefore, to construct channels with different W/L ratios, only the width (W) needed to be changed (Figure 4.1C). CO_2 laser cutting was used to cut the hydrophobic mask in five widths: 0.5 mm, 1 mm, 3 mm, 6 mm, and 10 mm, resulting in W/L ratios of 1, 2, 6, 12 and 20. The masks were cut in a way that ensures at least 1 mm overlap of the channel with the source/drain electrodes from both sides. Finally, to reduce the risk of having channels with large thickness differences, the volume of PEDOT:PSS drop-cast was adjusted systematically in a way that allows all channels to have the same

PEDOT:PSS volume-to-channel area ratio of 1 µL/mm^2. Figure 4.1D shows the final channels used in this study.

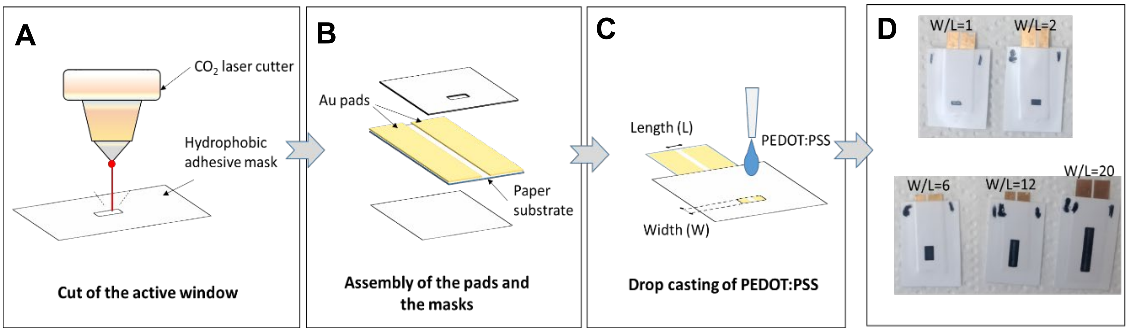

Figure 4.1. A) Laser cutting of the active window, B) assembly of the gold pads and the masks, C) drop casting of PEDOT:PSS on the active window, D) channels having different W/L ratios from left to right 1, 2, 6, 12, and 20.

4.3 Results and discussions

4.3.1 Ohmic response

The electrical conductivity of PEDOT:PSS films is known to increase with the thickness of the film[27]. This makes the performance of OECTs highly affected by the geometry of the devices. Therefore, it is important to check first the thicknesses of the PEDOT:PSS films prepared. Figure 4.2 displays FESEM pictures showing the cross-sections of four PEDOT:PSS channels prepared as described, and indicates that all channels have thicknesses well above 1 µm, with a minimum thickness of 2.62 ± 0.29 µm for the channel having W/L= 6, and a maximum thickness of 6.19 ± 1.13 µm having the highest W/L = 20. These values reflect the challenge of obtaining channels with consistent thickness using simple approaches such as drop casting or dip coating.

The ohmic response of the aforementioned channels was assessed in both dry and wet conditions. The I-V output curves of the channels were established by recording the current I_d, while sweeping the drain voltage V_d between -0.3 V and +0.3 V (0.05 V step) at room temperature in air, then in NaCl (0.1 M). Figure 4.3A and Figure 4.3B show the I-V output curves of the channels in dry and wet conditions, respectively. The results indicate that the current decreased slightly when the channels were tested in NaCl, compared to dry test. This decrease could be attributed to the swelling of the PEDOT:PSS[28]. When a PEDOT:PSS thin film is immersed in an aqueous solution, the diffusion of water inside the hollow structure of the film leads to an increase in its size, which affects the mobility of charge carriers[29]. Since thick films are denser, it can be hypothesised that this swelling effect is significantly reduced, and is limited only to a part of the PEDOT:PSS bulk channel.

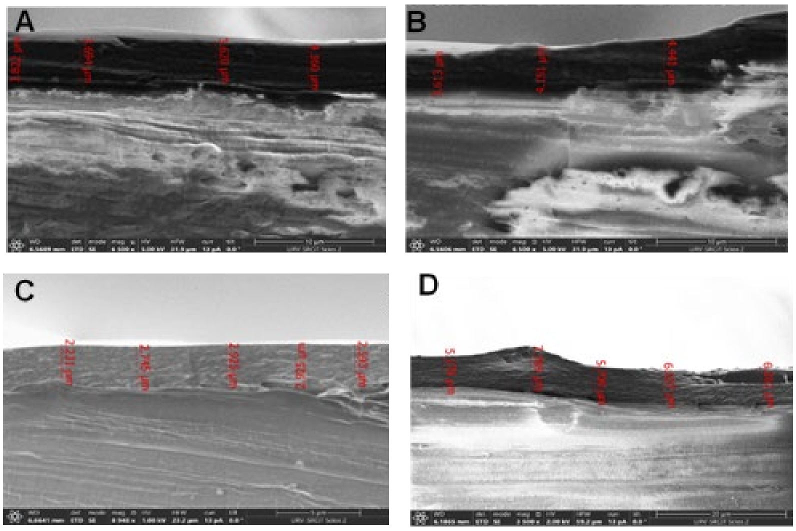

Figure 4.2. FESEM cross-sections of PEDOT:PSS channels that have a W/L of A) 1, B)2, C) 6, and D) 20.

On the other hand, regardless of the test conditions, all channels showed a linear relationship between I_d and V_d within the voltage range tested. This linearity suggests that the contact resistance (between PEDOT:PSS and source/drain electrodes) is ohmic, and most of the voltage applied drops across the PEDOT:PSS channel.

Furthermore, the resistance of the channels was also plotted versus W/L in order to check how the resistance changes with the W/L ratios. As can be seen from Figure 4.3C, the dynamic resistance of the channels (extracted from the I-V curves) is inversely proportional to the W/L ratio. For instance, the resistance decreased from 21.5 Ω for W/L=1, to 12.8 Ω for W/L=2, which represents 40 % drop in resistance. However, the drop in resistance was only 15.6 %, 13 %, and 30 %, when W/L was increased from 2 to 6, 6 to 12, and 12 to 20, respectively. This means that further increase in W/L beyond 20 is not expected to yield an important gain in conductivity for thick films. This behaviour can be explained by the increase of the contact resistance of the PEDOT:PSS film with its surface area. At some point, the increase of the contact resistance can offsets the gain in conductivity due to the bulk material. Additionally, it is known that the resistance of a conductor is proportional to it is length. This is very relevant for conducting polymers such as PEDOT:PSS which is considered at the macroscale as an amorphous material, making its conductivity highly dependent on the percolation of the PEDOT:PSS chains.

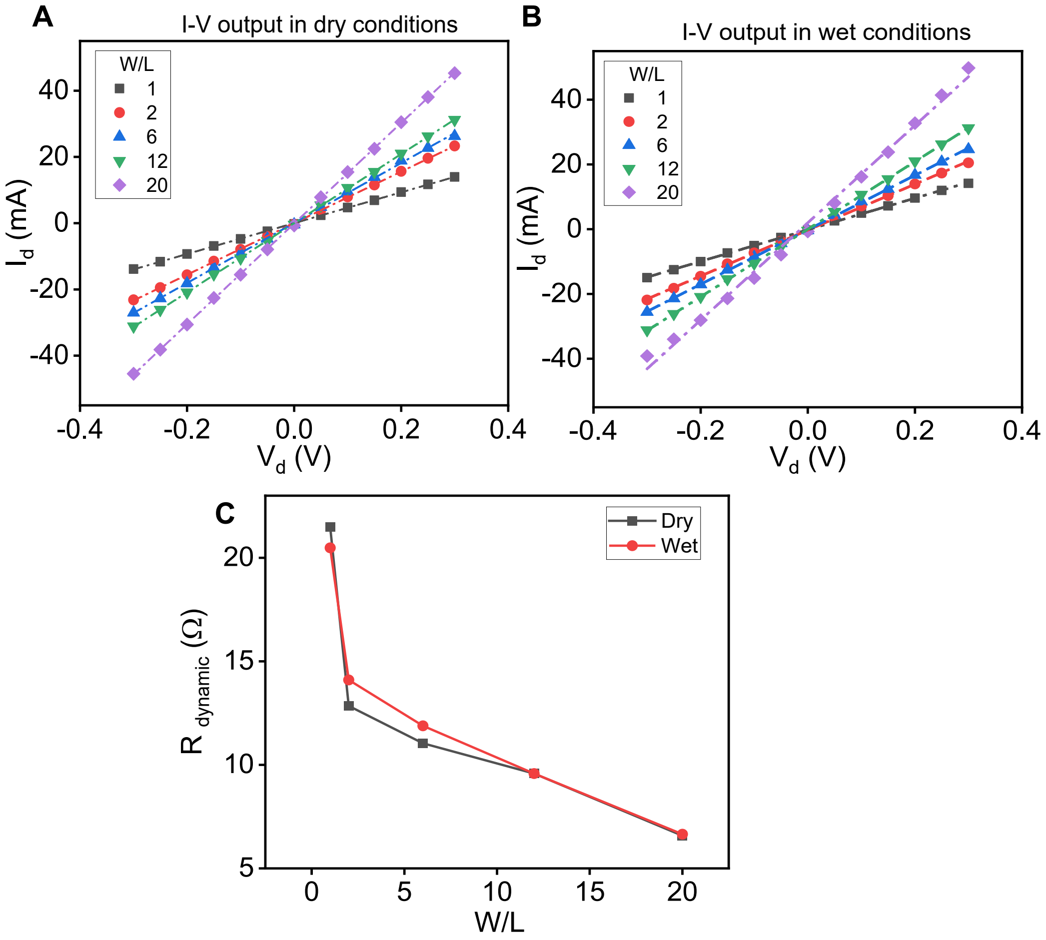

Figure 4.3. I-V output curve of four channels that have different W/L ratios (1, 2, 6, and 20) established, A) in air, and B) in NaCl (0.1 M). C) Dynamic resistance calculated from the I-V curves as function of the W/L ratio.

As demonstrated by Stocker et al., the conductivity of PEDOT:PSS can be viewed as the percolation between two regions. The first region is PEDOT:PSS rich and exhibits high conductivity (2.3 $\Omega.cm^{-2}$). On the other hand, the second region is PSS rich and shows very low conductivity (10^{-3} $\Omega.cm^{-2}$)[30]. Similar behaviour was also observed when the conductivity of different PEDOT:PSS films with increasing thickness was measured[31]. The conductivity increased by 50 % when the thickness was changed from 50 nm to 110 nm, while it increased by only 10 % when the thickness was further increased to 500 nm. Therefore, the performance of the channels can be limited by the W/L.

4.3.2 Post and Pre-treatment of PEDOT:PSS

We have seen earlier that the resistance of thick films created by drop cast does not scale with W/L. Therefore, increasing this parameter may not be the best approach to enhance the conductivity of the channel. Alternatively, the conductivity of PEDOT:PSS films has proven to be altered when the film is treated with different solvents[32]. To check the effect of solvent treatment on the resistance and reproducibility, we treated PEDOT:PSS channels that has low W/L (W/L=2) with different solvents using two methods : pre-treatment and post-treatment. In the former method, the solvent is mixed with the PEDOT:PSS commercial solution prior to drop-casting and drying. In contrast, the post-treatment consists of treating a dried PEDOT:PSS channel by drop-casting 1 µL of the solvent on top of the channel, followed by an additional step of drying at 100 ˚C for 5 min and rinsing with deionized water.

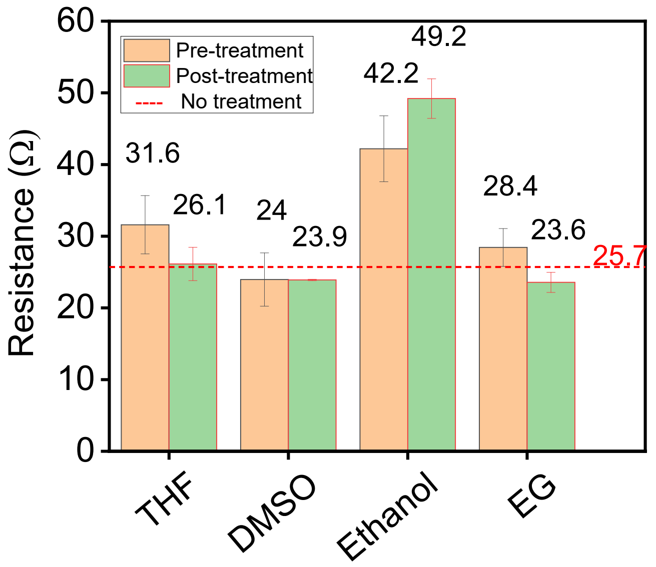

Figure 4.4. Resistance of PEDOT:PSS channels pre-and post-treated with different solvents.

Figure 4.4 shows the resistance of PEDOT:PSS channels (W/L=2) pre- and post-treated with four solvents that have an increasing polarity: tetrahydrofuran (THF), DMSO, ethanol, and ethylene glycol (EG). The results show that, the post-treatment of PEDOT:PSS with EG decreased the resistance of the channel by 8.1 %, while the pre-treatment yielded an increase of 10 %. This is consistent with the literature, wherein EG was reported to enhance the conductivity of PEDOT:PSS thin films[33]. Lin et al. have demonstrated that EG acts on PEDOT:PSS by increasing its charge carriers density, while the charge mobility remains invariable[34]. The worst results were obtained using ethanol where the resistance increased by 64.2 % and 91.4 % for pre- and post-treatment, respectively. Furthermore, DMSO treatment did not have a significant impact on the resistance of the channel, although, the resistance of the post-treated channels demonstrated an excellent reproducibility with a standard deviation of 0.1 Ω (N=3). Therefore, the solvents tested affected the resistance of the channels differently. While DMSO and EG showed the best results, ethanol and THF led to an increase in the resistance regardless of the treatment. This makes the DMSO post-treatment the best approach to improve reproducibility of the devices without sacrificing their electrical properties.

4.3.3 On/Off current ratio

The On/Off current ratio is another important characteristic of OECTs that is affected by the geometry of the devices. The ratio is determined by measuring the drain current at a given V_d without applying any gate voltage (on-state), and with an applied gate voltage (off-state). Figure 4.5 displays the On/Off current ratio as function of the W/L ratio for the same OECTs tested earlier, calculated at V_d = -0.3 V. The maximum gate voltage was set to 0.7 V to avoid damaging the devices. The graphs show that the channel with the lowest width-to-length ratio (W/L =1) demonstrated the highest On/Off current ratio 7.4×10^3. The ratio decreased with the increasing W/L, to reach 1.7×10^3 for W/L = 20.

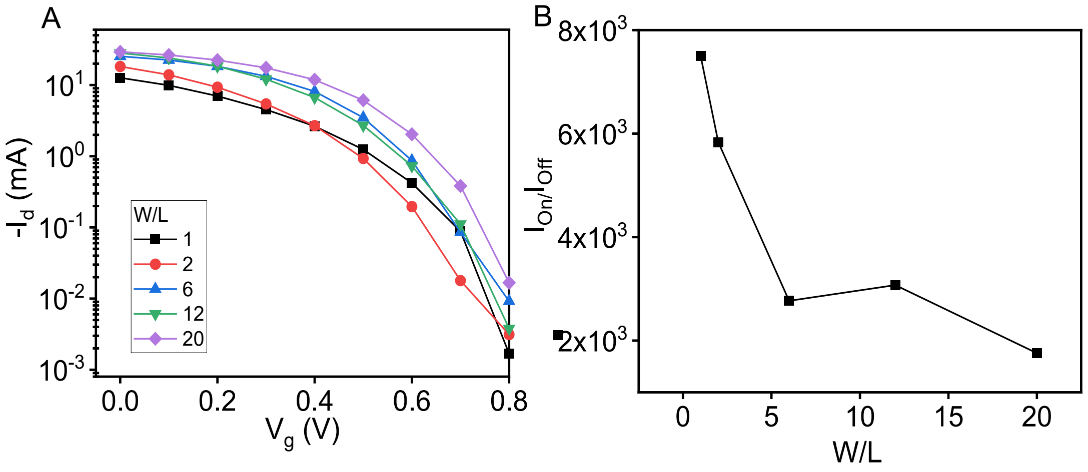

Figure 4.5. A) Transfer curves I_d-V_g of the OECTs in logarithmic scale established at V_d = -0.3 V, and B) On/Off current ratios plot versus W/L calculated from the transfer curves.

4.3.4 Time constant and measurement of the gate current I_g

The response time of the devices was also evaluated to check how it is affected by the device geometry. Figure 4.6A displays the drain current I_d of the OECTs at V_d = -0.3 V while V_g was increased from 0 V to 0.1 V. As expected, the response of the OECTs to a gate voltage step exhibit an exponential profile that reflects the transient response of the devices, and can be assimilated to the charging of a capacitor[35]. For this reason, the response was then fitted to an exponential function, which allows the determination of the time constant of each device[36]. The time constant corresponds to the time required by the device to reach 63 % of the total response. It is commonly used to compare and benchmark the response times of different devices. The results show that all devices reached have a response below 1 second. Small time constants are essential especially for transistors that are employed for designing logic circuits. However, in the context of (bio)chemical sensing, other qualities are more crucial than fast switching such as stability, reproducibility, and sensitivity. Compared to thick films, thin film OECTs with thickness below 1 µm enable cations to enter and exit the channel without diffusing and drifting too far from the bulk electrolyte. Although this is detrimental to the transconductance, thin-film devices exhibit fast switching and response times that vary between microseconds and milliseconds[37]. For instance, Khodagholy et al. have reported an OECT array that demonstrated a response time of 100 µs[38]. However, this remarkable result was obtained with an array of 64 OETCs, where each transistor was subjected to V_d = -0.5 V and V_g = 0.4 V, and with channels made of PEDOT:PSS that is 6 µm long, 15 µm wide, and 80 nm thick.

Apart from the time constant, the gate current (I_g) that flows through the Ag/AgCl gate electrode was also measured during the sweep of the gate voltage. Figure 4.6B shows I_g-V_g plots for channels with different W/L, recorded while sweeping the gate voltage from 0 V to 0.7 V. The graph shows that the absolute value of I_g increased with V_g, and the values of I_g after stabilization remained below 10 µA for all channels. Furthermore, Figure 4.6C displays the time trace of I_g, and gives much more information about how I_g evolves. It can be seen that each V_g step induces an abrupt increase in I_g, giving rise to peak currents. As we have previously observed for I_d, the profile of I_g is similar to a charging and discharging of a capacitor, after which I_g stabilizes.

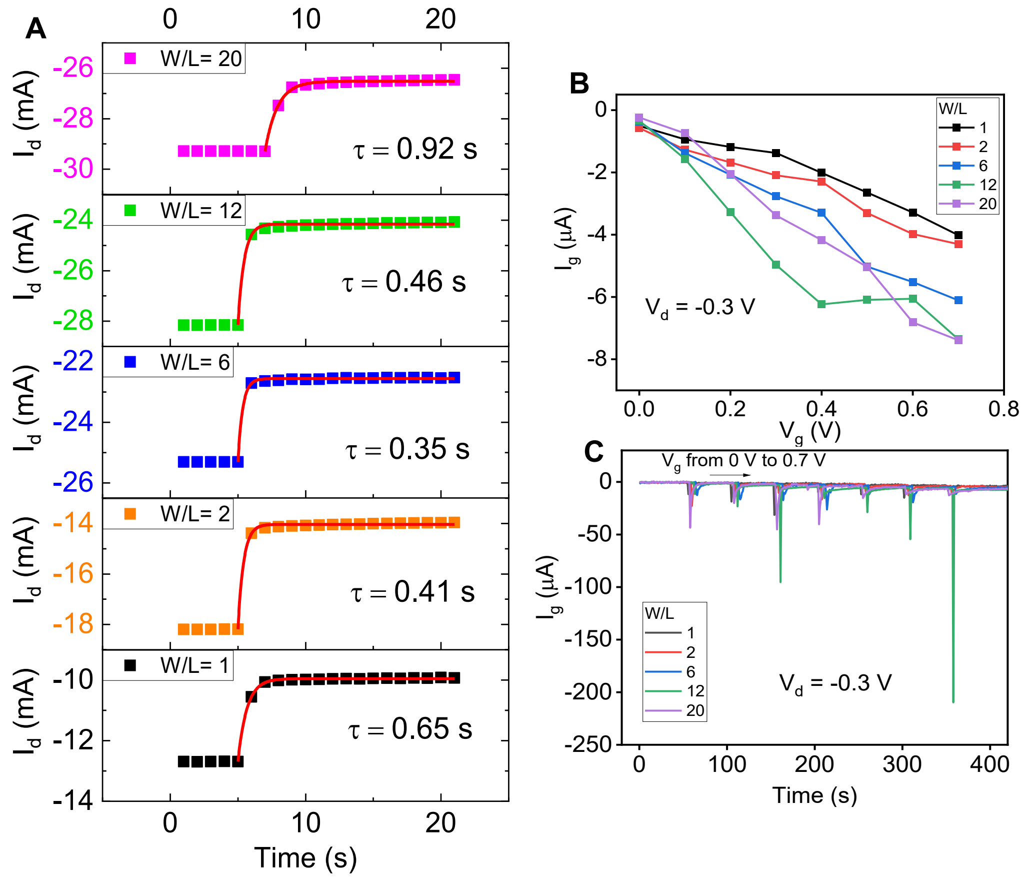

Figure 4.6. A) Time trace of I_d showing the response time of OECTs with different W/L channels, 1, 2, 6, 12, and 20, at V_d = -0.3 V while V_g was stepped from 0 V to 0.1 V. The red line represents the fitting of experimental data to an exponential function y = y0 + A*exp(-t/τ), where τ is the time constant of the device. B) Time plot of the gate current I_g recorded for the same OECTs at V_d =-0.3 V, while the gate voltage V_g is swept from 0 V to 0.7 V, and C) corresponding curves showing I_g as function of V_g.

It is worth noting that all OECTs showed an I_g significantly lower (few µA) compared to I_d (few mA). For instance, at the same gate voltage V_g= 0.4 V, the OECT with W/L = 1 showed an I_g and I_d of -2.01 µA and 1.96 mA, respectively. However, the magnitude of I_g peaks can reach higher values, as in the case of W/L= 12, where I_g exceeded 200 µA for a fraction of a second. The small magnitude of the gate current observed upon applying a gate voltage suggests that this current is of capacitive origin carried by the ions in the electrolyte. The magnitude of gate currents is highly important, particularly, when different OECTs share the same gate electrode such as in multiplexed systems. The superposition of the gate currents may lead to an increase in the magnitude of I_g, which may affect the stability of the device. As indicated in several works, I_g depends significantly on the nature of the gate electrode, and when its magnitude is large enough, it can affect the oxidation state of the channel[39, 40]. Therefore, designing thick film OECTs with very low I_g is beneficial for multiplexed systems where it is essential to minimize the sources instability.

4.3.5 Transconductance

The transconductance of the OECTs was also determined by constructing the transfer curves at different V_d. To avoid operating with excessive values of I_d, the transfer curves were established by fixing V_d between -0.3 V and -50 mV, while sweeping V_g from 0 V to 0.7 V in NaCl (0.1 M), using Ag/AgCl electrode as a gate electrode. Three devices for each OECT with a given W/L was tested. The time trace of I_d (shown in Figure S4.1 Supporting Information) displays step-like curves for all OECT, which shows clearly the decrease of I_d upon applying an increasing V_g, indicating an effective dedoping of the PEDOT:PSS films. Moreover, when the transfer curves I_d-V_g were normalized and plotted on the same graph (Figure S4.2), all the curves corresponding to W/L= 1 and 2 devices collapsed to one unique curve, while for OECTs with W/L= 6, 12 and 20 the curves were relatively dispersed. This behaviour indicates that W/L=1 and 2 OECTs are much more stable and demonstrate reproducible gating performance.

Furthermore, Figure 4.7 displays the plot of the average transconductance (N=3) versus the V_g of the OECTs. The graph shows that OECTs with low W/L exhibit a maximum transconductance (g_m) at slightly lower V_g, compared to devices with high W/L. For instance, devices with W/L=1, 2, and 6 demonstrated a g_m of 32.9 ± 3.8 mS, 43.5 ± 4.8 mS, and 38.9 ± 4.4 mS, respectively, at 0.2 V. In contrast, g_m for the devices W/L=12 and 20 was 67.0 ± 5.8 mS and 67.9 ± 6.1 mS, respectively, at 0.3 V. In addition, the effect that has W/L on g_m of the OECTs is clearly represented in Figure 4.7F, and it shows a positive correlation between g_m and W/L within a short interval. However, as discussed for the resistance in section 4.3.1, an increase of W/L from 12 to 20 had a negligible effect on g_m.

The maximum transconductance of the OECTs tested were 30.56 mS, 22.06 mS, 39.54 mS, and 64.47 mS for OECTs with W/L of 1, 2, 6, and 20, respectively. The drain and gate voltages for which these values were obtained were -0.3 V and 0.2 V/0.3 V respectively.

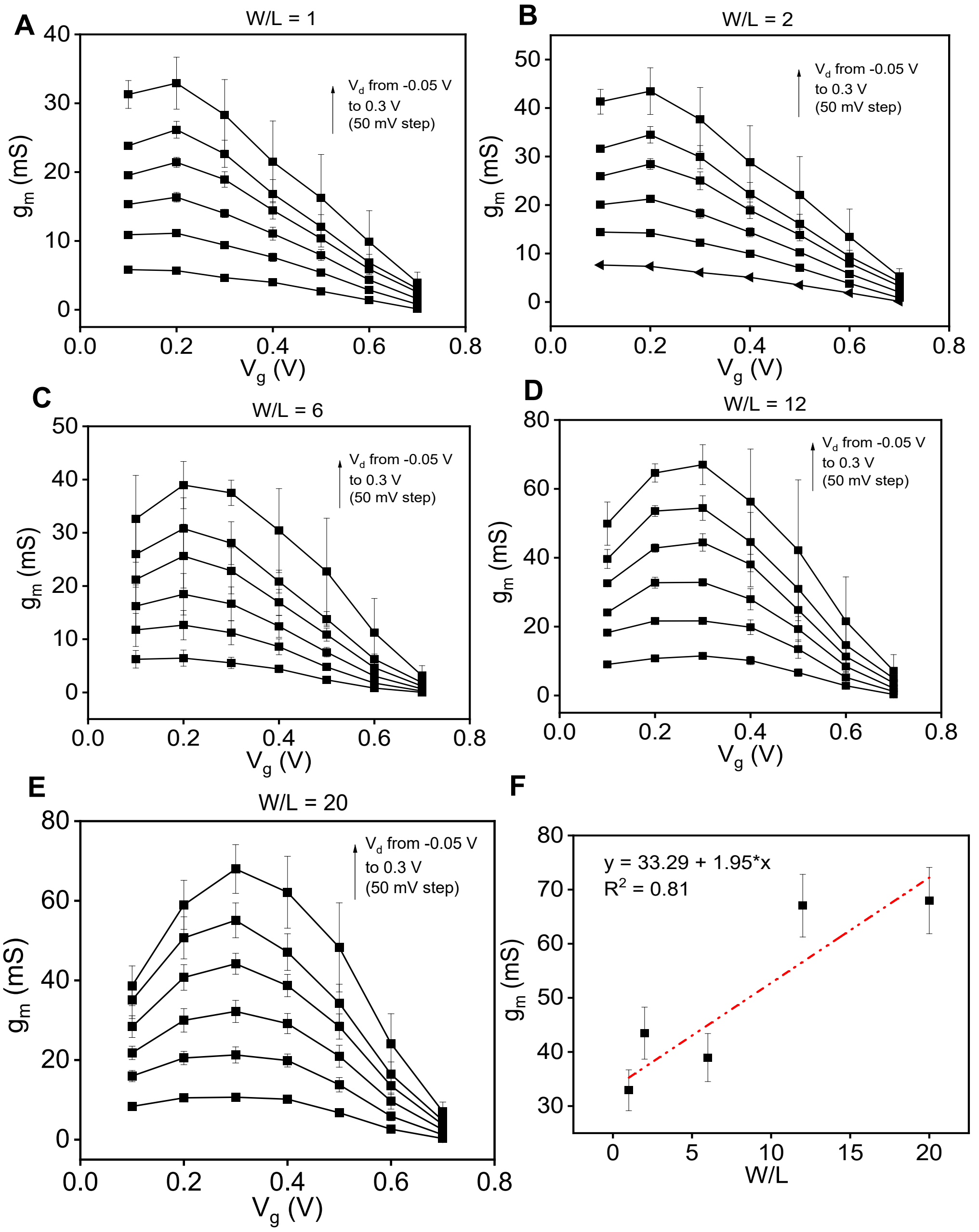

Figure 4.7. Transconductance-V_g plots for OECTs with channels that have W/L ratios A) 1, B) 2, C) 6, D) 12, and E) 20. F) Maximum transconductance as function of W/L ratios at V_d =-0.3 V. (N=3)

4.4 Conclusions

In the present chapter, we report on the construction and characterized thick film OECTs on a paper substrate. The channels were constructed by drop casting the conductive polymer PEDOT:PSS directly on hydrophobic masks that have different width-to-length ratios. Unlike other deposition methods (i.e. spin coating), drop casting reduces the volume of the conducting polymer used down to few microliters, and enables the fabrication of thick film PEDOT:PSS channels with a thickness well above 1 μm. The thick film OECTs tested exhibited an excellent transconductance that scales with the W/L ratio, good On/Off current ratios, low gate current leakage, along with an excellent stability in water and air. This work contributes to the efforts that aim at integrating paper in OECTs for building affordable, easy-to-use, and highly sensitive platforms for portable and disposable sensors.

4.5 Supporting information

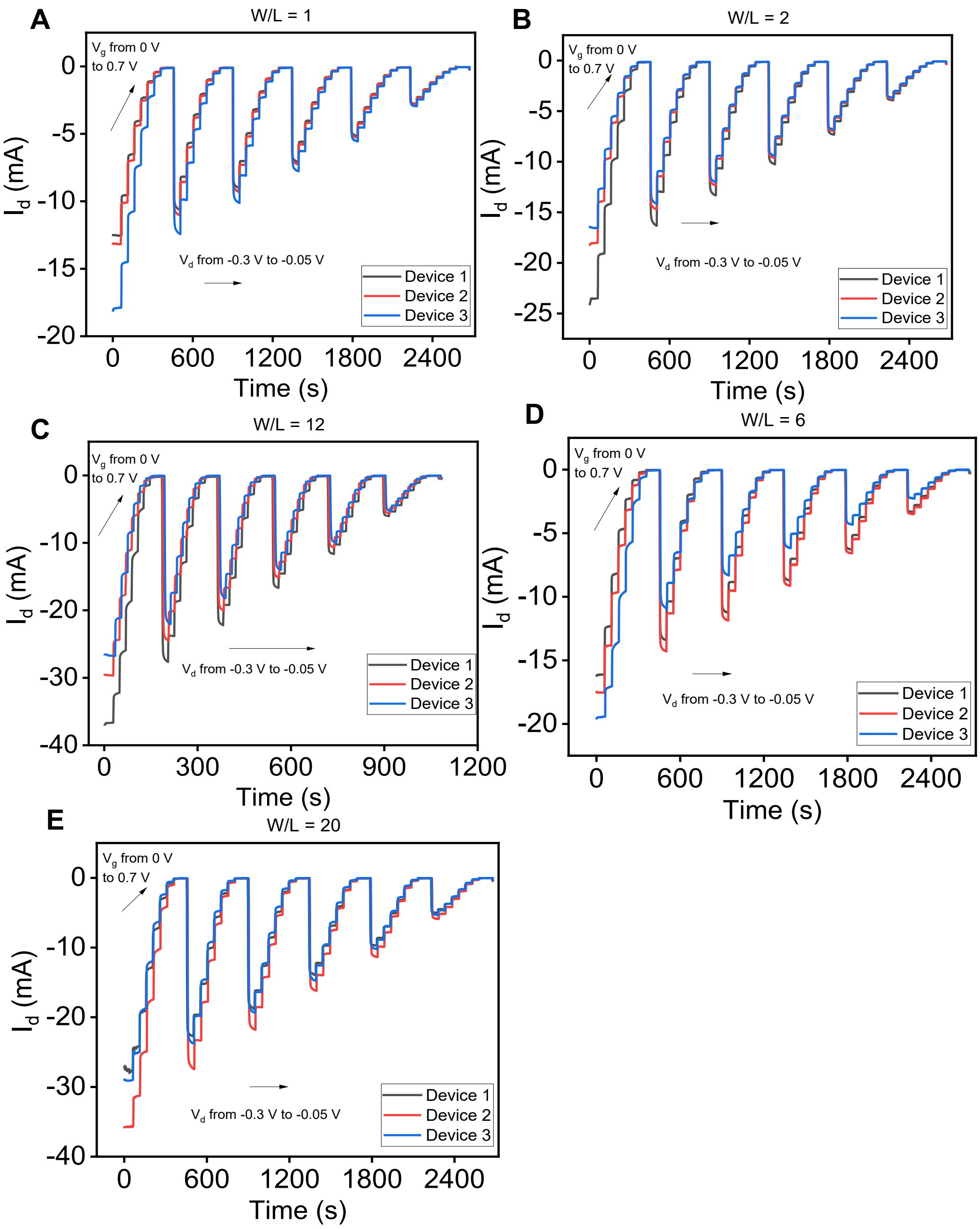

Figure S4.1. Time trace of the transfer curves showing the change of I_d at different V_d and V_g for channels with W/L of A) 1, B) 2, C) 6, D) 12, and E) 20. To allow the devices recover, the time between each V_g step was set to 50 s.

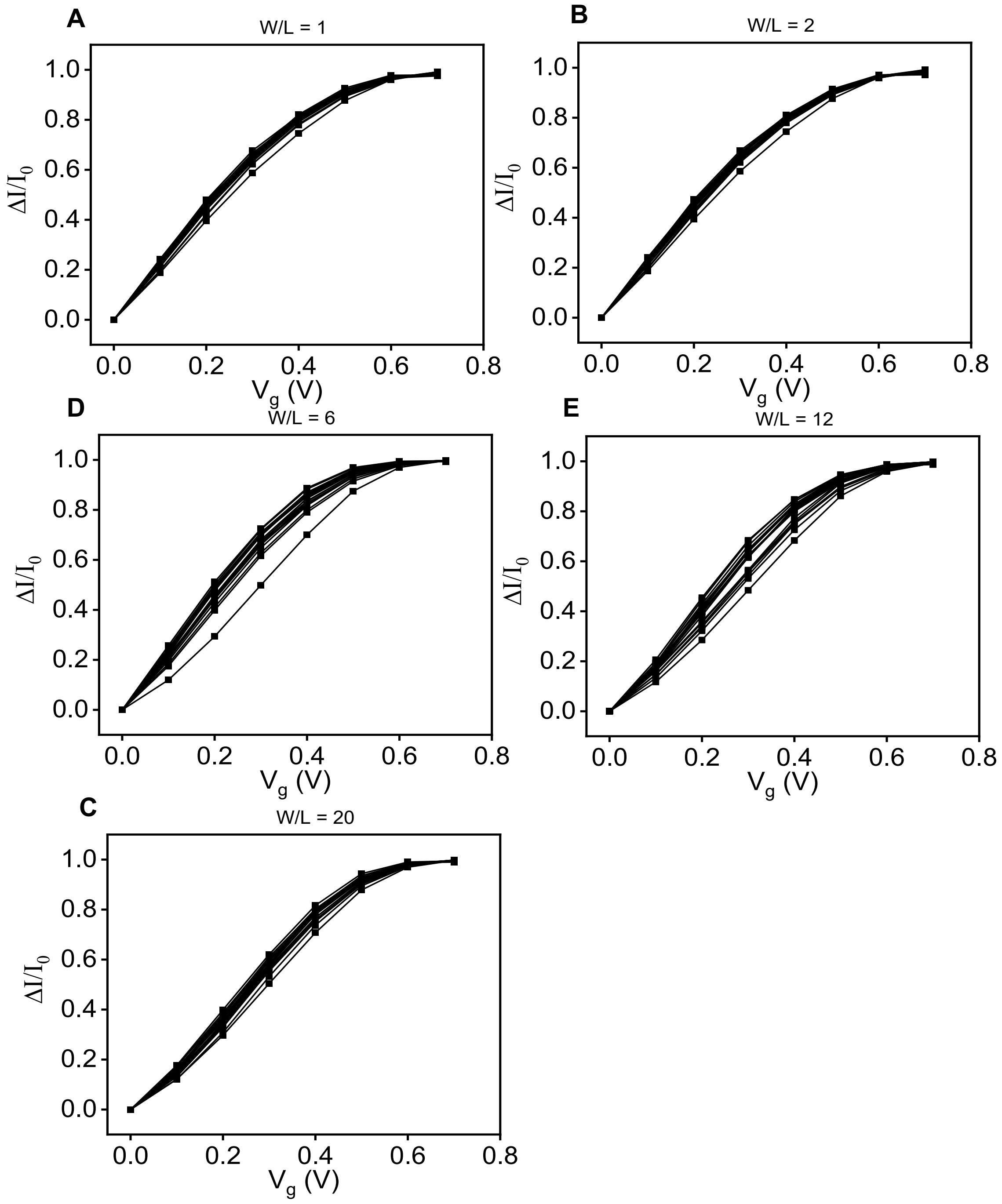

Figure S4.2. Normalized transfer curves at different V_d and V_g, for channels having W/L ratio of A) 1, B) 2, C) 6, D) 12, and E) 20.

4.6 References

[1] Rice, E., *J Ind Eng Chem*, **2002**, 4, 229-229.

[2] Salentijn, G. I.; Grajewski, M.; Verpoorte, E., *Anal Chem*, **2018**, 90, 13815-13825.

[3] Clegg, D. L., *Anal Chem*, **2002**, 22, 48-59.

[4] Sahin, H. T.; Arslan, M. B., *Int J Mol Sci*, **2008**, 9, 78-88.

[5] Koczula, K. M.; Gallotta, A., *Essays Biochem*, **2016**, 60, 111-120.

[6] Glavan, A. C.; Martinez, R. V.; Maxwell, E. J.; et al., *Lab Chip*, **2013**, 13, 2922-2930.

[7] Singh, A. T.; Lantigua, D.; Meka, A.; et al., *Sensors (Basel)*, **2018**, 18, 2838.

[8] Lee, V. B. C.; Mohd-Naim, N. F.; Tamiya, E.; et al., *Anal Sci*, **2018**, 34, 7-18.

[9] Bouhoun, M. L.; Blondeau, P.; Louafi, Y.; et al., *Chemosensors*, **2021**, 9, 96.

[10] Novell, M.; Guinovart, T.; Blondeau, P.; et al., *Lab Chip*, **2014**, 14, 1308-1314.

[11] Hristov, D. R.; Rodriguez-Quijada, C.; Gomez-Marquez, J.; et al., *Sensors (Basel)*, **2019**, 19, 554.

[12] Pozuelo, M.; Blondeau, P.; Novell, M.; et al., *Biosens Bioelectron*, **2013**, 49, 462–465.

[13] Nair, R. R., *Flex Print Electron*, **2020**, 5, 045004.

[14] Bihar, E.; Deng, Y.; Miyake, T.; et al., *Sci Rep*, **2016**, 6, 27582.

[15] Zschieschang, U.; Klauk, H., *J Mater Chem C*, **2019**, 7, 5522-5533.

[16] Khodagholy, D.; Rivnay, J.; Sessolo, M.; et al., *Nat Commun*, **2013**, 4, 2133.

[17] Polyravas, A. G.; Schaefer, N.; Curto, V. F.; et al., *Appl Phys Lett*, **2020**, 117, 073302.

[18] Paudel, P. R.; Kaphle, V.; Dahal, D.; et al., *Adv Funct Mater*, **2020**, 31, 2004939.

[19] Matsuhisa, N.; Jiang, Y.; Liu, Z.; et al., *Adv Electron Mater*, **2019**, 5, 1900347.

[20] Wu, X.; Surendran, A.; Ko, J.; et al., *Adv Mater*, **2019**, 31, e1805544.

[21] Rivnay, J.; Leleux, P.; Sessolo, M.; et al., *Adv Mater*, **2013**, 25, 7010-70104.

[22] Nissa, J.; Janson, P.; Simon, D. T.; et al., *Appl Phys Lett*, **2021**, 118, 053301.

[23] Berggren, M.; Malliaras, G. G., *Science*, **2019**, 364, 233-234.

[24] Proctor, C. M.; Rivnay, J.; Malliaras, G. G., *J Polym Sci, Part B: Polym Phys*, **2016**, 54, 1433-1436.

[25] Lill, A. T.; Cao, D. X.; Schrock, M.; et al., *Adv Mater*, **2020**, 32, e1908120.

[26] Zabihipour, M.; Lassnig, R.; Strandberg, J.; et al., *npj Flex Electron*, **2020**, 4, 15.

[27] Friedel, B.; Keivanidis, P. E.; Brenner, T. J. K.; et al., *Macromolecules*, **2009**, 42, 6741-6747.

[28] Biessmann, L.; Kreuzer, L. P.; Widmann, T.; et al., *ACS Appl Mater Interfaces*, **2018**, 10, 9865-9872.

[29] Sarkar, B.; Jaiswal, M.; Satapathy, D. K., *J Phys Condens Matter*, **2018**, 30, 225101.

[30] Stöcker, T.; Köhler, A.; Moos, R., *J Polym Sci, Part B: Polym Phys*, **2012**, 50, 976-983.

[31] Kumar, P.; Yi, Z.; Zhang, S.; et al., *Appl Phys Lett*, **2015**, 107, 053303.

[32] Yan, H.; Okuzaki, H., *Synth Met*, **2009**, 159, 2225-2228.

[33] Iyer, A.; Hack, J.; Angel Trujillo, D.; et al., *Appl Sci*, **2018**, 8, 2052.

[34] Lin, Y. J.; Ni, W. S.; Lee, J. Y., *J Appl Phys*, **2015**, 117, 215501.

[35] Paudel, P. R.; Tropp, J.; Kaphle, V.; et al., *J Mater Chem C*, **2021**, 9, 9761-9790.

[36] Faria, G. C.; Duong, D. T.; Salleo, A., *Org Electron*, **2017**, 45, 215-221.

[37] Friedlein, J. T.; McLeod, R. R.; Rivnay, J., *Org Electron*, **2018**, 63, 398-414.

[38] Khodagholy, D.; Gurfinkel, M.; Stavrinidou, E.; et al., *Appl Phys Lett*, **2011**, 99, 2011-2014.

[39] Tarabella, G.; Santato, C.; Yang, S. Y.; et al., *Appl Phys Lett*, **2010**, 97, 123304.

[40] Koutsouras, D. A.; Torricelli, F.; Gkoupidenis, P.; et al., *Adv Mater Technol*, **2021**, 6, 2100732.

5 Thick-film OECTs For The Detection Of Hydrogen Peroxide And Glucose

Summary

The previous chapter focused on the characterization of thick film OECTs featuring different W/L ratios, constructed via drop cast method. The devices demonstrated promising performance in terms of transconductance, ON/OFF ratio, and response time even for low W/L values. In this chapter, dip pen, an alternative method that allows the direct deposition of channels with low W/L and controlled thickness, was used to construct the OECTs. The OECTs were microscopically, electrically, and electrochemically characterized, then employed for the detection of hydrogen peroxide and glucose as a model. The results were published as a journal article: A. Ait Yazza, P. Blondeau, and Francisco J. Andrade, "Simple Approach for Building High Transconductance Paper-Based Organic Electrochemical Transistor (OECT) for Chemical Sensing" ACS Applied Electronic Materials. 2021, 3, 1886−1895.

5.1 Introduction

As stressed out in several works, the transconductance is a critical parameter to keep in mind for designing sensors with enhanced performance, because it is related to the amplification of the signal and, ultimately, the sensitivity of the technique[1]. While significant work is currently focused on increasing the transconductance through the modification of channel materials, another straightforward way to optimize g_m is through the obtimization of the thickness of the channel. Unlike field-effect transistors, which show a 2D surface-limited capacitance, the hydrophilic and porous PEDOT:PSS channel creates a volumetric, 3D capacitance[2] that allows OECTs to display transconductances significantly higher than other transistors[3]. It is well known that the transconductance is directly related to the channel dimensions.

$$g_m \propto \frac{W.d}{L} \qquad \text{Equation 5.1}$$

Where W (width), L (length) and d (thickness) are the channel characteristics as shown in Figure 5.1. Therefore, there is a direct way to enhance the transconductance by increasing the channel thickness[4]. Nevertheless the response time (τ) is also affected by the channel thickness[5]:

$$\boldsymbol{\tau} \propto d\sqrt{WL} \qquad \text{Equation 5.2}$$

As a result, optimization of the OECTs has been traditionally characterized by a trade-off between transconductance and response time. For this reason, thickness has been usually kept below 1 µm. With channels ranging from tens to several hundreds of nanometers, transconductances in the order of 5 mS and response times in the millisecond range have been reported[3]. Thus, transconductances are still significantly higher than in other transistors, while response times are low-enough for many applications. Rivnay et al., for example, successfully recorded human brain activity using two PEDOT:PSS OECTs with channel thicknesses of 230 nm and 870 nm[4]. Since the vast range of applications are based on these types of devices, fundamental studies of the OECTs have been traditionally kept within this range. There are significant efforts to improve the response time by minimizing the effects of diffusion, such as the modifications of the channel composition[6], internal ion reservoirs[7], ionic liquids[8], etc. In all cases, channel thickness has been kept under the micrometer range, and applications of OECTs with channel thickness above 1 µm are scarce[9].

In chemical and biochemical sensing, the response time is often controlled by the kinetics linked to the recognition events. In these situations, the optimization is mostly based on maximizing the transconductance -to enhance the sensitivity-. Therefore, it is worth questioning whether using thicker channels –beyond the traditional nanometer range limit- might be a valid approach to maximize the analytical response. The answer is not straightforward, since phenomena linked to ion migration, film hydration and swelling, etc, may be negatively affecting the performance of the system.

In this work, we explore the characteristics of a thick-film OECT when applied to the determination of hydrogen peroxide, a molecule that is present in a plethora of biochemical sensing schemes. In the last few years, our group studied the use of a Pt electrode coated with a layer of Nafion for the potentiometric determination of H_2O_2 and the construction of biosensors[10]. OECTs for the detection of hydrogen peroxide and the generation of glucose sensors using Pt and composite materials for the gate have also been reported[11-14]. Thus, this work will show the advantages of the thick-film platforms, such as the simplicity of construction of paper-based devices, to generate chemical sensors and biosensors. Analytical characterization of the thick-film sensor for hydrogen peroxide and proof of principle of a glucose sensor are presented.

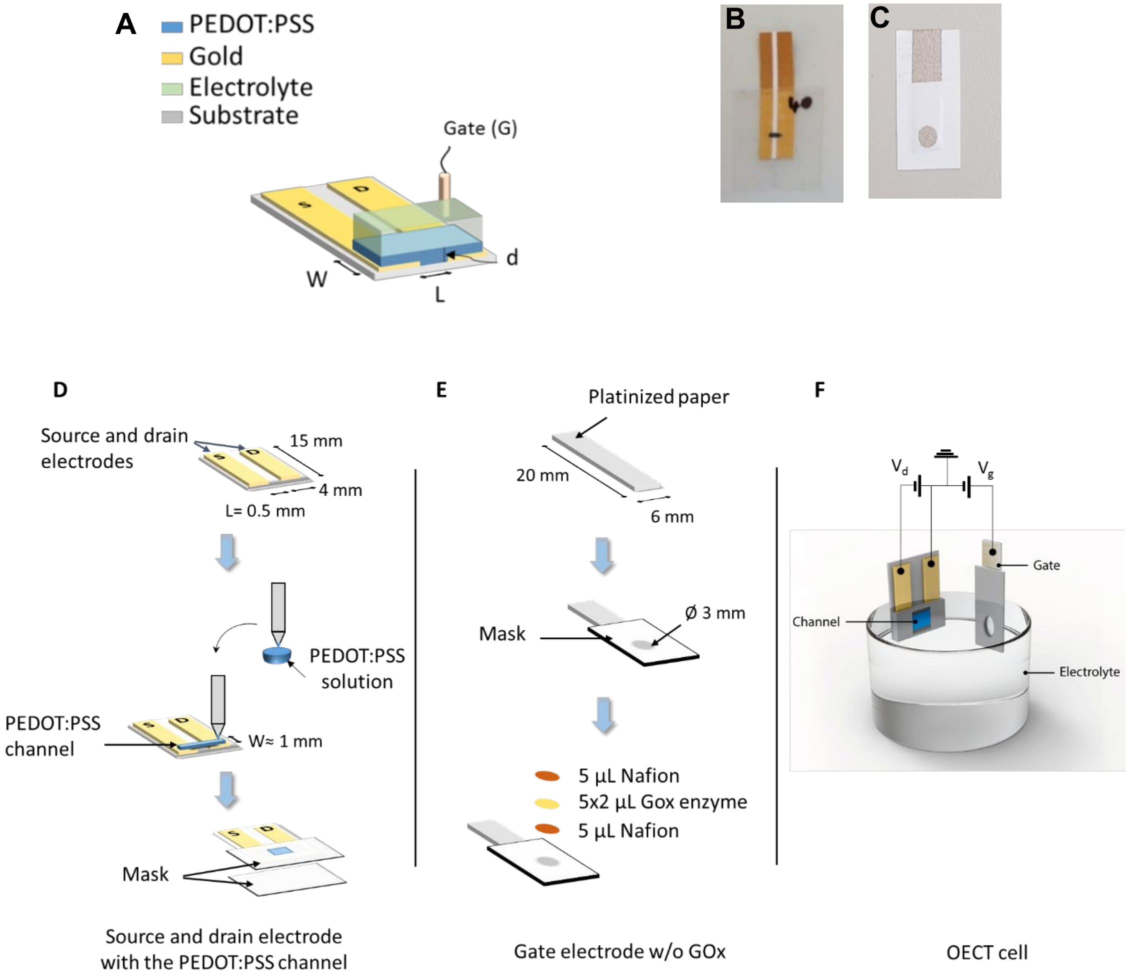

Figure 5.1. A) Schematic of an OECT, where W: width, L: length and d: thickness of the channel. B) Source/drain electrodes and PEDOT:PSS channel. C) Platinum gate electrode. D) Drawing of the PEDOT:PSS channel. E) Construction of the paltinum gate electrode. F) Schematic of the measurement cell.

5.2 Results and Discussion

5.2.1 Electrical characterization of the channel

Three types of channels were prepared by drop-casting of 1, 3, and 6 layers of the conducting polymer PEDOT:PSS. Figure 5.2A and Figure 5.2B display the time trace and the I_d-V_d characteristic of the aforementioned channels under dry conditions, that is, in the absence of the electrolyte solution. The graphs indicate that the device demonstrates a stable response which increases with the increase of the voltage applied. Furthermore, the plot of I_d-V_d shows a linear relationship within the range tested (-0.2 V to 0.2 V), hence, an ohmic behaviour. The range of V_d applied was limited because of the high conductivity of the channels, which results in currents that exceed the specifications of the measuring instrument (> 21 mA). Table 5.1 summarizes the values of the dynamic resistance extracted from the slope of the I-V output. It is worth noting that with only one layer, the system already shows a low dynamic resistance (or high conductance) in the order of 22 Ω. The dynamic resistance drops by 50 % when more layers are superimposed, as observed for 6 layers, where the resistance reaches a value of 11.0 Ω.

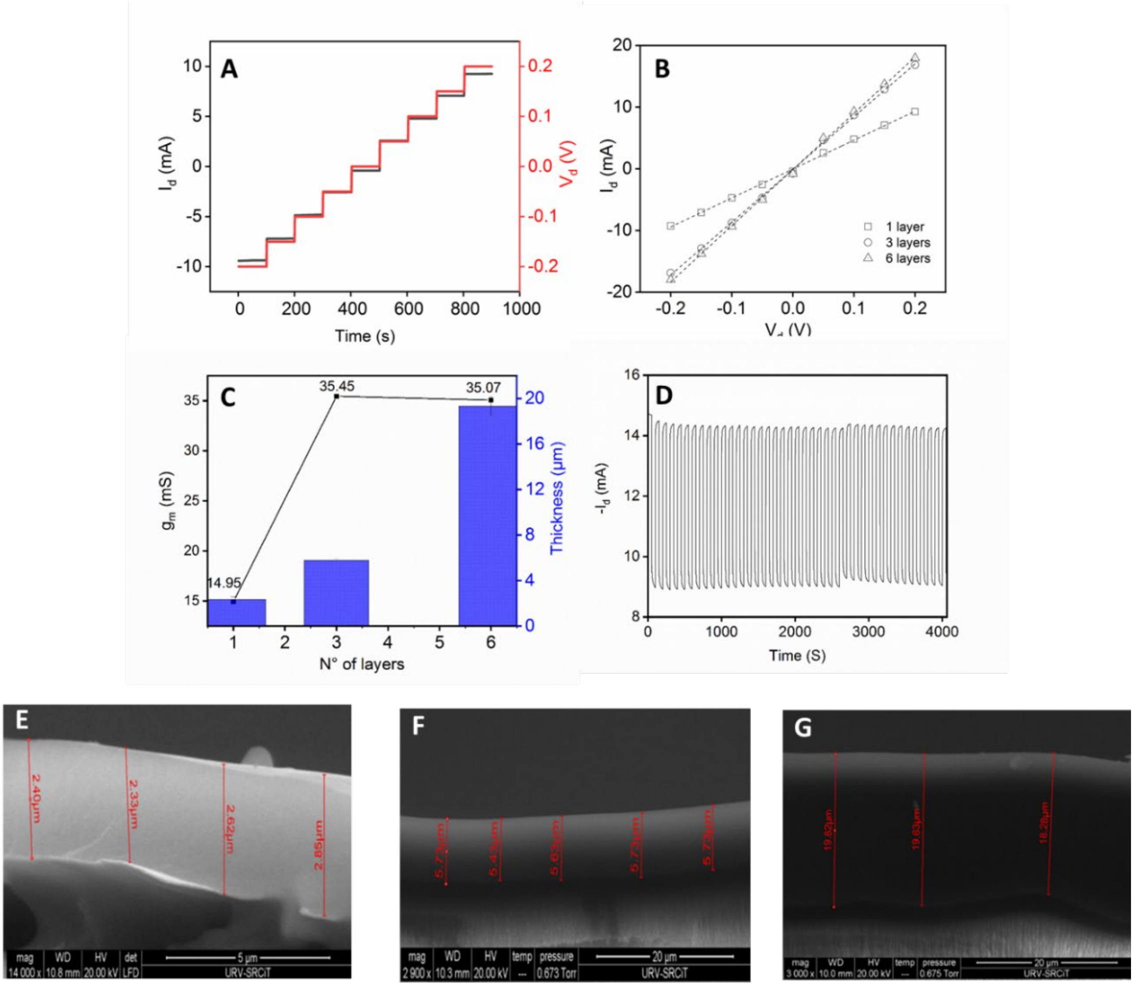

Figure 5.2. A) Time plot of Id for a channel with one PEDOT:PSS layer, as Vd is changes from -0.2 V to 0.2 V. B) $I_d - V_d$ characteristics of three channels with 1, 3 and 6 layers of PEDOT:PSS tested in dry conditions. C) Transconductance and thickness plots against the number of PEDOT:PSS layers. D) Current profile upon application of a square wave voltage at 0.05 Hz (50% duty cycle) during 40 cycles (-0.1 and -0.2 V) for a channel made of 3 layers. ESEM cross-sections of three PEDOT: PSS channels having E) 1 layer, F) 3 layers, and G) 6 layers.

The overall value of the resistance measured can be divided into two components: the bulk resistance of the CP, and the contact resistance ($R_{total} = R_{channel} + R_{contacts}$)[15]. As, discussed previously, gold was utilized to pattern the source/drain electrodes because it minimizes the contact resistance with the CP. Additionally, another form of resistance may arise from the superposition of multiple PEDOT:PSS layers, as reported by Pesavento et al. for pentacene-based thin-film transistors[16].

Table 5.1. Dynamic and static resistance of three channel with different number of PEDOT:PSS layers 1, 3 and 6. The dynamic resistance was calculated from the corresponding I_d- V_d curves by taking the inverse of the slope, while the static resistance was measured using a digital multimeter. The I_d-V_d curves were established without gate electrode and without electrolyte.

Number of PEDOT layers	Thickness (µm)	Dynamic resistance (Ω)	Static resistance (Ω)
1	2.5	21.3	22.6
3	5.6	11.7	11.2
6	19.2	11.0	10.4

5.2.2 Characterization of the channel thickness

Channel geometry, in particular, thickness,[4] is one of the main parameters affecting OECT performance. The most popular approaches to control the CP film thickness, spin coating and inkjet printing, require dedicated equipment and are more suitable for thin-film fabrication (below 1 µm)[17]. Ultrasimple methods such as dip pen, on the other hand, have been scarcely reported for fabrication of OECTs[18, 19]. In this work, the channel geometry is controlled through a simple approach. The length is set by the gap between the Au pad electrodes (0.5 mm). The width is determined by the size of the metallic tip used as a pen, which in this work creates a uniform width in the order of 1.00 ± 0.04 mm. The channel thickness is mostly controlled by the rheological characteristics of the ink, which determines the pen loading, and also the interaction of the ink with the paper substrate, which determines the delivery of the CP ink.

As shown in Figure 5.2E, Figure 5.2F and Figure 5.2G, the total thickness of the channel were 2.55 ± 0.24 µm; 5.63 ± 0.14 µm and 19.24 ± 0.84 µm for one, three and six layers, respectively. The error in the measurements shows that the film is reasonably uniform across the channel. As expected, the thickness of the channel increases with the number of layers deposited. This growth, however, is not linear, since the thickness of the layer will depend on the delivery and the way the film dries. On average, the thickness has increased between 2 to 3 µm per applied layer. This is similar to inkjet printing of successive layers, which has been used in several works to control the thickness of thin films[20]. Therefore, multiple dip-pen could serve as a quick, simple, and low-cost alternative method to obtain thick film channels. The stability and dynamic response of the channel was tested by monitoring the current profile upon application of a square wave voltage at 0.05 Hz (50% duty cycle) during 40 cycles. In all cases, the rise and fall of the current is limited by the reading device, and it is below 1 s, well within the required performance (Figure 5.2D).

5.2.3 Electrical characterization of the OECT

The OECTs were tested by immersing the PEDOT:PSS channel and the Ag/AgCl gate electrode in a 0.1 M NaCl electrolyte solution (Figure 5.1F). After applying a drain voltage (V_d), the current (I_d) was monitored as a function of time. The gate voltage bias (V_g) was modified from 0 V to 0.9 V with 0.1 V increment steps that were applied each time I_d was stabilized. At the end of each run, voltage was set back to zero to verify the return to the baseline. This process was repeated for a different V_d, and the transconductance (g_m) was calculated as described in Section 2.3.2. It is worth noting that the dwell-time (time elapsed between two increments of the gate voltage) in the transfer and output curves (Figure 5.3) was set to 120 seconds to allow I_d to become more stable.

Figure 5.3A shows the transfer curves (I_d vs V_g) for an OECT with a 5.6 µm channel thickness (see Figure S 5.1 for 2.5 and 19.2 µm channel thickness). The plots show that the initial I_d decreases as the gate voltage is increased, which indicates that the transistor is operating in the depletion mode. This drop of I_d is attributed to the injection of cations (Na^+) from the electrolyte into the PEDOT:PSS channel, which leads to a decrease in the density of charge carriers (holes) and a drop of the electrical conductivity of PEDOT. This process –the foundation of an OECT- is usually represented as[21]:

$$\mathrm{PEDOT^+{:}PSS^- + M^+ + e^- \leftrightharpoons PEDOT^0 + PSS^-M^+} \qquad \text{Equation 5.3}$$

Where M^+ is a cation injected from the electrolyte, $PEDOT^+$ and PEDOT° are the oxidized and reduced forms of the polymer, respectively. Figure 5.3B and Figure 5.3C represent the transconductance (g_m) and the output curves of the OECT (I_d vs V_d) for different V_g, respectively. The results show that g_m increases with V_d, and that it reaches a maximum at V_g approximately 0.2 V. It has been shown that this value depends on several factors, such as the nature of the gate and the geometrical relationships of the system[22]. Moreover, the transfer curve and g_m-V_g plot represented in Figure 5.4A and Figure 5.4B, respectively, shows that g_m reaches a maximum value of 40.1 ± 3.6 mS (for N = 4). It should be stressed that the results shown correspond to a 5.6 µm channel, as it will be discussed below.

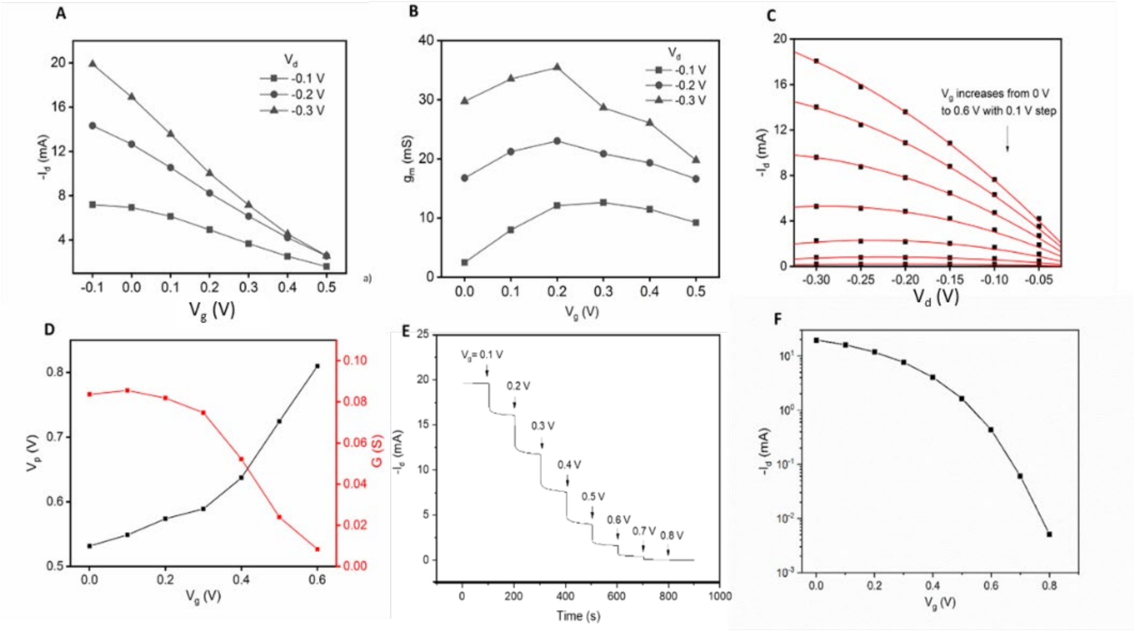

Figure 5.3. A) Transfer curve, B) transconductance and C) Output curve (fitted using Bernard-Malliaras model (red line) of an OECT with a channel made of 3 PEDOT:PSS layers (5.6 µm channel). D) Pinch-off voltage and conductance calculated from the model. E) Time trace of I_d at V_d= -0.3 V and F) corresponding transfer curve in logarithmic scale used to calculate the IOn/IOff current ratio. The drain current drops from 19.6 mA at V_g=0 V, to 5 µA at V_g=0.8 V, which gives an On/Off current ratio of 3.8x10^3. The gate used is Ag/AgCl.

Additionally, Figure 5.3E demonstrates the switching capabilities of the thick film OECT. The device was in ON state at V_g = 0 V where the drain current recorded was 19.6 mA. The OECT switched-off when V_g increased gradually from 0 to 0.8 V, where I_d reached a minimum value of 5.5 µA, -which represents the maximum de-doping of the channel-, yielding an on/off current ratio of 3.8 x10^3 (Figure 5.3F). Remarkably, these two values are among the highest figures reported for paper-based OECTs. Interestingly, good values of g_m can be obtained even at zero gate-voltage, which may be useful in several applications[23].

Figure 5.2C emphasizes the impact that has the channel thickness on gm. interestingly, channel thickness does not affect the conditions at which the maximum is reached (V_g = 0.2 V). It is also worth noticing that with 3 layers of CP, g_m reaches a maximum value and then levels off. This suggests that increasing the channel thickness beyond certain critical value may be detrimental for performance, since factors such as response time and the on/off current ratio of the transistor may be negatively affected[22]. For instance, the time constants of two channels with 3 and 6 layers determined by applying a step gate voltage from 0 to 0.4 V at V_d= -0.3 V and fitting the response to an exponential function, were 3.72 and 5.48 s, respectively, as illustrated in Figure 5.4C and Figure 5.3D. The response measured (black line) was recorded at constant V_d= -0.3 V, and by changing the gate voltage from 0 to 0.4 V. The red line represents a fitting of the measured response using an exponential function: $y = y_0 + A.\mathrm{Exp}(-x/\tau)$, where τ is the time constant of the device.

The reasons for this behavior are not yet totally clear, although problems associated to film hydration, cation migration, etc., may be playing an important role. In short, the layers below 6 µm do not seem to effectively engage in the ion-electron coupling required in OECTs. Therefore, the following experiments were conducted using an OECT with a channel thickness of approximately 6 µm, i.e. 3 layers of PEDOT:PSS. It is worth noting that the response times obtained for the OECTs with 3 and 6 layers (3.72 s and 5.48 s, respectively), are significantly higher compared to the values extracted from the OECTs with different W/L (< 1 s) studied in the previous chapter. This result is interesting, because it points out that doubling the thickness of the channel is more likely to affect the switching speed of the OECT rather than doubling W/L.

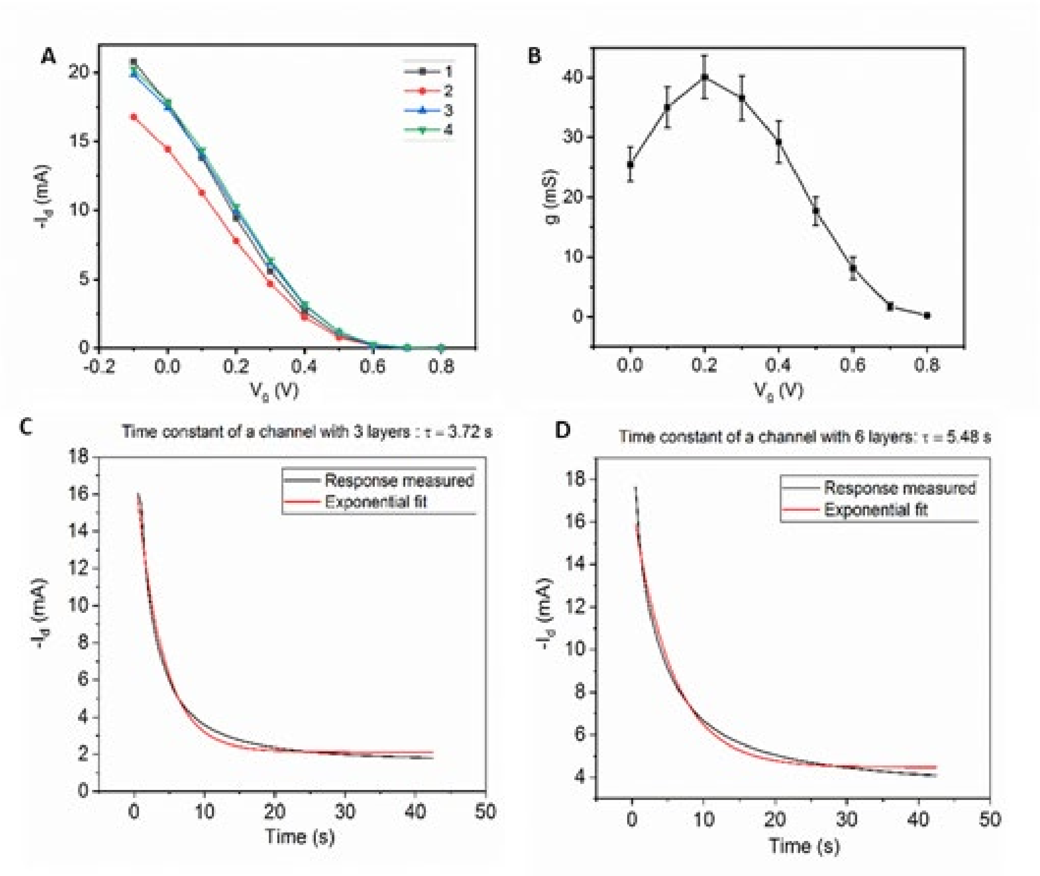

Figure 5.4. A) Transfer curves, and B) Average transconductance of N= 4 OECTs made of three Pedot:Pss layers (Ag/AgCl was used as gate electrode) at Vd= -0.3 V in NaCl (0.1 M). The maximum transconductance of all OECTs tested is at Vg= 0.2 V with an average of 40.1 ± 3.6 mS. Measured and fitted response of a channel made of C) 3 and D) 6 layers.

It should be stressed that the values of g_m reported in this work are among the highest values reported for this type of devices. Table 5.2 compares the g_m values of this work with other state-of-the-art PEDOT:PSS OECTs, showing that -to the best of our knowledge- this is the highest transconductance reported for a paper-based OECT. Very recently, OECTs with high transconductance values have been also reported[24, 25]. It should be stressed that by tuning the film composition, drying procedures, substrate and system geometry (e.g., gate to channel geometry), transconductances can be enhanced, sometimes at the expense of a more complex procedure. In the case of this work, a balance between performance and simplicity of manufacturing has been achieved. Satisfactory results have been obtained by using the unmodified CP ink (i.e., as provided by the manufacturer) on a paper substrate with a simple construction approach.

Table 5.2. Comparison of OECTs characteristics

Substrate	**Channel fabrication**	**Gate material**	**Channel Material**	**W (µm)**	**L (µm)**	**T (µm)**	**gm (mS)**	**Voltages (V)**	**Ref.**
PLA	3D printing	Ag/AgCl	PEDOT:PSS	912	694	7.1	31.8±6.3	V_d= -0.7 V_g= 0	[9]
PE	Printing	Ag/AgCl	PEDOT:PSS	1000	500	2.1	10	V_d= -0 .4 V_g= 0	[26]
Polyarylate	Spin coating	Ag/AgCl	PEDOT:PSS/ EMIM-TCM	1000	200	0.8	28.7	V_d= -0.5 V_g= 0.42	[8]
Paper	Dip pen	Ag/AgCl	PEDOT:PSS	1000	500	5.63	40.1±3.6	V_d= -0.3 V_g= 0.2	**This work**
Paper	Dip pen	Pt/Nafion	PEDOT:PSS	1000	500	6	24.5	V_d= -0.15 V_g= 0.2	**This work**
Si wafer	Spin coating	Au/PEDOT	PEDOT:PSS	500	5	6	32.3	V_d = -0.6 V_g= 0.5	[7]
Glass	Spin coating	Ag/AgCl	PEDOT:PSS	*			142	V_d = -0.6 V_g= 0.2	[24]
PET	Spin coating	Ag/AgCl	PEDOT:PSS	**			139	V_d = -0.6 V_g= 0.2	[25]

PE: Polyethylene, PLA: Polylactic acid, EMIM-TCM: 1-Ethyl-3-methylimidazolium tricyanomethanide

*interdigitated electrodes with finger number Nf = 5, finger width and channel length Wf = LCh = 5 µm and polymer film thickness d = 115 nm

**interdigitated electrodes (large comb) with finger number Nf = 6, channel length LCh = 8 µm and W/L ratio 230

5.2.4 Volumetric capacitance of the channel

Accurate models describing the fundamental processes in OECTs are still a matter of intense research[27]. While the most evident difference with FET is the volumetric capacitance of OECTs[28], Torsi and co-workers have stressed that the fundamental physical phenomena are similar in both systems, but the main difference is where and how the electric double layer (EDL) is formed[29]. In an electrolyte-gated FET the capacitance originates from EDL created on the surface of an insulator material that separates the conducting polymer or and the electrolyte. In OECT, on the other hand, the lack of this insulator material allows ions to move freely into the porous PEDOT:PSS structure. Thus, the capacitance originates on the EDL generated around the PEDOT domains. It has been shown that PEDOT forms dispersed micro and nano-structured domains in a PSS-electrolyte matrix. Therefore, the EDL is formed around these PEDOT domains, forming an extended and dispersed structure through the whole channel volume. In fact, the description of the OECT proposed by Bernards et al.,[30] is originally derived from the FETs models, providing that the interfacial (2D) capacitance is replaced by a volumetric (3D) capacitance. Therefore, the most commonly used model for an OECT in the depletion mode within the linear range, I_d relates with the device geometry and the properties of the conducting polymer:

$$I_d = \frac{G}{V_p}\left(V_p - V_g + \frac{\mathrm{V_d}}{2}\right)V_d \qquad \text{Equation 5.4}$$

where G is the initial electrical conductance of the channel and V_p is the transistor pinch-off voltage, i.e., the value of V_g at which the system is almost fully de-doped. The fit of the experimental data to Equation 5.4 using a least square method, is shown in Figure 5.3C. The model provides a good fit to the data providing that –as reported by Alcácer et al- G and V_p are used as variables. The channel conductance (G) shows an initial value of 84.5 mS (for V_g = 0 V), which is close to the initial value of resistance found for the channel (Figure 5.2C, although in this figure the resistance is lower, since the channel is dry). The results of the models (Figure 5.3D)show that for V_g above 0.2 V, G decreases sharply and reaches a value of 8.7 mS for V_g = 0.6 V. Regarding the pinch-off voltage V_p, its value increases with V_g from 0.51 V to 0.81 V, which is within the range of values that has been reported in the literature.

These results show that while thick-film OECT present similar behavior to thin-film devices, they show particular features likely due to the deviations introduced by the increased channel thickness. In fact, Bernards-Malliaras model (Equation 5.4), derived for homogeneous thin-film devices with uniform properties across the channel, and has been under scrutiny during the last few years. Lüssem and co-workers have recently demonstrated that migration of ions towards the drain electrode produces gradients of concentration that affect the pinch voltage[31]. McLeod and cowokers have demonstrated the non-uniform mobility of holes in the PEDOT, a parameter that is assumed constant in Bernards-Malliaras model[32]. In summary, the generation of concentration and electrical field gradients, together with variations in the CP properties make the system more dependent on geometrical characteristics, particularly on the film thickness. Working on adaptations of the model to thicker films should be conducted in the future.

Rivnay et al. studied the capacitance (C) as a function of the channel volume, arriving to Equation 5.5[4]:

$$C = C^{*}.WLd \qquad \text{Equation 5.5}$$

Where C*, the volumetric capacitance of the PEDOT:PSS channel, has a value of 40 F/cm^3. Considering the volume of the channel used in this work (with a volume of approximately of $2.8 \cdot 10^{-6}$ cm^3), equation 6 predicts a capacitance of 112 µF. Experimental measurements of the capacitance performed by impedance spectroscopy yield a value of capacitance of 106 µF (Figure S 5.3 is Supporting Information), which is fairly close to this value. The product of the charge carrier mobility and the volumetric capacitance (µ.C*) has been proposed as a material's figure-of-merit for benchmarking OECTs[33]. For instance, the product (µ.C*) extracted from fitting Bernards-Malliaras model to the output (Figure 5.3A and Figure 5.3B) at V_d= -0.3 V and V_g = 0 V gives a value of 139.7 F/cm.V.s, which is in agreement with the literature. Therefore, while models to describe accurately the behavior of thick-film OECTs will be required, the general properties of these devices match those of the thin-film counterparts. Thick film technology, however, provides a simplified manufacturing approach and enhanced response.

5.2.5 Detection of H_2O_2

To illustrate the advantages of thick-film transistors, a system for the detection of hydrogen peroxide was built and optimized. This molecule is widely used in biochemical sensing as an intermediary species for signal generation. During the last few years, we reported the sensitive and selective potentiometric determination of H_2O_2 using a Pt electrode coated with Nafion. Interestingly, while often referred as a redox reaction of peroxide, however, the response of the Pt electrode is due to a mixed potential mechanism involving exchange currents from different surface reactions –mainly the oxygen reduction reaction and the Pt oxidation[34]. Thus, the potentiometric measurement does not follow to a Nernstian regime, since the kinetically controlled surface reactions create concentration gradients on the electrode. Nafion enhances these surface reactions, preventing the adsorption of interfering anions, providing reactive species and stabilizing the electrode response[10]. Furthermore, its biocompatibility is ideal for the development of biosensors[35].

An OECT was built using a channel with three layers of PEDOT:PSS (W = 1 mm and L = 0.5 mm) and a paper-based Nafion-coated Pt electrode as a gate. Conditions were optimized in order to maximize the sensitivity of the detection. V_d was adjusted to -0.3 V to keep I_d below 20 mA. The use of Pt electrode introduces a new variable in the system.

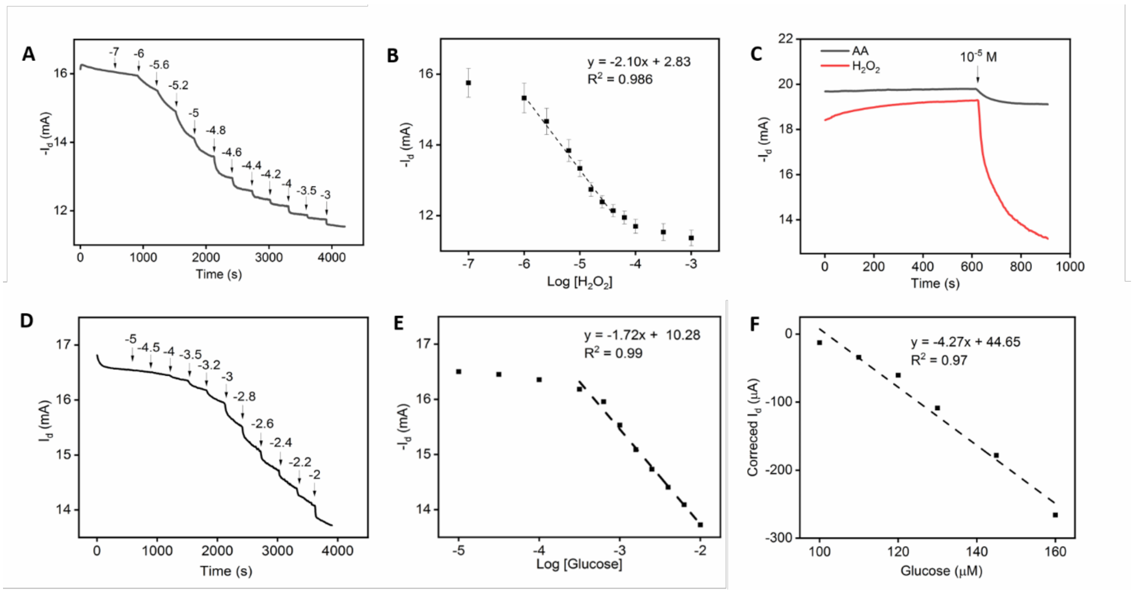

Figure 5.5. A) Time trace of the OECT response for increasing concentrations of H_2O_2 (numbers indicate logarithmic concentrations of the target). B) the corresponding logarithmic calibration curve (the error bars correspond to standard deviation of 3 sensors). C) response of a sensor to ascorbic acid (AA) and H_2O_2. D) Time trace of an OECT response for increasing concentrations of glucose. E) the corresponding logarithmic calibration curve; F) calibration curve corresponding to a 100-160 μM range. In all cases, OECT is operated at V_d = -0.3 V, V_g = 0.2 V. The numbers on the time traces represent the logarithm of the concentration of the analyte.

Ag/AgCl electrodes show a negligible capacitance, so the applied gate potential is similar to the effective gate potential. In the case of the Pt/Nafion electrode, however, the effective gate potential (V_g^{eff}) is different from the applied gate potential, since the electrode capacitance and the redox potential have to be also considered. In fact, this is the working principle of the sensor: alterations in the concentration of an electroactive species (H_2O_2) that affect the effective gate potential, will be registered as changes in I_d. In this case, equation 5 can be re-written as:

$$I_d = \frac{G}{V_p}\left(V_p - V_g^{eff} + \frac{1}{2}.V_d\right)V_d$$

Equation 5.6

Where $V_g^{eff} = V_g + V_{offset}$ .The term V_{offset} includes the capacitances at the interfaces and the redox potential of the system. Initial tests (data not shown) show that –in the absence of Pt- PEDOT shows a negligible response to peroxide. When adding peroxide with a Pt gate, however, the change in the potential of the Pt electrode is registered as a drop in the channel current. The optimization was performed by evaluating the sensitivity for the detection of peroxide at different gate potential. Optimum conditions were found for V_g = 0.2 V, V_d = -0.3V (Figure S 5.2, see S.I). The time trace of I_d upon addition of peroxide is shown in Figure 5.5A, and the corresponding calibration plot in Figure 5.5B.

The sensor displays a linear response with the logarithm of the concentration of peroxide in the range 10^{-6} to $10^{-4.4}$ M. Under optimum conditions, an outstanding sensitivity of 2.1 mA/dec is reached. This value is several orders of magnitude higher than the values reported for other similar sensors. For comparison, selected examples of OECTs reported sensitivity are shown in Table 5.2. In this work, the limit of detection is 3×10^{-7} M. While this system has not been optimized to improve the limit of detection, the value obtained is comparable to thin-film OECTs, and one order of magnitude higher than graphene-based OECT.

On the other hand, ascorbic acid (AA) is known to interfere with the electrochemical detection of H_2O_2. Figure 5.5C shows the limited response of the sensor to the addition of 10^{-5} M of ascorbic acid, a concentration that is usually considered an upper level in physiological samples. As can be observed, for the same concentration added, the change in the drain current caused by AA is significantly lower than the response to H_2O_2. This low response towards AA is attributed to the presence of the anionic groups on Nafion, which acts as a permselective barrier repelling the negatively charged AA and enhancing the detection of H_2O_2.

5.2.6 Detection of glucose

As a way to illustrate the use of the thick film for biosensing, glucose oxidase (GOx) enzyme was added to the Pt-Nafion gate. GOx acts as a catalyst for the oxidation of glucose according to:

$$D - Glucose \xrightarrow{GOx} D - Glucono - 1{,}5 - lactone + H_2O_2 \qquad \text{Equation 5.7}$$

In this reaction, H_2O_2 is a by-product that alters the potential of the platinum electrode, causing a change in the channel conductivity, as discussed above. The time trace with the response of the sensor to increasing concentration of glucose is shown in Figure 5.5D, and the corresponding calibration curve is shown in Figure 5.5E. The sensitivity in this case is 1.72 mA/dec and the limit of detection is 1.10^{-4} M. The linear range spans from $10^{-3.5}$ to 10^{-2} M. These values are acceptable to cover, for example, the normal range of glucose in blood. Optimization of these values can be achieved by modifying the gate characteristics. Linear ranges, for example, can be adjusted by replacing Nafion by other ionomeric materials. The limit of detection can be further improved by optimizing the area of the gate, the volume and the concentration of Nafion/GOx deposited. Moreover, the integration of Pt nanoparticles, CNT, and/or graphene in the gate electrode have proven to enhance the limit of detection, and shift the linear range towards small concentrations of glucose (Table 5.2)[36, 37]. All this will depend on the type of biological fluid that will be target.

To validate the specificity of the response, the response to glucose of an OECT without GOx was evaluated, and the response is shown in Figure S 5.4A. The first part of this figure shows the initial drop of current produced by setting the gate at 0.2V. This is a rather large potential step, and for that reason stabilization time is relatively long. After that, the GOx-free sensor does not show any significant response to the addition of three concentrations of glucose 10^{-5}, 10^{-4} and 10^{-3} M.

Clearly, with an enhanced sensitivity and a response time in the order of tens of seconds, these thick film transistors offer a valuable approach for chemical and biochemical sensing. In terms of detectability, they offer enhanced sensitivity due to the power amplification provided by OECTs. In a very recent work regarding this topic, Malliaras et al. discussed the issues of thickness and noise level, concluding –in line with this work- that channel thickness should be increased as much as allowed by the response time[38]. In this work, currents in the order of a few mA show noise levels in the single µA range (typically, a 10 mA current shows a standard deviation of 2 10^{-3} mA). Figure 5.5F and Figure S 5.4B show a calibration plot between 100 and 160 µM of glucose, illustrating the enhanced power of detection provided by the high sensitivity of the OECT, i.e. 4.27 µA/ µM. These values can be improved considering that the noise observed is heavily influenced by the ripple of the commercial, low-cost power supplies used. In fact, by using a stabilized DC power supply, the standard deviation of the I_d can go down below 8 10^{-5} mA. Considering sensitivities of 2 mA/decade, this noise level provides a very attractive signal to noise ratio. Alternatively, it has been shown that simple approaches to signal amplification –such as the use of a load resistor- can provide significant signal improvements. It should be stressed that the traditional potentiometric methods working under zero current conditions (i.e., currents well below picoamps), signals of a few hundreds of millivolts will result in signals well below nano or pico watt power. The significantly higher power of the OECT signals provides room for signal enhancement.

5.3 Conclusions

In the present work, we demonstrated the potential of thick film OECTs, and the possibility for simple casting methods such as dip pen to conveniently create high performance devices. The use of thick film OECTs in chemical sensing encompasses several advantages. First, the high transconductance achieved by these devices provides enhanced analytical figures, such as high sensitivity and signal-to-noise ratio. Second, the practical advantages of a low cost and simple manufacturing approach. The possibility to build manually reproducible paper-based OECT sensors facilitates their adoption and further exploration. In summary, these paper-based thick-film OECTs open new and attractive avenues for the development of highly sensitivity, powerful, simple and low-cost chemical and biochemical sensors.

5.4 Supporting information

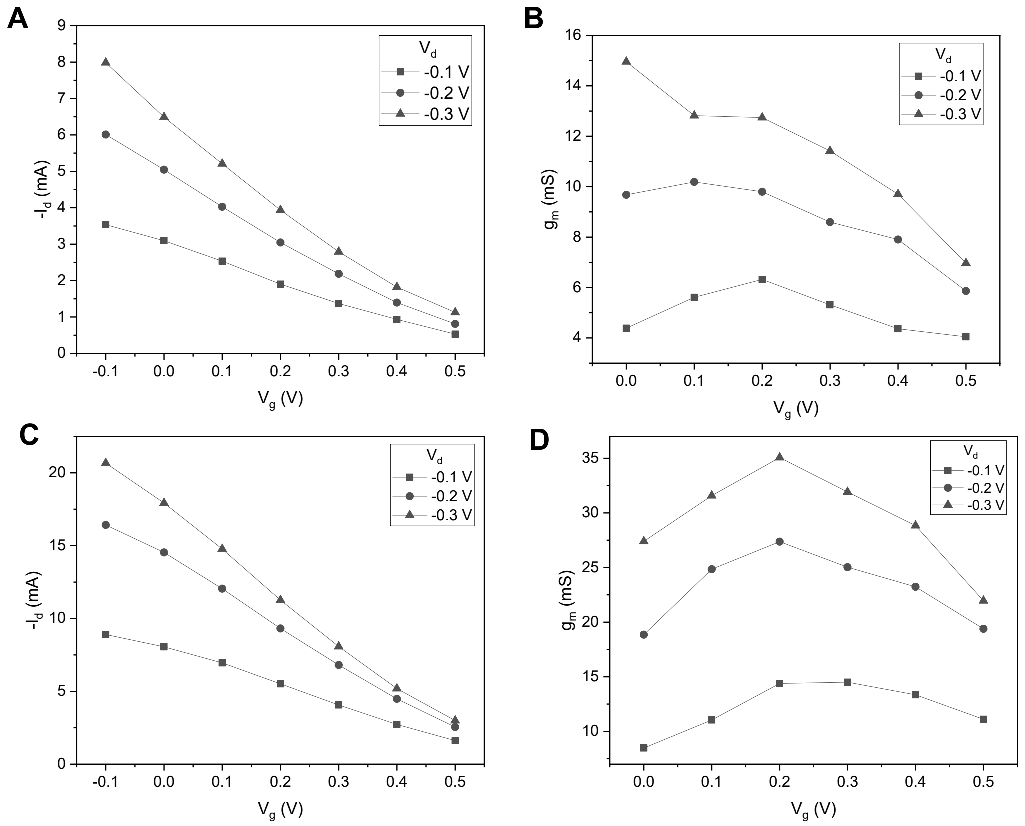

Figure S 5.1. A) Transfer curve and B) transconductance of an OECT with a channel made of 1 PEDOT:PSS layer. C-D) are the characteristic curves of the OECT with 6 layers (the gate electrode is Ag/AgCl).

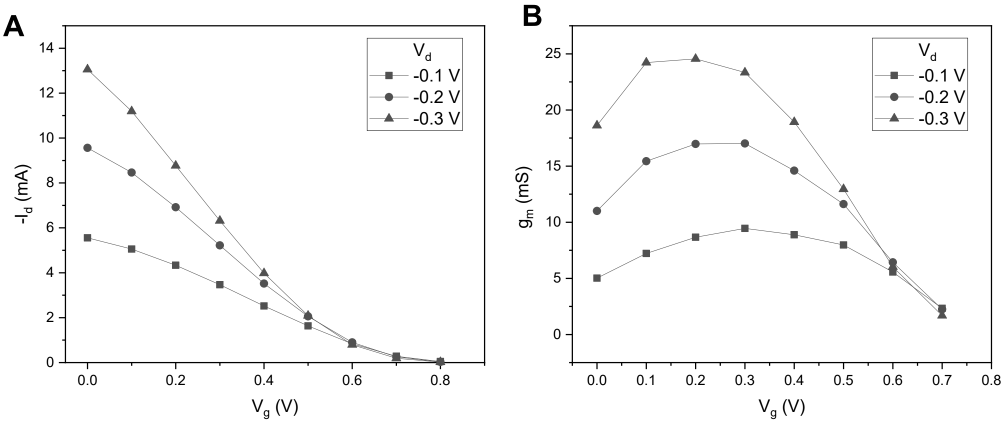

Figure S 5.2. A) Transfer curves of an OECT using platinum coated with nafion as gate electrode. B) corresponding transconductance curves. The length, width and thickness of the channel are 0.5 mm, 1 mm, and 2.5 µm respectively.

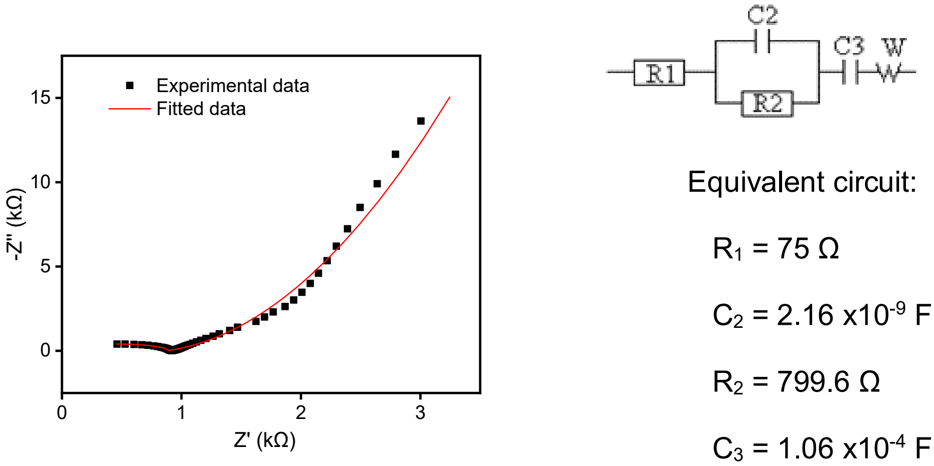

Equivalent circuit:

R_1 = 75 Ω

C_2 = 2.16 x10^{-9} F

R_2 = 799.6 Ω

C_3 = 1.06 x10^{-4} F

S = 2044 Ω.$s^{1/2}$

Figure S 5.3. Electrochemical impedance spectra of the same channel fitted to Randles circuit and the corresponding parameters of the equivalent circuit including a Warburg impedance W.

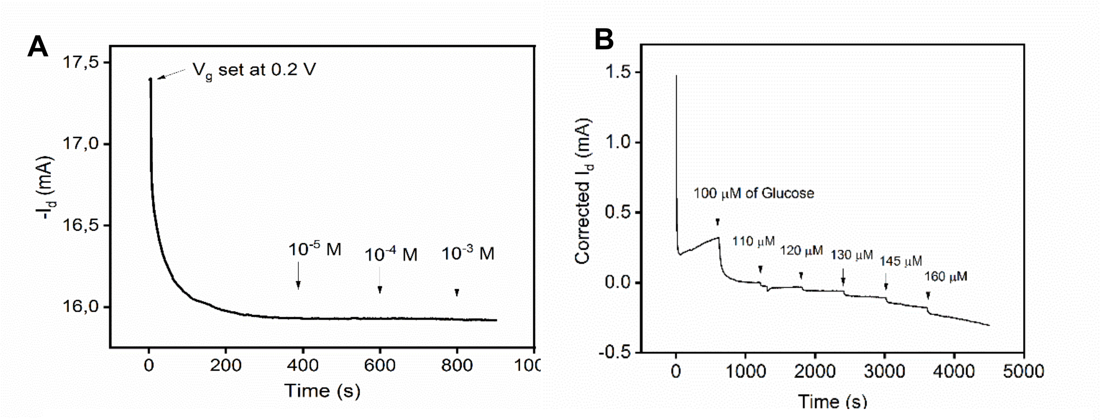

Figure S 5.4. A) Response of a sensor to glucose using a Pt gate without the enzyme GOx. B) Time trace of an OECT response for increasing concentrations of glucose in the 100-160 µM

5.5 References

[1] Rivnay, J.; Leleux, P.; Sessolo, M.; et al., *Adv Mater*, **2013**, 25, 7010-70104.

[2] Volkov, A. V.; Wijeratne, K.; Mitraka, E.; et al., *Adv Funct Mater*, **2017**, 27, 1-10.

[3] Khodagholy, D.; Rivnay, J.; Sessolo, M.; et al., *Nat Commun*, **2013**, 4, 2133.

[4] Rivnay, J.; Leleux, P.; Ferro, M.; et al., *Sci Adv*, **2015**, 1, e1400251.

[5] Friedlein, J. T.; McLeod, R. R.; Rivnay, J., *Org Electron*, **2018**, 63, 398-414.

[6] Wang, N.; Yang, A.; Fu, Y.; et al., *Acc Chem Res*, **2019**, 52, 277-287.

[7] Spyropoulos, G. D.; Gelinas, J. N.; Khodagholy, D., *Sci Adv*, **2019**, 5, eaau7378.

[8] Wu, X.; Surendran, A.; Ko, J.; et al., *Adv Mater*, **2019**, 31, e1805544.

[9] Fan, J.; Montemagno, C.; Gupta, M., *Org Electron*, **2019**, 73, 122-129.

[10] Parrilla, M.; Cánovas, R.; Andrade, F. J., *Electroanalysis*, **2017**, 29, 223-230.

[11] Guo, X.; Cao, Q.; Liu, Y.; et al., *Anal Chem*, **2020**, 92, 908-915.

[12] Tang, H.; Yan, F.; Lin, P.; et al., *Adv Funct Mater*, **2011**, 21, 2264-2272.

[13] Liao, J.; Lin, S.; Yang, Y.; et al., *Sens Actuators B: Chem*, **2015**, 208, 457-463.

[14] Pappa, A. M.; Curto, V. F.; Braendlein, M.; et al., *Adv Healthc Mater*, **2016**, 5, 2295-2302.

[15] Kaphle, V.; Liu, S.; Al-Shadeedi, A.; et al., *Adv Mater*, **2016**, 28, 8766-8770.

[16] Pesavento, P. V.; Puntambekar, K. P.; Frisbie, C. D.; et al., *J Appl Phys*, **2006**, 99, 094504.

[17] Kholghi Eshkalak, S.; Chinnappan, A.; Jayathilaka, W. A. D. M.; et al., *Applied Materials Today*, **2017**, 9, 372-386.

[18] Minari, T.; Kanehara, Y.; Liu, C.; et al., *Adv Funct Mater*, **2014**, 24, 4886-4892.

[19] Cho, J.; Cheon, K. H.; Ahn, H.; et al., *Adv Mater*, **2015**, 27, 5587-5592.

[20] Moya, A.; Gabriel, G.; Villa, R.; et al., *Curr Opin Electrochem*, **2017**, 3, 29-39.

[21] Robinson, N. D.; Svensson, P.-O.; Nilsson, D.; et al., *J Electrochem Soc*, **2006**, 153, H39-H44.

[22] Hütter, P. C.; Rothländer, T.; Haase, A.; et al., *Appl Phys Lett*, **2013**, 103, 1-5.

[23] Yu, S.; Ratcliff, E. L., *ACS Appl Mater Interfaces*, **2021**, 13, 50176-50186.

[24] Liang, Y.; Brings, F.; Maybeck, V.; et al., *Adv Funct Mater*, **2019**, 29, 1902085.

[25] Tyrrell, J. E.; Boutelle, M. G.; Campbell, A. J., *Adv Funct Mater*, **2020**, 31, 2007086.

[26] Romele, P.; Ghittorelli, M.; Kovacs-Vajna, Z. M.; et al., *Nat Commun*, **2019**, 10, 3044.

[27] Colucci, R.; Barbosa, H. F. d. P.; Günther, F.; et al., *Flex Print Electron*, **2020**, 5, 013001.

[28] Proctor, C. M.; Rivnay, J.; Malliaras, G. G., *J Polym Sci, Part B: Polym Phys*, **2016**, 54, 1433-1436.

[29] Macchia, E.; Picca, R. A.; Manoli, K.; et al., *Materials Horizons*, **2020**, 7, 999-1013.

[30] Bernards, D. A.; Malliaras, G. G., *Adv Funct Mater*, **2007**, 17, 3538-3544.

[31] Kaphle, V.; Paudel, P. R.; Dahal, D.; et al., *Nat Commun*, **2020**, 11, 2515.

[32] Friedlein, J. T.; Shaheen, S. E.; Malliaras, G. G.; et al., *Adv Electron Mater*, **2015**, 1, 1500189.

[33] Inal, S.; Malliaras, G. G.; Rivnay, J., *Nat Commun*, **2017**, 8, 1767.

[34] Baez, J. F.; Compton, M.; Chahrati, S.; et al., *Anal Chim Acta*, **2020**, 1097, 204-213.

[35] Kim, G.; Kim, H.; Kim, I. J.; et al., *J Biomater Sci Polym Ed*, **2009**, 20, 1687-1707.

[36] Liao, C.; Zhang, M.; Niu, L.; et al., *J Mater Chem B*, **2013**, 1, 3820-3829.

[37] Zhang, M.; Liao, C.; Mak, C. H.; et al., *Sci Rep*, **2015**, 5, 8311.

[38] Polyravas, A. G.; Schaefer, N.; Curto, V. F.; et al., *Appl Phys Lett*, **2020**, 117, 073302.

6 PEDOT:PSS/Nanomaterials Composites Chemiresistors For The Detection Of H_2O_2

Summary

In this chapter, PEDOT:PSS-nanoparticles composites were prepared and utilized to construct thick film electrochemical devices. Four nanomaterials (platinum nanoparticles, prussian blue, reduced graphene oxide, and zinc oxide) known for their catalytic activity were combined with PEDOT:PSS to create OECTs and chemiresistors. The devices were then characterized and tested for the detection of hydrogen peroxide.

6.1 Introduction

As it has been discussed in the previous chapter, highly sensitive OECTs can be built by deposition of PEDOT:PSS thick films via simple approaches (e.g. dip pen or drop casting), and utilizing platinum paper as gate electrode. This approach does not require operating in a clean room, and simplifies considerably the fabrication of OECTs. Up to this point, the sensing element of the sensor is incorporated onto the surface of the gate electrode. When the analyte interacts with the gate electrode, a potential drop occurs across the gate-electrolyte interface. This potential drop affects the injection of cations into the PEDOT:PSS channel, enabling the modulation of the oxidation state of the conductive polymer (CP). Since the electrical conductivity of the CP depends on its oxidation state, the current that flows through the channel changes. Alternatively, instead of the gate electrode, the channel can be sensitized by functionalizing it with biomolecules or nanoparticles. Since the event that triggers the detection takes place near the channel, the role of the gate electrode in the detection process is diminished. As a result, the oxidation state of the CP can be directly modulated because of the physical contact between the CP and the nanoparticles, provided the interaction between the two elements impedes the mobility of charge carriers in the CP. This approach can be extended and generalized by incorporating different types of nanoparticles in PEDOT:PSS.

Different conductive polymer and/or nanomaterials composites have been reported in the literature for bio- and chemical sensors, among other applications.[1-3] For instance, Berggren and co-workers constructed an enzymatic OECT based on PEDOT:PSS-platinum nanoparticles composite and choline oxidase capable of detecting acetylcholine.[4] The OECT operated at V_d = -0.2 V and V_g = +0.4 V, while exhibiting a sensitivity of 4.1 $A.mol^{-1}.L.cm^{-2}$ and linear range from 0.9-14 µM.

Iron(III) hexacyanoferrate, commonly referred to as Prussian Blue (PB), exhibit excellent catalytic activity that mimic peroxidase enzymes.[5, 6] For this reason, PB has been used extensively to build electrochemical sensors for the detection of H_2O_2, providing an alternative that is more stable than enzymes and more affordable compared to noble metals such as platinum and palladium. Its properties in terms of catalytic activity, redox reversibility, and biocompatibility makes it an interesting material for various modern applications including, electrochemical sensors,[7] energy storage,[8] and fuel cells.[9] For instance, Lin et al. developed an amperometric sensor for H_2O_2 via electrodeposition of PB on a 3D network of polypyrrole nanowires.[10] The sensor functioned at low potentials (-0.05 V vs Ag/AgCl electrode), which minimized interferences with ascorbic acid, while exhibiting a linear range from 0.2 - 7.2 mM, and a sensitivity of 10 $\mu A.mM^{-1}.cm^{-2}$. Apart from chemical sensing, PEDOT:PSS-PB is an excellent material for building batteries and fuel cells, particularly the ones that run on H_2O_2.[11] In this regard, Shaegh et al. and Miglbauer et al. constructed one-compartment H_2O_2 fuel cell that generates a remarkable power density by employing PEDOT:PSS-PB composites. [9, 12]

Graphene is an allotrope of carbon that exhibits remarkable mechanical, catalytic, optical, and electrical properties, which makes it the focus of various research areas[13]. Its honeycomb structure and π-π conjugation place it among the most electronic conductive materials on earth. However, the major drawback of graphene is its insolubility, which limits its processibility in solutions.[14] To overcome this issue while maintaining some of its key properties, graphene is chemically transformed into its derivative graphene oxide (GO) by a strong oxidant such as sulphuric acid. This transformation generates various oxygenated groups (carboxyl, carbonyl, etc.) and renders GO much more soluble. GO can reduced via microwave or chemical reduction, which results in reduced graphene oxide (rGO). Although GO and rGO retain their hexagonal structure, rGO displays significant differences compared to GO, with high electrical conductivity, less defects, and small carbon-oxygen ratio.[15]

rGO has been reported to have excellent capacitance and catalytic activity. rGO is typically combined with polyelectrolytes such as Nafion or chitosan, or conductive polymers to create nanocomposites that exhibit properties. More exhaustive review articles have been published about the sensing capabilities of GO and rGO based sensors.[16, 17] For instance, Liao et al. have reported an OECT for the detection of glucose through the modification of a platinum gate electrode with rGO and glucose oxidase[18]. The sensor showed a sensitivity of 370 mV and a linear range within 0.01 µM -1 µM. Wang et al. developed a woven OECT by coating polyamide fibres with polypyrrole and rGO. When the gate fibre electrode was functionalized with glucose oxidase, the sensors was able to detect glucose with a sensitivity of 0.773 NR.dec^{-1} and a linear range of 1 nM - 5 µM.[19]

Zinc oxide nanoparticles (ZnO) is a semiconducting material with a wide band gap, which exhibits interesting optical properties in the ultraviolet-visible region.[20] For this reason, ZnO have been integrated in different sensors for H_2O_2 detection. As an example, Sodzel et al. constructed an optical sensor for the indirect detection of H_2O_2 and glucose by incorporating ZnO nanoparticles. Under ultraviolet-visible light, the luminescence of ZnO nanoparticles decreased in the presence of hydrogen peroxide due to quenching. Sivalingam et al. reported a H_2O_2 chemiresistive sensor based on thin film nanostructured ZnO.[21] The sensor operated optimally at a temperature range 323 K - 373 K, and showed resistance values up to 1 GΩ with a detection limit of 6 ppm (1.76×10^{-4} M).

In this chapter, we prepared different PEDOT:PSS composites dispersions by embedding four nanomaterials in a PEDOT:PSS matrix via a simple mixing process. The composites where then cast to build chemiresistors and OECTs. The devices were characterized electrically and electrochemically, and then tested for the detection of hydrogen peroxide.

6.2 Fabrication of the sensor

The main advantage of functionalizing the channel is that the system can be employed as either an OECT or a chemiresistor. To promote the catalytic activity of PEDOT:PSS, four nanomaterials were selected: reduced graphene oxide (rGO), platinum nanoparticles (PtNPs), Prussian blue nanoparticles (PB), and zinc oxide (ZnO).

As illustrated in Figure 6.1, each PEDOT:PSS/nanoparticles composite was prepared by adding 20 µL of the nanoparticles suspended in ethanol (5 mg/mL) to 180 µL of a commercial PEDOT:PSS (3.1 %wt). Next, each composite was sonicated for 30 min to ensure the homogeneity and the dispersion of nanoparticles. After sonication, a micropipette was used to drop-cast approximatively 4 µL of the composite on the active window of the device (Ø4 mm), to either make the gate electrode or the channel.

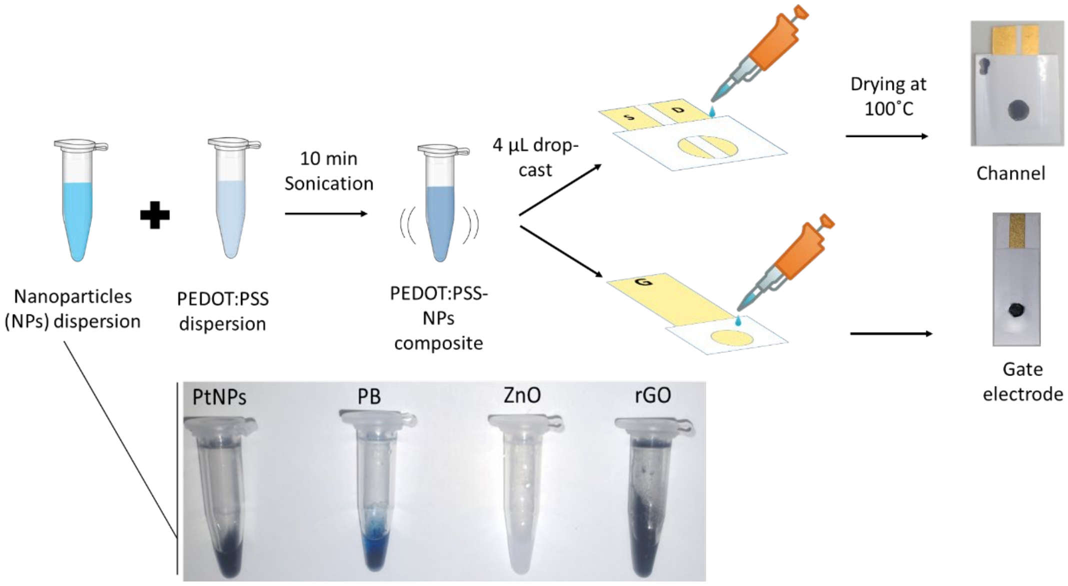

Figure 6.1. Description of the fabrication steps of the sensors, and the nanoparticles suspended in ethanol.

6.3 Results and discussion

6.3.1 TEM characterization

Surface morphology of the composites and dispersion of the nanoparticles within the PEDOT:PSS matrix were analyzed using scanning electron microscopy (SEM), and transmission electron microscopy (TEM), respectively. Figure 6.2A-C displays TEM images of platinum, zinc oxide, and prussian blue nanoparticles imbedded within the PEDOT:PSS matrix. The images show that the nanoparticles are homogeneously distributed in the PEDOT:PSS matrix, with a minimal aggregation. The diameter of nanoparticles was estimated from TEM images, and shows that the PtNPs have the smallest diameter, whereas ZnO and PB have 18.1 ± 7.2 nm and 29.2 ± 6.7 nm, respectively. Figure 6.2D shows a PEDOT:PSS-rGO composite featuring a large semi-transparent single-layer rGO sheet with darker edges and a surface area of ≈1 µm^2. The presence of π-π stacking/ interactions combined with the large surface area of rGO sheets, allow PEDOT:PSS and rGO to form an intimate contact which improves the stability and homogeneity of the composite.[22] In addition to the close contact, the similar work functions of PEDOT:PSS (5.1 eV) and rGO (4.9 eV) is reported to enhance the charge transfer of the composite.[23, 24] In contrast, SEM images (S1) does not show any significant difference between the morphologies of the composites.

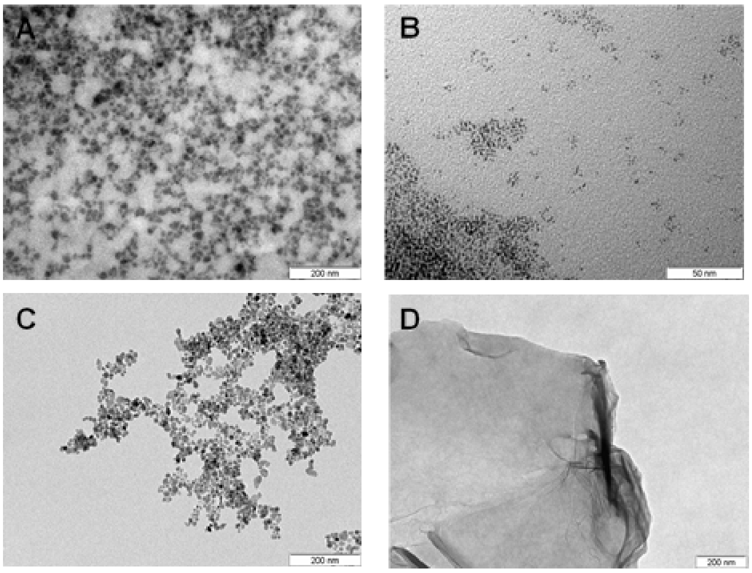

Figure 6.2. TEM micrographs of the four PEDOT:PSS composites: A) PEDOT:PSS -PB, B) PEDOT:PSS -PtNPs, C) PEDOT:PSS-ZnO, and D) PEDOT:PSS -rGO.

6.3.2 Electrical characterization of the composites

Figure 6.3A displays cyclic voltammograms of the composites in the potential range of -0.3 V to 0.3 V at 100 mV/s, in 0.1 M KCl. In this range, the composites exhibit a rectangular-like shape, which is characteristic of a non-faradaic current. In the absence of faradaic currents (due to redox reactions), this current reflects the movement of ions and increases with the potential applied until it reaches a steady-state. The rectangular shape is typically associated with the charging of the double layer capacitance (DLC).[25] This is in agreement with the fact that PEDOT:PSS exhibit high specific and volumetric capacitance.[26, 27]

Moreover, the charge-discharge curves of the four composites were also collected at constant current (500 μA) via galvanostatic charge-discharge (GCD). The results are plotted in Figure 6.3B, and show a symmetric increase and decrease of the voltage with the charging current. The slop of the linear charge segment ($\mathrm{Slop} = \frac{\Delta V}{\Delta t}$) is typically used to estimate the capacitance,[28] according to Equation 6.1:

$$C = i \times \frac{\Delta t}{\Delta V} \qquad \text{Equation 6.1}$$

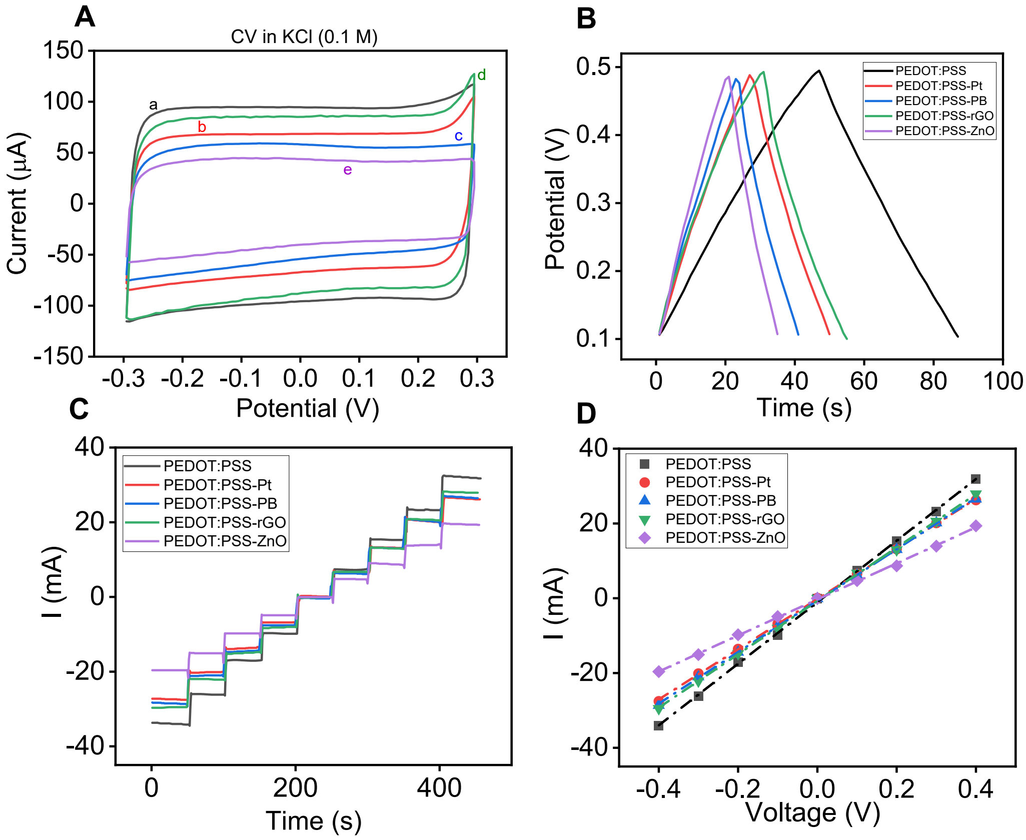

Figure 6.3. A) Cyclic voltammograms of a- PEDOT:PSS, b- PEDOT:PSS-Pt, c- PEDOT:PSS-PB, d- PEDOT:PSS-rGO, e- PEDOT:PSS-ZnO, in KCl (0.1 M) between -0.3 V and +0.3 V at 100 mV/s. B) Galvanostatic charge-discharge (GCD) of the composites in KCl 0.1 M with cut-off voltage +0.1 V and +0.5 V. C) Time trace of the output curve of the composites in 0.1 M NaCl, and D) corresponding Output curves I-V acquired by immersing each channel in NaCl 0.1 M and recording the current while the voltage applied between the two electrodes of the channel is varied from -0.4 V to +0.4 V at 50 s intervals.

Where C is the areal capacitance in F.cm^{-2}, i is the charging current, A is the area covered with the PEDOT:PSS composite, Δt is the charging time (s), and ΔV is the voltage window in Volt. Table 6.1 shows the calculated values of the specific capacitance, and indicates that a decrease in the capacitance of all the composites in comparison with PEDOT:PSS (454.6 mF.cm^{-2}). The highest capacitance among the composites was observed for PEDOT:PSS-rGO (303.9 mF.cm^{-2}), while the lowest value was recorded for PEDOT:PSS-ZnO (199.7 mF.cm^{-2}). It is worth mentioning that the capacitance of PEDOT:PSS can be up to 800 mF.cm^{-2}, and vary significantly depending on solvent treatment[29], annealing temperature,[30] and measurement method. The nature of the nanoparticles may also play a role in the overall capacitance of the composite.

Table 6.1. Summary of the conductance and specific capacitance of the composites.

Composite	**Specific capacitance ($mF.cm^{-2}$)**	**Conductance (mS)**	**R^2**
PEDOT:PSS	454.6	82.3	0.99
PEDOT:PSS-Pt	269.1	67.1	0.99
PEDOT:PSS-PB	235.9	68.8	0.99
PEDOT:PSS-rGO	303.9	71.4	0.99
PEDOT:PSS-ZnO	199.7	48.2	0.99

The ohmic response of the composites was also evaluated in NaCl 0.1 M. Figure 6.3C and Figure 6.3D display the output curves of the composites. As expected, the PEDOT:PSS composites displayed a linear current-voltage relationship within the voltage window tested, which implies a good ohmic region. As summarized in Table 6.1, the highest conductance was recorded for PEDOT:PSS with 82.35 mS, while the lowest value is for ZnO composite with 48.24 mS. This decrease in the conductivity of PEDOT:PSS-ZnO composite could be attributed to the poor electrical properties of the semiconductor ZnO, which has a large band gap of 3.1 eV.

The stability of the devices was also evaluated via cyclic voltammetry by subjecting the composites to 100 consecutive cycles at a scan rate of 100 mV/s in NaCl 0.1 M. Figure S 6.1 (See S.I) presents the voltammograms corresponding to the four composites, highlighting the first and the last cycle. The results show that pristine PEDOT:PSS, PB, and PtNPs composites demonstrate a reproducible and stable cycling after 100 cycles, which indicates that the composites maintained their capacitive and electrochemical properties. Conversely, the maximum current ZnO composite, in particular, decreased significantly after each cycle compared to pristine PEDOT:PSS, which may suggest that PEDOT:PSS- ZnO composite is unstable.

6.3.3 Electrochemical characterization of the composites

The amperometric response of the composites was also recorded by immersing the device in 5 mL cell of a phosphate-buffered saline solution (0.1 M PBS) pH = 7.4 under stirring, in a three-electrode cell. A voltage bias V = -0.1 V was applied to the working electrode versus Ag/AgCl electrode and the current was recorded. After the current has been stabilized, the analyte was added using a micropipette.

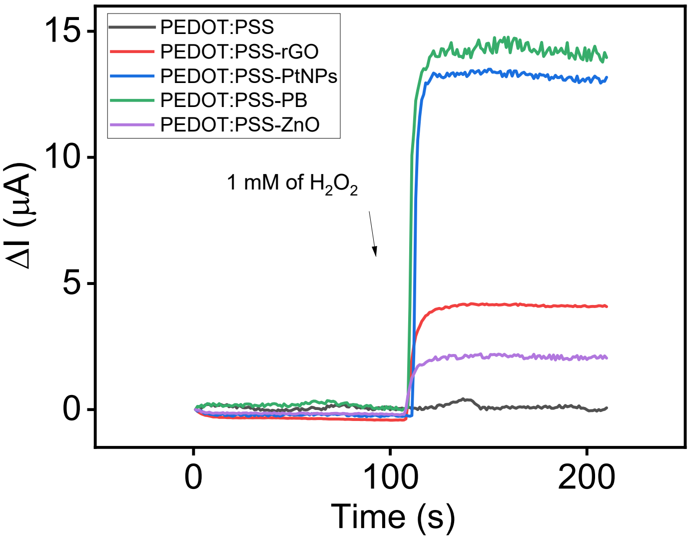

Figure 6.4. Chronoamperometric response of the composites and pristine PEDOT:PSS to the addition of 1 mM of H_2O_2 in a three-electrode cell using a Ag/AgCl reference electrode and a platinum wire as counter electrode, at -0.3 V vs Ag/AgCl.

Figure 6.4 displays the amperometric responses of the PEDOT:PSS composites to the addition of 1 mM of hydrogen peroxide at 0.1 V versus Ag/AgCl. The four PEDOT:PSS composites responded differently to the addition of H_2O_2. The highest response was obtained with PP-PtNPs and PP-PB sensors, showing a current change of 13.8 µA and 14.7 µA, respectively. In addition, the response time of the sensors was relatively short, with 90% of the total response reached under 15 s. In contrast, the blanc sensor which is made of pristine PEDOT:PSS only, did not show any significant response to H_2O_2. Therefore, the possibility that the response of the sensors could originate from the direct interaction of H_2O_2 and PEDOT:PSS can be safely ruled out.

6.3.4 Detection of hydrogen peroxide

Chemiresistor mode

The responses of the four PEDOT:PSS/nanomaterials composites in chemiresistor mode to the successive additions of H_2O_2 are presented in Figure 6.5 . In this mode, all the devices were tested in the same conditions under a bias voltage of -0.3 V without a gate electrode. The current (I) is recorded and left to stabilize, then the concentration of H_2O_2 in the electrolyte is progressively increased from 1 µM to 10 mM, at constant intervals of 300 s.

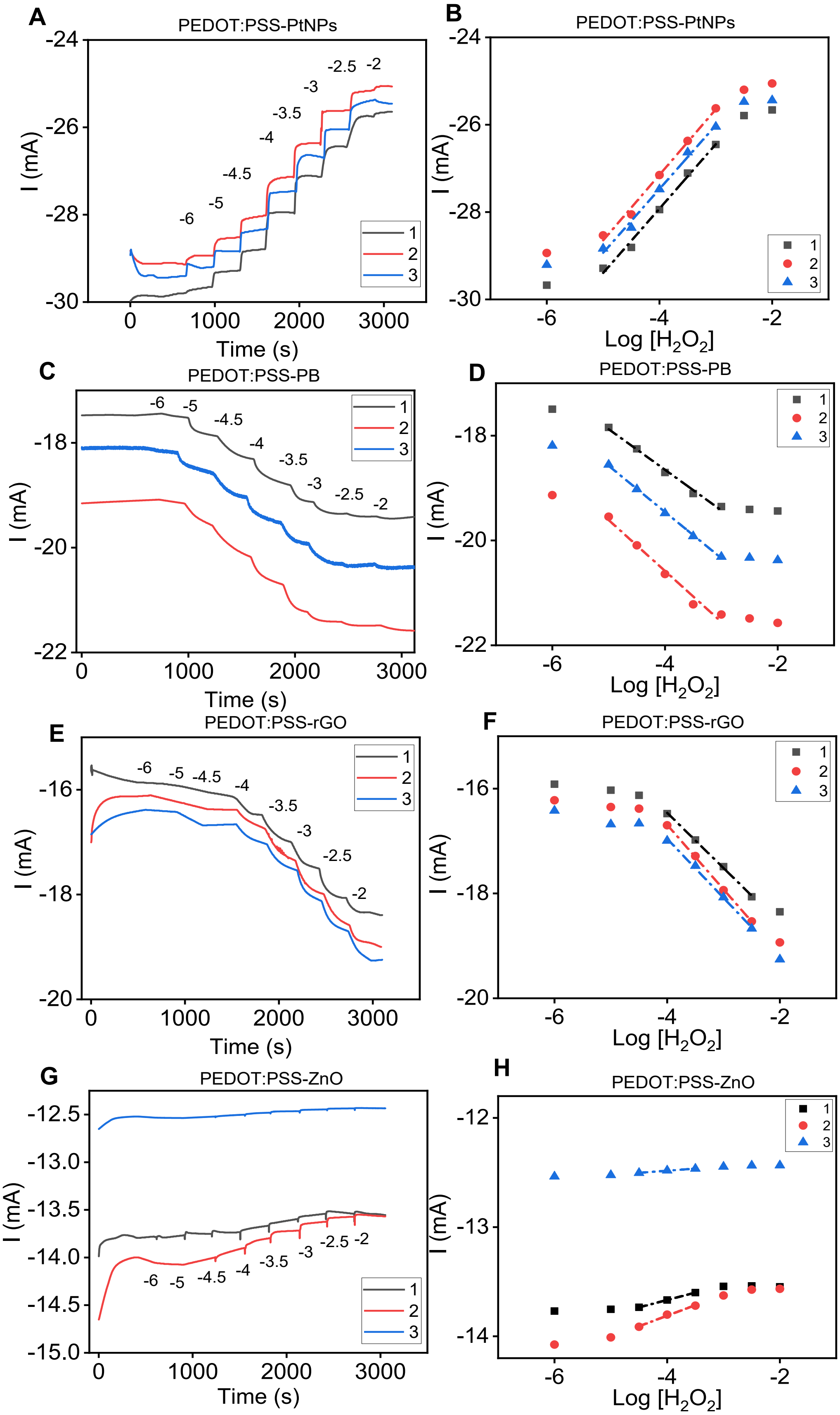
A
PEDOT:PSS-PtNPs
I (mA)
Time (s)
-6
-5
-4.5
-4
-3.5
-3
-2.5
-2
1
2
3
B
PEDOT:PSS-PtNPs
I (mA)
Log [H_2O_2]
C
PEDOT:PSS-PB
I (mA)
Time (s)
D
PEDOT:PSS-PB
I (mA)
Log [H_2O_2]
E
PEDOT:PSS-rGO
I (mA)
Time (s)
F
PEDOT:PSS-rGO
I (mA)
Log [H_2O_2]
G
PEDOT:PSS-ZnO
I (mA)
Time (s)
H
PEDOT:PSS-ZnO
I (mA)
Log [H_2O_2]

Figure 6.5. Time trace of ΔI_d for chemiresistors showing the increasing additions of H_2O_2 from -6 to -2, for composites A) PEDOT:PSS-PtNPs, C) PEDOT:PSS-PB, and E) PEDOT:PSS-rGO, and G) PEDOT:PSS-ZnO. B), D), F) and G) are the corresponding ΔI_d-log[H_2O_2] plots. F) Comparison of the sensitivities of all the OECT.

Upon the addition of H_2O_2, the composites displayed different responses and analytical performances. First, for PEDOT:PSS-PtNPs chemiresistor, the hydrogen peroxide induced a decrease in the current (in absolute value), which can be viewed as a decrease in the conductivity of the composite, particularly of PEDOT:PSS. The real mechanism underlying the response of PEDOT:PSS/PtNPs composites to H_2O_2 is not well understood. However, It is possible to rationalize its response in terms of the individual properties of PEDOT:PSS and PtNPs. Since the reduced form of the conductive polymer (PEDOT^0) is less conductive than its oxidized form (PEDOT$^+$), and H_2O_2 can undergo an oxidation reaction on the surface of platinum,[31, 32] it can be hypothesized that the addition of H_2O_2 favors the formation PEDOT^0. The decrease in the conductivity of PEDOT:PSS as result of the addition of H_2O_2 was also reported in the literature when PEDOT:PSS/horseradish peroxidase was used instead of PEDOT:PSS-PtNPs.[33] Moreover, as summarized in Table 6.2, the PEDOT:PSS-PtNPs sensors demonstrated higher sensitivity and wider linear range in comparison to the other composites, with a sensitivity of 1.47 ± 0.02 mA in the linear range between -5 and -3 (Table 6.2).

Second, PEDOT:PSS-PB and PEDOT:PSS-rGO composites in Figure 6.5C and Figure 6.5E, respectively, demonstrated an opposite response when compared to PtNPs. For these two composites, the addition of H_2O_2 induced an increase of the current recorded, which is equivalent to the increase in the conductivity of PEDOT:PSS. With respect to PB, Karyakin and co-workers have suggested in their seminal work that the mechanism underlying the detection of H_2O_2 via PB involves the electro-reduction of H_2O_2 to OH^- in the presence of O_2, at neutral or acidic pH.[34, 35] By analogy, it can be inferred that H_2O_2 favors the formation of the conductive form of the polymer which is PEDOT$^+$.

Table 6.2. Analytical performance of PEDOT:PSS composites toward H_2O_2 (N = 3)

Composite	**Sensitivity mA/dec**	**Linear range**	**R^2**
PEDOT:PSS-PtNPs	1.48 ± 0.02	-5 to -3	0.99
PEDOT:PSS-PB	-0.87 ± 0.10	-5 to -3	0.99
PEDOT:PSS-rGO	-1.14 ± 0.09	-4 to -2.5	0.99
PEDOT:PSS-ZnO	0.12 ± 0.08	-4.5 to -2.5	0.99

OECT mode

In a standard OECT sensor, the analyte interacts with the recognition element that is located at the gate electrode, while the response is measured at the level of the PEDOT:PSS channel.[36] To evaluate the impact of the dual functionalization of the gate electrode and the channel on the response of the sensors to H_2O_2, two configurations of OECTs were tested: standard and dual. In the standard OECT, the channel is made of pristine PEDOT:PSS, whereas the gate electrode is a PEDOT:PSS-nanoparticles composite. In the dual OECT, both the channel and the gate electrode are made of the same PEDOT:PSS composite. The gate electrodes were constructed according to Figure 6.1, where 4 µL of PEDOT:PSS composites were drop cast on gold electrodes. PEDOT:PSS-ZnO was not tested due to instability issues.

Figure 6.6 displays the response of the three OECTs to the increasing concentration of H_2O_2 in the range 1 µM -10 mM. All the devices were tested at the same operating voltages of V_d = -0.3 V and V_g = 0.4 V. The results shows that all the sensors demonstrated a response to H_2O_2 involving a decrease of the drain current I_d. As discussed previously, the decrease of I_d indicates the dedoping of PEDOT:PSS due to the injection of cations from the electrolyte.[37] Except for PtNPs composite that showed a decrease of I_d upon the addition of H_2O_2 regardless of the measurement mode (chemiresistor or OECT), PB and rGO composites exhibited remarkably different response in chemiresistor and OECT modes. As an example, when PEDOT:PSS-PB was tested as a chemiresistor (without gate electrode), I_d increased indicating an increase of the conductivity of the composite, whereas I_d decreased in both OECTs configurations. This may suggest that, despite the incorporation of nanoparticles in the channel, the main response of the sensors is mostly dictated by what happens at the gate electrode. This observation is in agreement with the previous work reported by Berggren and coworkers, in which they tested an OECT featuring PEDOT:PSS/PtNPs composite in the channel and the gate electrode, with and without gate electrode[4]. In their work, they found that the decrease of I_d upon the addition of 0.91 mM of H_2O_2 was 10 times higher with the gate electrode (V_d = -0.2 V and V_g = +0.4 V), compared to the response without gate electrode. On the other hand, the standard OECT that had PEDOT:PSS-PtNPs as gate electrode demonstrated the highest sensitivity with 3.97 mA/dec (Figure 6.6B and Figure 6.6G). Moreover, regardless of the composite tested, the standard OECT performed better than the dual OECT in terms of sensitivity to H_2O_2, as summarized in Table 6.3 and Figure 6.6G.

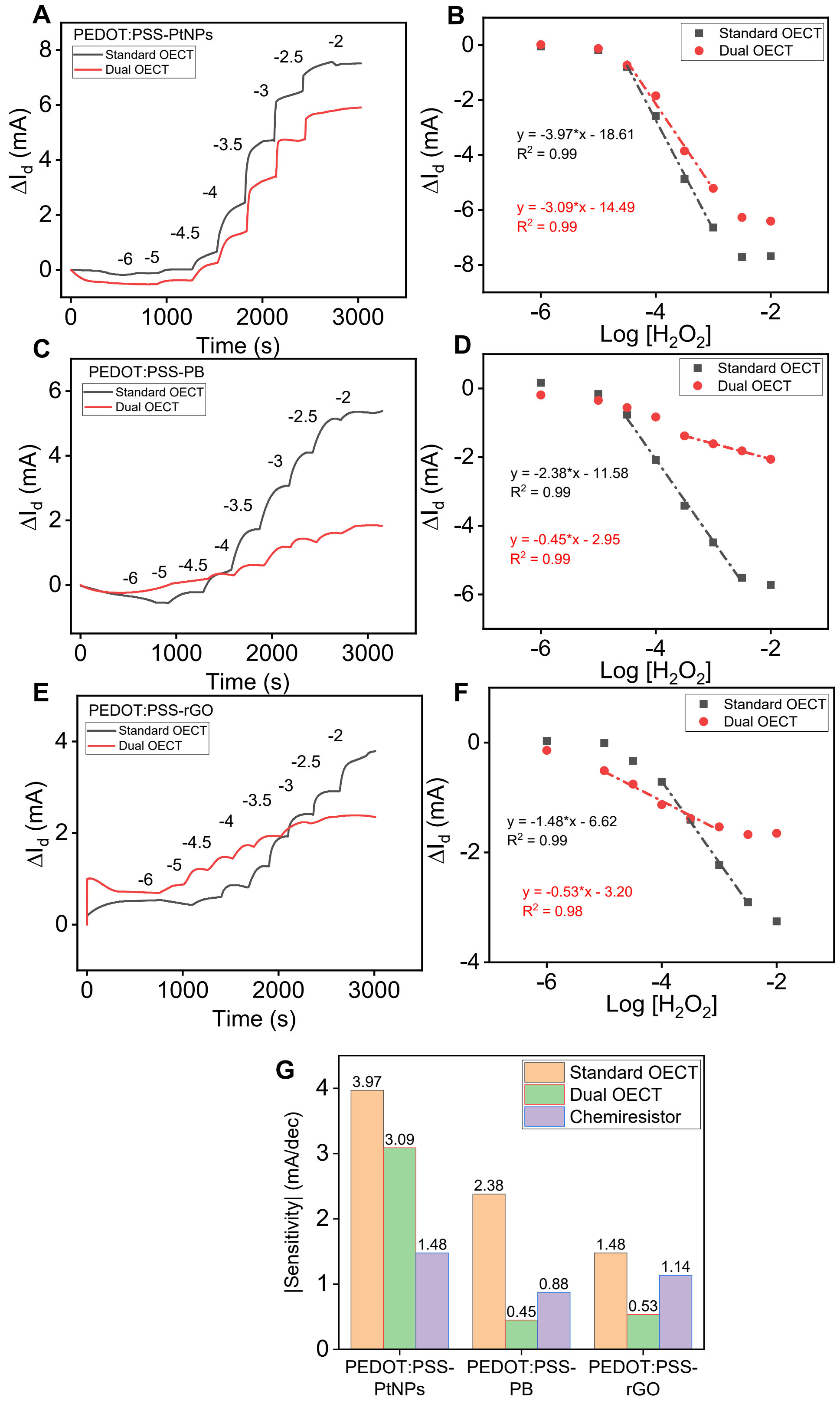
A
PEDOT:PSS-PtNPs
Standard OECT
Dual OECT
-6 -5 -4.5 -4 -3.5 -3 -2.5 -2
ΔId (mA)
0 2 4 6 8
0 1000 2000 3000
Time (s)
B
Standard OECT
Dual OECT
y = -3.97*x - 18.61
R2 = 0.99
y = -3.09*x - 14.49
R2 = 0.99
ΔId (mA)
0 -2 -4 -6 -8
-6 -4 -2
Log [H2O2]
C
PEDOT:PSS-PB
Standard OECT
Dual OECT
-6 -5 -4.5 -4 -3.5 -3 -2.5 -2
ΔId (mA)
0 2 4 6
0 1000 2000 3000
Time (s)
D
Standard OECT
Dual OECT
y = -2.38*x - 11.58
R2 = 0.99
y = -0.45*x - 2.95
R2 = 0.99
ΔId (mA)
0 -2 -4 -6
-6 -4 -2
Log [H2O2]
E
PEDOT:PSS-rGO
Standard OECT
Dual OECT
-6 -5 -4.5 -4 -3.5 -3 -2.5 -2
ΔId (mA)
0 2 4
0 1000 2000 3000
Time (s)
F
Standard OECT
Dual OECT
y = -1.48*x - 6.62
R2 = 0.99
y = -0.53*x - 3.20
R2 = 0.98
ΔId (mA)
0 -2 -4
-6 -4 -2
Log [H2O2]
G
Standard OECT
Dual OECT
Chemiresistor
|Sensitivity| (mA/dec)
0 1 2 3 4
3.97 3.09 1.48
2.38 0.45 0.88
1.48 0.53 1.14
PEDOT:PSS-PtNPs
PEDOT:PSS-PB
PEDOT:PSS-rGO

Figure 6.6. Time trace of ΔI_d for standard and dual OECTs showing the increasing additions of H_2O_2 from -6 to -2, for composites A) PEDOT:PSS-PtNPs, C) PEDOT:PSS-PB, and E) PEDOT:PSS-rGO. B), D), and F) are the corresponding ΔI_d-log[H_2O_2] plots. F) Comparison of the sensitivities of all the OECT.

Table 6.3. Summary of the analytical performance of standard and dual OECTs.

Composite	Standard OECT			Dual OECT		
	|Sensitivity| (mA/dec)	LR	R^2	|Sensitivity| (mA/dec)	LR	R^2
PEDOT:PSS-PtNPs	3.97	-4.5 to -3	0.99	3.09	-4.5 to -3	0.99
PEDOT:PSS-PB	2.38	--4.5 to -2.5	0.99	0.45	-3.5 to -2	0.99
PEDOT:PSS-rGO	1.48	-4 to -2.5	0.99	0.53	-5 to -3	0.98

LR: linear range.

6.4 Conclusions

In conclusion, thick film chemiresistors and OECTs were constructed based on PEDOT:PSS and four nanomaterials, PtNPs, PB, rGO, and ZnO. While ZnO exhibited poor response, the composites featuring PtNPs, PB, and rGO demonstrated good sensitivity over an excellent linear range (-5 to -3) when tested as chemiresistors for the detection of H_2O_2. Two configurations of OECTs were evaluated, standard and dual. In both configurations, PtNPs composite performed way better than PB and rGO, exhibiting 66 % and 168 % increase in sensitivity compared to PB and rGO in standard configuration. However, the nature of the redox reaction at the channel and gate electrode are not well understood, and require further investigation.

6.5 Supporting information

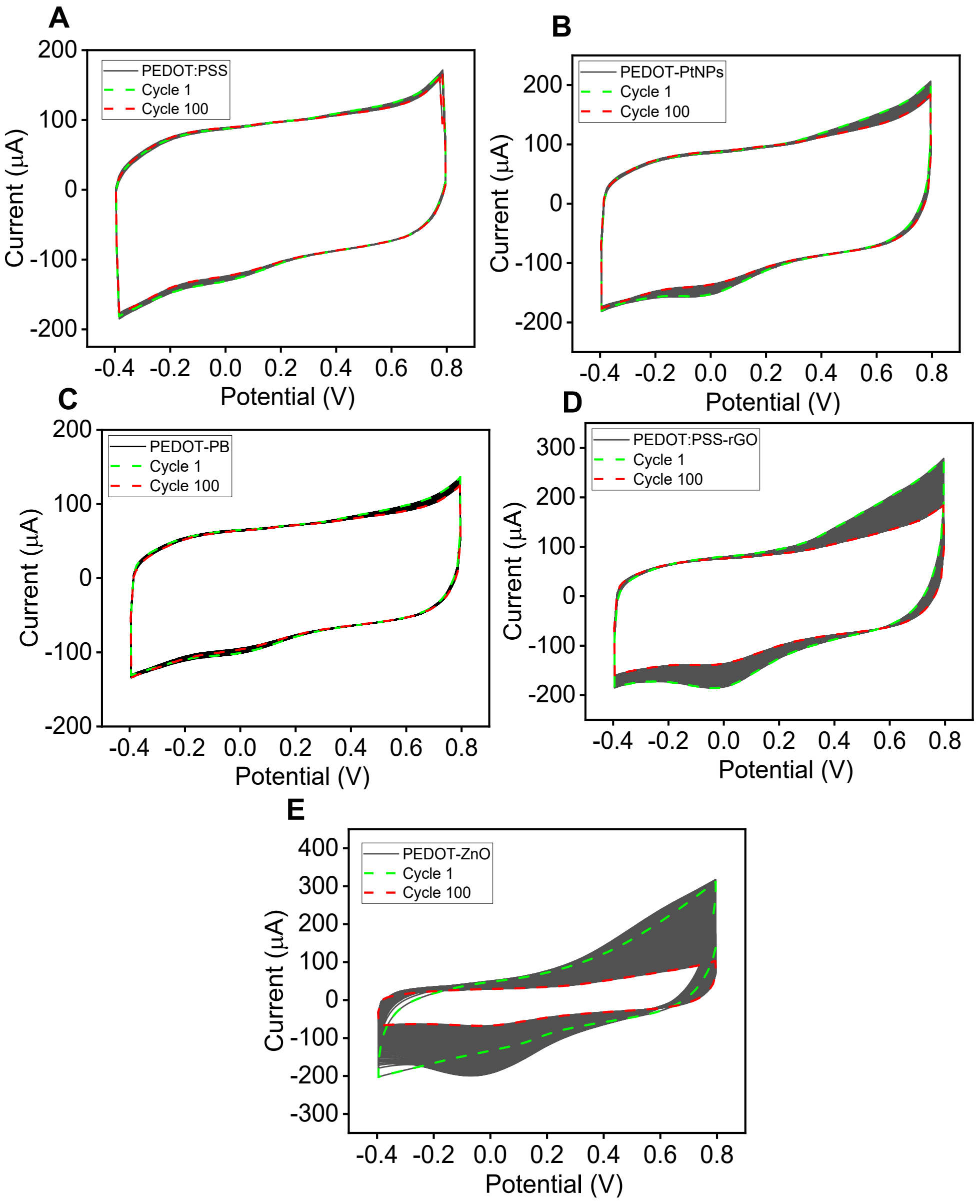

Figure S 6.1. Cyclic voltammograms highlighting the 1st and 100th cycles conducted in NaCl (0.1 M) of A) pristine PEDOT:PSS, B) PEDOT:PSS-PtNPs, C) PEDOT:PSS-PB, D) PEDOT:PSS-rGO, and E) PEDOT:PSS-ZnO.

6.6 References

[1] Yang, J.; Liu, Y.; Liu, S.; et al., *Mater Chem Front*, **2017**, 1, 251-268.

[2] Zhao, Z.; Richardson, G. F.; Meng, Q.; et al., *Nanotechnology*, **2016**, 27, 042001.

[3] Kaur, G.; Adhikari, R.; Cass, P.; et al., *RSC Advances*, **2015**, 5, 37553-37567.

[4] Kergoat, L.; Piro, B.; Simon, D. T.; et al., *Adv Mater*, **2014**, 26, 5658-5664.

[5] Zhang, W.; Ma, D.; Du, J., *Talanta*, **2014**, 120, 362-367.

[6] Vazquez-Gonzalez, M.; Torrente-Rodriguez, R. M.; Kozell, A.; et al., *Nano Lett*, **2017**, 17, 4958-4963.

[7] Yang, T.; Jia, H.; Liu, Z.; et al., *J Electroanal Chem*, **2017**, 799, 625-633.

[8] Goda, E. S.; Lee, S.; Sohail, M.; et al., *Journal of Energy Chemistry*, **2020**, 50, 206-229.

[9] Mousavi Shaegh, S. A.; Nguyen, N.-T.; Mousavi Ehteshami, S. M.; et al., *Energy Environ Sci*, **2012**, 5, 8225.

[10] Lin, M.; Yang, J.; Cho, M.; et al., *Macromol Res*, **2011**, 19, 673-678.

[11] Hurlbutt, K.; Wheeler, S.; Capone, I.; et al., *Joule*, **2018**, 2, 1950-1960.

[12] Miglbauer, E.; Wojcik, P. J.; Glowacki, E. D., *Chem Commun (Camb)*, **2018**, 54, 11873-11876.

[13] Smith, A. T.; LaChance, A. M.; Zeng, S.; et al., *Nano Materials Science*, **2019**, 1, 31-47.

[14] Johnson, D. W.; Dobson, B. P.; Coleman, K. S., *Curr Opin Colloid Interface Sci*, **2015**, 20, 367-382.

[15] Morimoto, N.; Kubo, T.; Nishina, Y., *Sci Rep*, **2016**, 6, 21715.

[16] Shamkhalichenar, H.; Choi, J.-W., *J Electrochem Soc*, **2020**, 167, 037531.

[17] Zhang, R.; Chen, W., *Biosens Bioelectron*, **2017**, 89, 249-268.

[18] Liao, C.; Zhang, M.; Niu, L.; et al., *J Mater Chem B*, **2013**, 1, 3820-3829.

[19] Wang, Y.; Qing, X.; Zhou, Q.; et al., *Biosens Bioelectron*, **2017**, 95, 138-145.

[20] Siddiqi, K. S.; Ur Rahman, A.; Tajuddin; et al., *Nanoscale Res Lett*, **2018**, 13, 141.

[21] Sivalingam, D.; Gopalakrishnan, J. B.; Krishnan, U. M.; et al., *Physica E Low Dimens Syst Nanostruct*, **2011**, 43, 1804-1808.

[22] Abd-Wahab, F.; Abdul Guthoos, H. F.; Wan Salim, W. W. A., *Biosensors (Basel)*, **2019**, 9, 36.

[23] Lee, D. Y.; Na, S. I.; Kim, S. S., *Nanoscale*, **2016**, 8, 1513-1522.

[24] Sygellou, L.; Paterakis, G.; Galiotis, C.; et al., *J Phys Chem C*, **2015**, 120, 281-290.

[25] Volkov, A. V.; Wijeratne, K.; Mitraka, E.; et al., *Adv Funct Mater*, **2017**, 27, 1-10.

[26] Proctor, C. M.; Rivnay, J.; Malliaras, G. G., *J Polym Sci, Part B: Polym Phys*, **2016**, 54, 1433-1436.

[27] Bianchi, M.; Carli, S.; Di Lauro, M.; et al., *J Mater Chem C*, **2020**, 8, 11252-11262.

[28] Ge, Y.; Xie, X.; Roscher, J.; et al., *J Solid State Electrochem*, **2020**, 24, 3215-3230.

[29] Wei, Q.; Mukaida, M.; Naitoh, Y.; et al., *Adv Mater*, **2013**, 25, 2831–2836.

[30] Huang, X.; Deng, L.; Liu, F.; et al., *Energy mater adv*, **2021**, 2021, 1-10.

[31] Evans, S. A.; Elliott, J. M.; Andrews, L. M.; et al., *Anal Chem*, **2002**, 74, 1322-1326.

[32] Hall, S. B.; Khudaish, E. A.; Hart, A. L., *Electrochimica Acta*, **1998**, 43, 2015-2024.

[33] Giaretta, J. E.; Oveissi, F.; Dehghani, F.; et al., *Adv Mater Technol*, **2021**, 6, 1-8.

[34] Karyakin, A. A., *Electroanalysis*, **2001**, 13, 813-819.

[35] Karyakin, A., *Electrochem Commun*, **1999**, 1, 78-82.

[36] Rivnay, J.; Inal, S.; Salleo, A.; et al., *Nat Rev Mater*, **2018**, 3, 1-14.

[37] Friedlein, J. T.; McLeod, R. R.; Rivnay, J., *Org Electron*, **2018**, 63, 398-414.

7 Chemiresistive Sensors Based On PEDOT:PSS/Platinum Nanoparticles Composite For The Detection Of Hydrogen Peroxide And Lactate

Summary

Based on the preliminary and promising results achieved for PEDOT:PSS composites chemiresistors in terms of analytical performance, we decided to focus on PEDOT:PSS-platinum nanoparticles composite. To gain more insight about the performance of the device in practical conditions, the sensor was further characterized and tested for the detection of hydrogen peroxide and lactate in artificial sweat. The characterization and analytical results of the device are presented and discussed.

7.1 Introduction

The recent transformations of healthcare and the proliferation of wellbeing culture has fostered the development of novel technologies that can fulfil the increasing need for personalized point-of-need and point-of-care devices. An essential prerequisite of such devices is their ability to be used independently by patients and users, from sample collection to test execution. For this to happen, it is crucial that the complexity of such devices be kept at minimum without compromising performance. In this regard, unlike OECTs or OFETs, chemiresistors technology is well positioned because it utilizes two-electrode system, which further simplifies the electrochemical cell. This chapter presents a novel chemiresistor for lactate detection based on PEDOT:PSS/platinum nanoparticles. The immobilization of the enzyme lactate oxidase on top of the composite provides the sensor with selectivity and sensitivity to lactate. The electrical, electrochemical, and analytical performance of the device are discussed.

Chemirestsors are two-electrode devices that are usually associated with gas sensing. One of the earliest chemiresistors was originally designed as a gas sensor, wherein the sensing material was made of a metal-oxide semiconductor maintained at high temperatures, which allowed the detection of gases such as CO_2[1]. Over the years, chemiresistors have been utilized in a plethora of applications including environmental[2], food[3], and biochemical sensing[4], as a single device or in arrays[5]. Eventually, these devices have found their route to bio- and chemical sensing in aqueous solutions[6]. Chemiresistors are now regarded as a subgroup of (bio) chemical sensors in which the resistance of a sensitive material is monitored, while the material is kept in direct contact with the analyte of interest[7]. The sensing material is a conductive thin film deposited between two metallic electrodes that are separated by a small gap. What makes chemiresistors an excellent candidate for building biosensing platforms is their simple design, facile fabrication, and high signal-to-noise[8]. Unlike traditional electrochemical methods, e.g. amperometry and potentiometry[9, 10], chemiresistors do not require a reference electrode, reducing further the complexity of data acquisition and processing steps. Furthermore, their ease of integration and miniaturization have made them suitable for building point-of-care devices[11], wearable sensors[12], and smart patches[13]. PEDOT:PSS composites are highly relevant in this context because not only endow chemiresistors with the required conductivity, but also with selectivity to a wide range of analytes[14, 15].

On the other hand, PEDOT:PSS composites are novel materials created to fulfil specific technical needs by combining the organic conductive polymer poly(3,4-ethylenedioxythiophene) polystyrene sulfonate (PEDOT:PSS), nanomaterials, polyelectrolytes, and/or biomolecules. In addition to the excellent electrical properties of this conductive polymer, its composites can be designed by incorporating nanomaterials that bring unique features, such as piezoelectric[16], magnetic[17], catalytic[18], and thermoelectric properties[19]. For this reason, nanomaterials are central to PEDOT:PSS composites, since they expand the capabilities of the conductive polymer beyond the electrical conductivity. Over the last decade, PEDOT:PSS composites have been widely studied in numerous research areas, including energy storage, fuel cells[20], solar cells[21], thermoelectric[19], electrochromic[22], and biosensors[23].

PEDOT:PSS is the most common conductive polymer (known also as organic semiconductive polymer) owing to his high conductivity, solution processability, commercial availability, and pH stability. The conductive polymer can be casted or electropolymerized from different solvents, and still maintains good conductivity after drying, which makes it miscible with nanomaterials suspensions. This compatibility with other solvents is essential, because it ensures a uniform dispersion of nanoparticles within the PEDOT:PSS matrix and reproducible morphology of thin films. For this reason, PEDOT:PSS composites thin films can be prepared also by either mixing the conductive polymer with nanomaterials in suspension, or by successive/simultaneous electropolymerization and electrodeposition of the conducting polymer and nanomaterials, respectively. Moreover, the composites can be processed using a wide range of methods; from the simplest (e.g drop-cast, spin coating), to the most sophisticated (e.g. photolithography and inkjet printing).

PEDOT:PSS composites are also biocompatible, as such, they can be combined with biomolecules to build multifunctional biosensors able to detect specific analytes[24, 25]. The versatility of these composites have encouraged their incorporation in different transducing schemes, including amperometric, potentiometric, and to less extent chemiresistors.

Several works in the literature have successfully reported the use of conductive polymer composites for building H_2O_2 chemiresistive biosensors. For instance, Giaretta et al. have demonstrated a chemiresistor wherein the channels was comprised of PEDOT:PSS/horseradish composite, printed on paper substrate and employed as hydrogen peroxide sensor[26]. In their work, they attributed the decrease of the resistance measured upon the addition of H_2O_2 to the oxidation of PEDOT:PSS and the creation of the highly conductive bipolarons species. Song et al. have successfully built a glucose chemiresistive sensor by inkjet printing, utilizing polyaniline fibers and platinum nanoparticles composite[4]. Despite these efforts, there is still a lack of chemiresistive biosensors that incorporate PEDOT:PSS based composites that enable the detection of biomolecules in aqueous solutions. In this work, chemiresistive-based sensors were demonstrated by combining the excellent conductivity of PEDOT:PSS, the catalytic activity of PtNPs, and the specificity of biomolecules. The composite, comprised of the conducting polymer poly(3,4-ethylenedioxythiophene) doped with polystyrene sulfonate (PEDOT:PSS), was decorated with platinum nanoparticles (PtNPs) and deposited via drop-casting. The sensors can be incorporated in a platform for building affordable Point-of-Need devices.

7.2 Results and discussion

7.2.1 Working principle of the chemiresistor

The working mechanism of the PEDOT:PSS/PtNPs chemiresistor described in Figure 7.1B can be rationalized in terms of the catalytic activity of PtNPs, the redox state of PEDOT:PSS, and the properties of PEDOT:PSS/PtNPs interface. The electrical conductivity of PEDOT:PSS is directly related to the mobility and concentration of charge carriers along the conjugated backbone of the polymer. Within the framework of solid-state physics, PEDOT:PSS is widely considered as p-type organic semicoducting material where the charge carriers are positive holes. The ability of these holes to move along the polymer chain (and/or hope from one chain to another) without disturbance, and the stability offered by the negatively charged PSS, dictate the redox state of the conducting polymer, thus its conductivity.

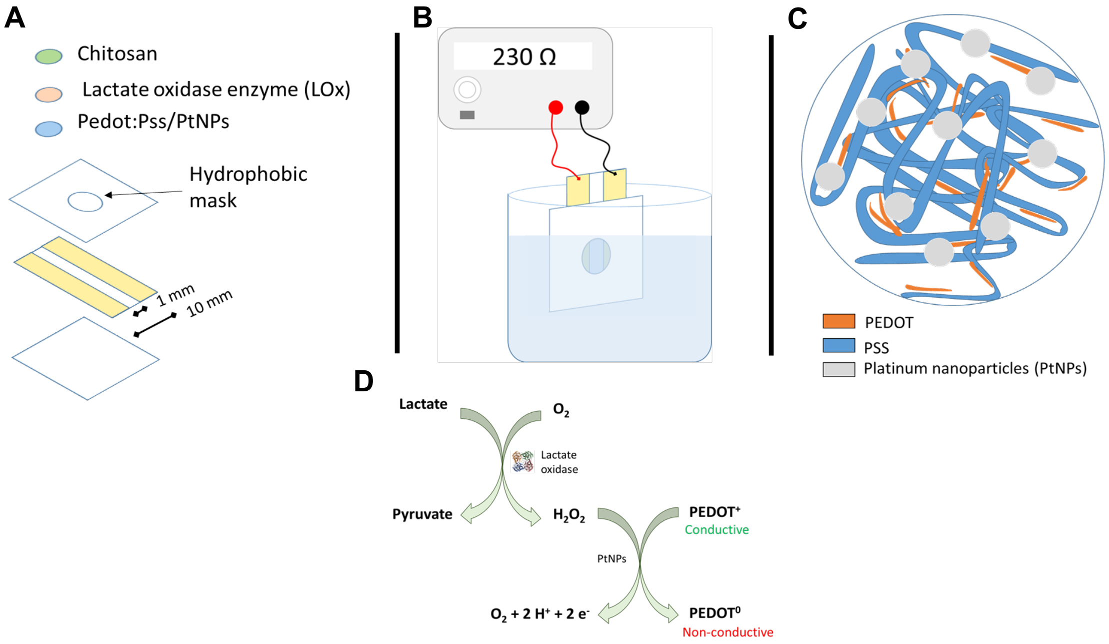

Figure 7.1. A) Construction of the chemiresistor. B) Measurement setup. C) Illustration of the PEDOT:PSS/PtNPs composite structure. D) Detection mechanism of the sensor.

In the PEDOT:PSS/PtNPs composite, the nanoparticles are anchored at different locations along the PEDOT and PSS chains. This uniform distribution of nanoparticles in the PEDOT:PSS matrix results in a PEDOT:PSS/PtNPs interface with high specific area. To illustrate this point, assuming 1 µg of PtNPs with spherical shape and radius of 3 nm, ideally, the maximum total area of the PEDOT:PSS/PtNPs interface can be approximated by the total surface area of all nanoparticles. In this case, the area of the interface would be 0.47 cm^2. Therefore, an electrochemical event nearby has a great chance to disturb the mobility of charge carriers over a large area, especially if it occurs simultaneously over different locations along the PEDOT:PSS chains.

It should always be considered that PEDOT has a redox equilibrium between the oxidized (conductive) and reduced (non-conductive) form. This reversible process is responsible for the changes in the channel electrical conductivity triggered by chemical changes. Most of the applications explored so far in the literature are based on charge-mediated change of the redox state, i.e., using the migration of cations to alter the redox balance. Alternative mechanism to change the equilibrium of PEDOT are less common. Redox reactions should be thermodynamically and kinetically favourable. To overcome some of these issues, it should be possible to use sensitizing species that can act as mediators, targeting specific substances and enabling the redox transition of the conductive polymer. This is the idea behind the introduction of Pt nanoparticles: developing a detection approach that takes advantage of the reactivity of the $Pt\text{-}H_2O_2$ system and affects the conductivity of PEDOT.

Consequently, as we have seen in Chapter 6, the response of PEDOT:PSS to the change in the charge carriers mobility is an increase or decrease of its electrical conductivity. Similarly, when the hydrogen peroxide undergoes a redox reaction at the surface of platinum nanoparticles, the $PEDOT^+:PSS^-$ synergy is altered , leading to a decrease in the conductivity of PEDOT:PSS.

7.2.2 Microscopic characterization of the composite

Dispersion of PtNPs in PEDOT:PSS

One of the challenge in the preparation of polymer-nanoparticles composites is to obtain thin-films with reproducible and consistent properties. The degree of dispersion of nanoparticles within the PEDOT:PSS matrix is known to have a significant impact on the mechanical properties of the films and the analytical performance of the sensor. Therefore, it is essential that the nanoparticles have a uniform size and be homogeneously dispersed in the PEDOT:PSS matrix, with minimum agglomerates.

Figure 7.2A-C show TEM images of PtNPs in three PEDOT:PSS/PtNPs composites which have platinum loading of 0.1 mg/mL, 0.5 mg/mL, and 2 mg/mL. The images show that PtNPs are well dispersed within the PEDOT:PSS for 0.1 mg/mL and 0.5 mg/mL, ensuring an enhanced polymer-nanoparticles interface. However, large islands of nanoparticles that are challenging to reproduce are formed when the concentration is increased to 2 mg/mL. In addition, the diameter of PtNPs estimated from TEM pictures is about 2.34 ± 0.89 nm[27], which is the typical size obtained when PtNPs are stabilized with triphenylphosphine[28].

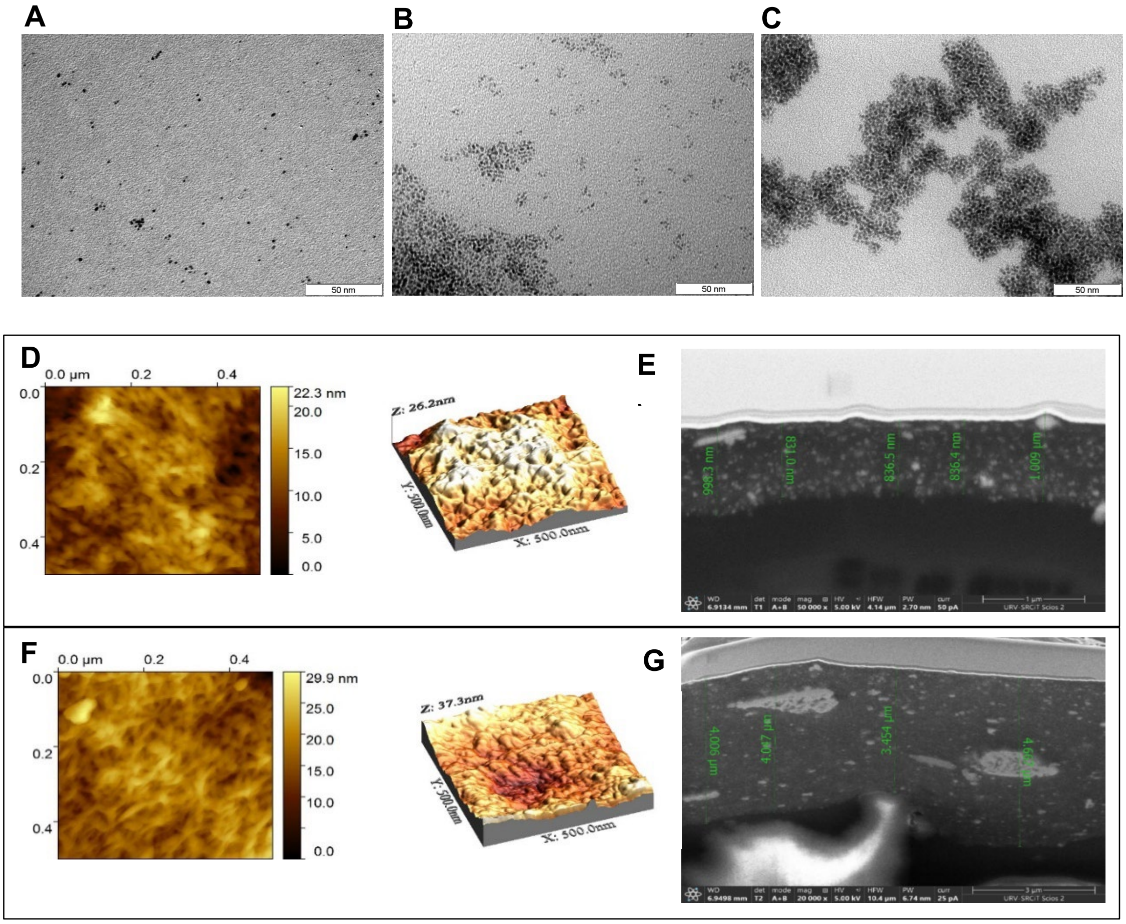

Figure 7.2. TEM images of PtNPs in three composites which have 0.1 % of PEDOT:PSS, but different concentrations of PtNPs A) 0.1 mg/mL, B) 0.5 mg/mL, and C) 2 mg/mL. D) AFM morphology of a composite with 0.1 % of PEDOT:PSS and 0.5 mg/mL PtNPs . E) the corresponding FESEM cross-section. F) AFM morphology of PEDOT:PSS-PtNPs 1 %, 0.5 mg/mL, and G) the corresponding FESEM cross-section.

Morphology of the PEDOT>PSS/PtNPs composite

The morphology and thickness of the PEDOT:PSS/PtNPs composite film depends on the PtNPs loading and the concentration of the polymer. To check this relationship, we analyzed the morphology and thickness of two PEDOT:PSS-PtNPS composites that have the same loading of PtNPs, but different concentrations of PEDOT:PSS, 0.1 %, 1 %, respectively. Figure 7.2D and Figure 7.2F display the morphology of the two composite films, characterized by AFM over an area of 500 nm x 500 nm. The maximum heights recorded were 26.2 nm, 37.3 nm for the composite tested, which suggests that the surface of the channels is very smooth. This is important because roughness of PEDOT:PSS films depends on the substrate material used, and it has been reported that high roughness affects the morphology of the film and increases its sheet resistance[29].

Therefore, the surface of the composite films constructed by drop casting method can be considered as relatively rough on the nanoscale and smooth on the microscale. This is important, particularly for paper substrates coated with PEDOT:PSS.

Furthermore, cross-sections of the aforementioned composite films were acquired via FESEM. The images presented in Figure 7.2E and Figure 7.2G demonstrate clearly the dispersion of the nanoparticles within the conducting polymer matrix. The nature of the nanoparticles were also confirmed to be platinum, as can be seen in the EDX data (Figure S 7.1, Supporting Information). In addition, the thickness of the composite films was estimated from the cross-sections and was 4.0 ± 0.3 µm and 0.9 ± 0.1 µm (calculated by taking the average and the standard deviation of four measures at 3 different locations).

7.2.3 Electrochemical characterization

The electrochemical properties of the composite were studied by cyclic voltammetry, electrochemical impedance spectroscopy, and chronoamperometry. Figure 7.3A shows the CV curves obtained for bare platinum, PEDOT:PSS, and PEDOT:PSS/PtNPs in PBS (0.1 M). The voltammogram of the platinum electrode tested did not show any observable peaks, however, it is notable that the current increased rapidly when the potential applied was scanned towards high negative potentials (from -0.6 to -0.8 V vs Ag/AgCl). This abrupt increase of the current could be ascribed to the hydrogen evolution reaction. In contrast, the CV profile of pristine PEDOT:PSS and PEDOT:PSS/PtNPs composite in PBS displayed a large rectangular-like shape, indicative of the capacitance behaviour of the conductive polymer.

Moreover, when tested in the presence of ferri/ferrocyanide $[Fe(CN)_6]^{3-/4-}$, PEDOT:PSS and PEDOT:PSS/PtNPs showed well-defined anodic and cathodic peaks related to the reduction and the oxidation of the redox mediator at 0.15 V and 0.32 V, respectively. The two peaks point to the excellent electron transfer capabilities of PEDOT:PSS. However, the peak-to-peak separation for both PEDOT:PSS and the PEDOT:PSS/PtNPs composite ($\Delta E \approx 150$ mV) is more than twice larger than the ideal value of 59 mV, indicating an irreversible process.

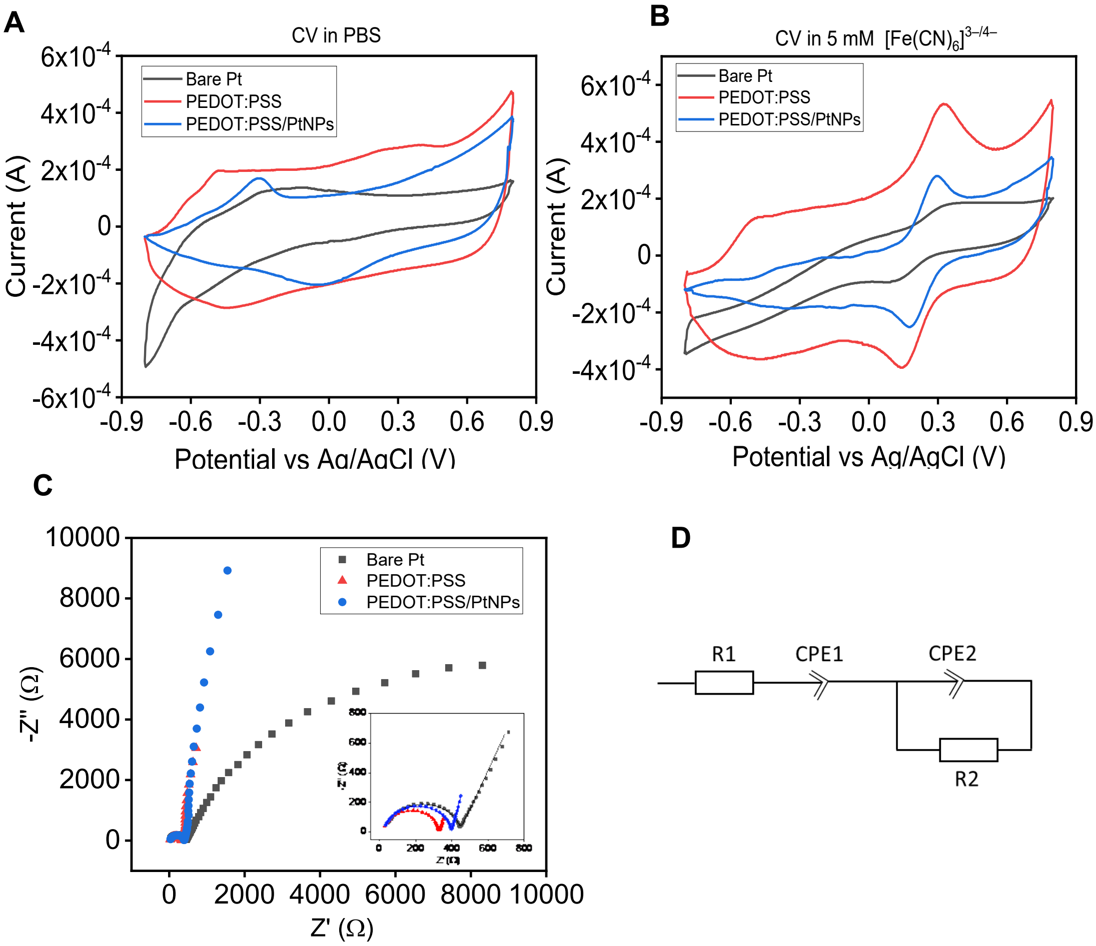

Figure 7.3. Cyclic voltammograms obtained for PEDOT:PSS/PtNPs (0.1 %, 0.5 mg/mL) in A) 0.1 M PBS, and, B) 0.1 M OBS + 5 mL potassium ferri/ferrocynide. C) EIS spectra of the same composite in PBS, with inset graph showing the fitting of the experimental data using a simple randles circuit illustrated in D).

Furthermore, Figure S 7.2 (See S.I) presents the CV curves of PEDOT:PSS/PtNPs at different scan rates ranging from 50 mV/s to 500 mV/s. It is worth noting that the anodic and cathodic current increased significantly with the increasing scan rate. In addition, the plot of the peak current versus the square root of the scan rate demonstrated a linear relationship, which indicates that the redox reaction of $[Fe(CN)_6]^{3-}/^{4-}$ at the surface of the composite takes place according to a diffusion limited process[30].

On the other hand, the PEDOT:PSS/PtNPs composite was drop cast using a gold electrode as substrate, then tested by adding 1 mM of H_2O_2 (in PBS 0.1 M) via amperometry, in a three-electrode setup (Figure S 7.4, see S.I). Upon the addition of 1 mM of H_2O_2, the sensor showed an increase in the current that depends on the voltage applied. For instance, at 0 V vs Ag/AgCl, the current recorded was 7 μA, while at -0.3 V the current increased to about 14 µA. Ultra-small PtNPs were reported to demonstrate an excellent sensitivity toward hydrogen peroxide due to their enhanced catalytic properties.[31] These results corroborate with other works in the literature that have also reported amperometric detection of H_2O_2 utilizing PEDOT:PSS-PtNPs based composites with sensitivities in the range of few nA.µM^{-1}.mm^{-2}.[32, 33]

EIS

To have a closer look at the composite/electrolyte interface, we conducted an EIS analysis in a three electrodes setup. Figure 7.3C shows the Nyquist plot of Pt, PEDOT:PSS and PEDOT:PSS/PtNPs, featuring the plot of the real part against (Z´) the imaginary part (Z”) of the impedance, covering the frequency range 0.1 Hz-105 Hz. At high frequencies, the plot (inset graph) demonstrated well-defined semicircles for the composite and its constituents PEDOT:PSS and Pt. Conversely, the diffusional-controlled region varied significantly for PEDOT:PSS and PEDOT:PSS/PtNPs samples on one hand, and the platinum on the other hand. These results show that, despite the addition of platinum nanoparticles, the composite maintained its diffusion properties PEDOT:PSS. This effect is also observed for PEDOT:PSS/carbon nanotubes composite, where the shape of EIS response was preserved when PEDOT:PSS was tested with and without carbon nanotubes[34]. The Nyquist plots were perfectly fitted with a simple Randles circuit comprising a resistor R1 in series with a constant phase elements CPE1, and a resistor R2 in parallel with a constant phase elements CPE2 (Figure 7.3D). The parameters of the circuit are summarized in Table 7.1.

Table 7.1. Summary of the parameters calculated from Randles circuit.

Substrate	**R1 (Ω)**	**CPE1 ($F.s^{a1-1}$)**	**a1**	**R2 (Ω)**	**CPE2 ($F.s^{a2-1}$)**	**a2**
Bare Pt	32.69	9.2E-05	0.77	410.00	7.14E-08	0.93
PEDOT:PSS	20.60	6.3E-04	0.83	308.40	8.34E-08	0.95
PEDOT:PSS/PtNPs	25.41	1.9E-04	0.87	371.90	6.89E-08	0.95

7.2.4 Electrical characterization

Resistance of the channel

The stability over time of the PEDOT:PSS/PtNPs composite chemiresistor was examined by measuring the resistance of three devices exposed to air, daily during one week. After each measurement, the devices were stored at room temperature (25 °C). Figure 7.4A shows that the resistance slightly increased with time to stabilize in the seventh day. The average resistance of the three channels in Day 1 was 218.3 ± 14.9 Ω, by the seventh day, the average resistance increased to 221.3± 14.6 Ω. This change could be attributed to the slight degradation of the conductivity of PEDOT:PSS.

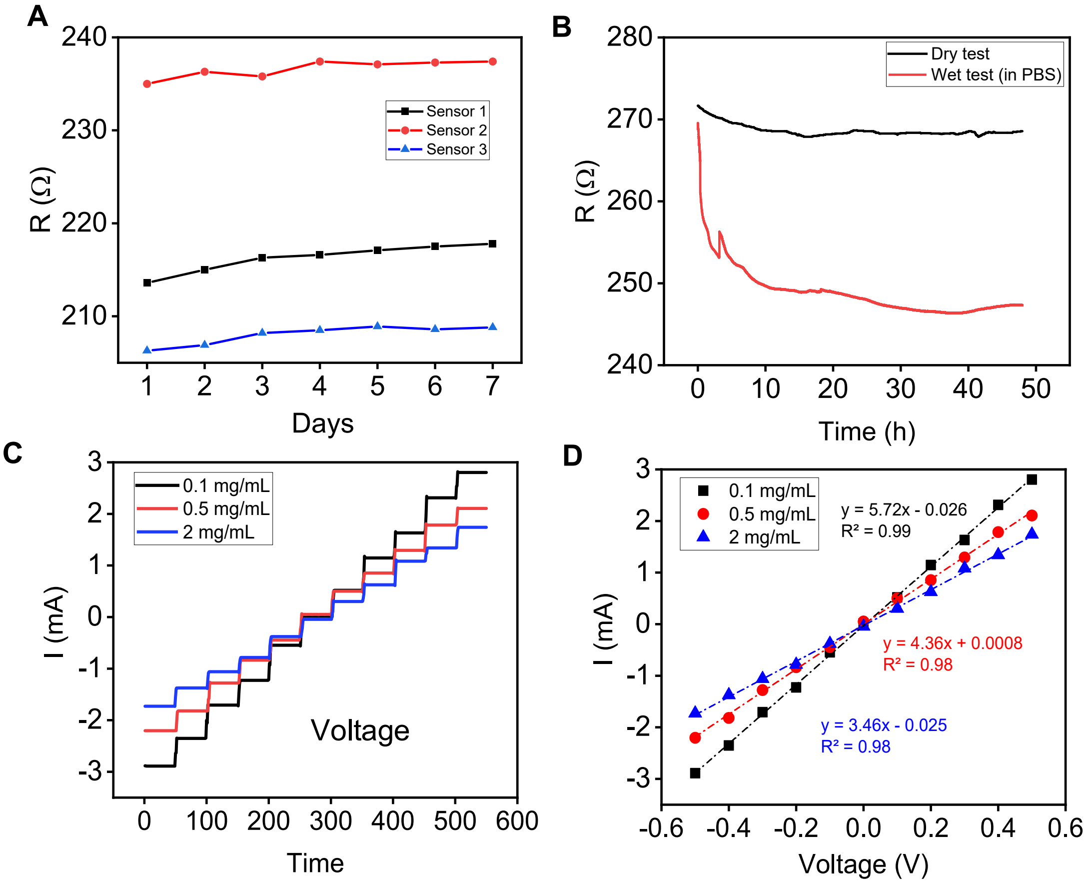

Figure 7.4. A) Time trace of the resistance of three chemiresistors over a period of seven days. B Recording of the resistance during 48h, showing the drift of the resistance in PBS (0.1M), and in air. C-D) I-V output curves for three composites that have 0.1 % PPEDOT:PSS, but different PtNPs loading.

The drift of the device was also measured by monitoring the resistance of a fresh PEDOT:PSS/PtNPs channel during 48 h, in dry and wet conditions (PBS 0.1 M).

In dry conditions, the device showed a resistance drift of 0.06 Ω/h. Conversely, in wet conditions, the chemiresistor displayed a drift of 0.46 Ω/h, which is about 8 times the drift observed in dry conditions and inevitably leads to a change in the baseline of the sensor. This drift is attributed to the interaction of the electrolyte solution with PEDOT:PSS and PtNPs, and could be interpreted as the result of a capacitance effect that rises when the composite is immersed in solution. This capacitance has two components; volumetric capacitance due to the swelling of the conductive polymer film, and the high electrical double layer capacitance (EDL) that develops on the surface of PtNPs. Therefore, the time required for the resistance to stabilize reflects the time needed for an equilibrium-like state to be established.

I-V output

To check whether the amount of PtNPs affects the ohmic behavior of the chemiresistors, we established the output curve I-V for three PEDOT:PSS/PtNPs composites that have different loading in PtNPs. Figure 7.4C-D show the I-V output of a PEDOT:PSS/PtNPs chemiresistors measured in air, and the corresponding response time for voltage step of 0.1 V from -0.5 V to 0.5 V. As can be noted from the correlation coefficients, the three chemiresistors maintained an excellent ohmic behaviour, despite the relatively high loading of PtNPs. This could be explained by the well dispersion of nanoparticles within the matrix, which ensures uniform properties of the composites.

7.2.5 Detection of hydrogen peroxide

For the detection of hydrogen peroxide and lactate, the PEDOT:PSS/PtNPs composite comprised of 0.1 % PEDOT:PSS, and PtNPs 0.5 mg/mL was selected, as it showed an excellent homogeneity and afforded reproducible results. Therefore, unless indicated otherwise, the subsequent tests were carried out using this composite formulation.

For the detection of hydrogen peroxide, the response of three sensors was measured in PBS, as represented in Figure 7.5A. The addition of hydrogen peroxide induced an increase in the resistance of the composite. This increase correlates well with the logarithm of the concentration of H_2O_2 (Figure 7.5B). The sensors displayed a linear response from 10 μM to 1000 μM, and a sensitivity of 15 ± 0.2 Ω/dec (N = 3).

Effect of the Voltage applied on sensitivity of H_2O_2

The measurement of the resistance R utilizes Ohms Law (V = R x I), where a constant current I is applied and the corresponding voltage V is measured. The ratio of the voltage and the current allows the accurate measure of the resistance. Alternatively, chemiresistors can be operated equally by applying a constant voltage between the two electrodes of the device while measuring the electrical current. Figure S 7.6 (S.I) shows the response of the chemiresistor to H_2O_2 at different voltages from -0.1 V to -0.5 V. Interestingly, as represented in Figure 7.5E), the sensitivity of the sensor increased with the voltage applied. This increase of the sensitivity to H_2O_2 could be attributed to the enhancement of the catalytic activity of platinum nanoparticles when they are subjected to an external electrical field. Moreover, regardless of the voltage applied, the same trend is observed, that is, the decrease of the current recoded upon the addition of H_2O_2, which is in agreement with the drop of the resistance observed in the previous section.

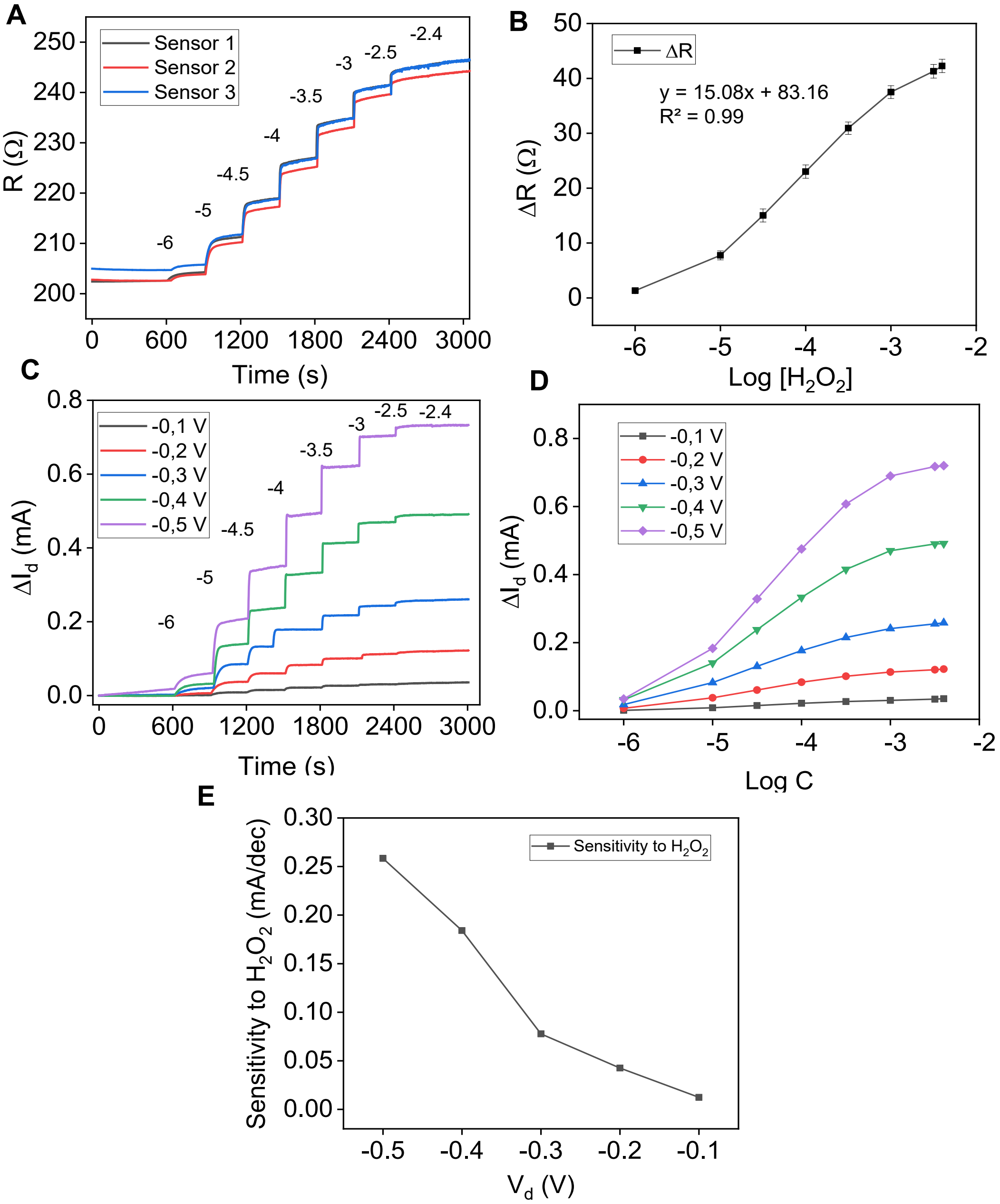

Figure 7.5. A) PEDOT:PSS/PtNPs chemiresistor. Plot of the resistance R vs time of three sensors showing the additions of hydrogen peroxide in PBS (01 M), indicated by the logarithm of the concentration, and B) corresponding calibration curve featuring the average response (N=3). C) ΔI-time plot showing the response of the chemiresistor to H_2O_2 for different voltages applied between -0.1 V and -0.5 V. D) Plot of ΔI versus the

logarithm of the concentration of H_2O_2 at different drain voltages. E) Sensitivity to H_2O_2 as function of the drain voltage.

7.2.6 Detection of L-lactate

Figure 7.6A and Figure 7.6B represent the response to L-lactate from 10^{-3} mM to 3 mM, recorded for a PEDOT:PSS/PtNPs chemiresistor coated with lactate oxidase and immobilized with chitosan, in a 5 mL cell and in a droplet of 10 µL, respectively. As noted for H_2O_2, the resistance of the device increased as L-lactate is added. The LOx entrapped in chitosan catalyzes the oxidation of L-lactate to pyruvate and hydrogen peroxide, as illustrated in Figure 7.1E.

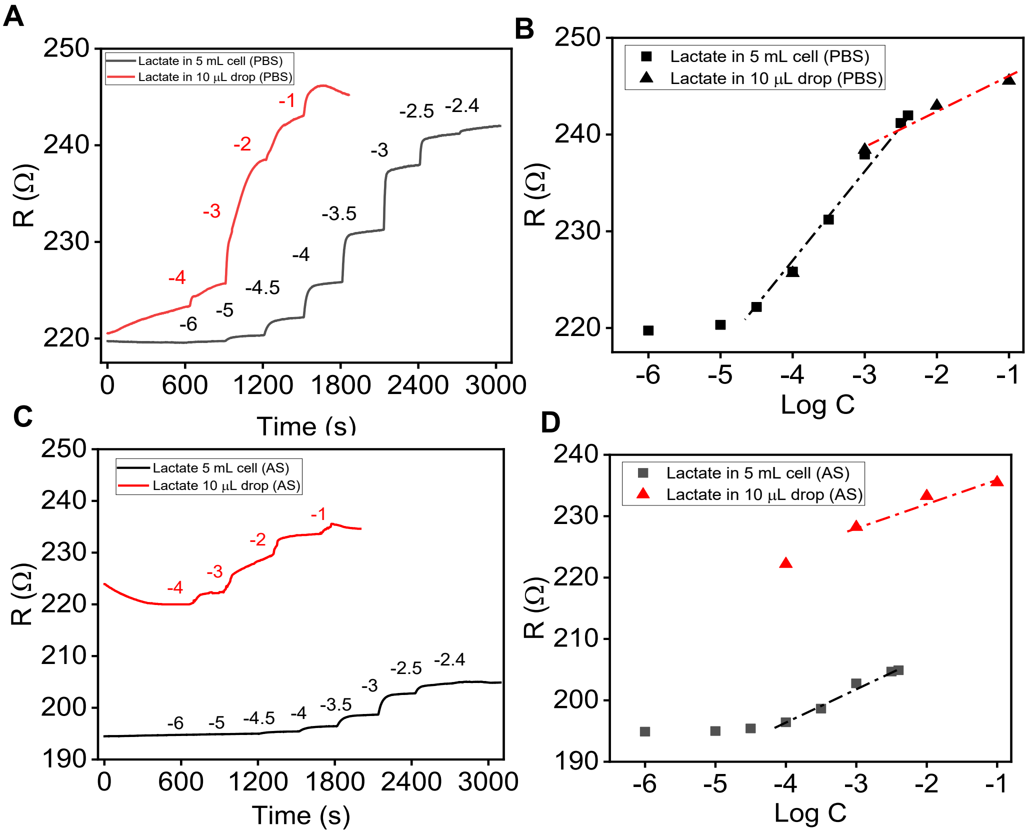

Figure 7.6. A) Time trace of the resistance recorded in PBS for a chemiresistor upon the addition of L-lactate in a 5 mL cell, and in 10 µL droplet, B) corresponding plot of the resistance against the logarithm of the concentration of L-lactate. C) Time trace featuring the response of a chemiresistors to lactate in artificial sweat (AS) in 5 mL cell and 10 µL.

The hydrogen peroxide generated reacts on the surface of PtNPs imbedded in PEDOT:PSS. The nature of the reactions involved is complex, since it depends on the surface composition and charge. On the pristine Pt atoms peroxide is adsorbed and blocks the oxygen reduction reaction. On PtO sites it and undergoes an oxidation reaction. This reaction changes the PtNP potential, modulating the redox balance of the PEDOT:PSS, which is observed as a change in the overall conductivity of composite.

The response of the sensor in the 5 mL cell was carried with steering, which ensures that the enzyme is continuously supplied with L-lactate. As a result, the catalyzed oxidation of L-lactate continues until the saturation is reached at $10^{-2.5}$ M. Conversely, in the 10 µL this process relies solely on the diffusion of L-lactate. Therefore, the profile of the response obtained could be explained-at least in part-as due to a limitation on the supply of the substrate to the enzyme.

In addition, the volume of the LOx deposited can be optimized to achieve higher sensitivities. Figure 7.6A and Figure 7.6C display the R-time curves, as L-lactate was added from 10^{-6} M to $3x10^{-3}$ M, for three chemiresistors that were prepared with an increasing volume of LOx, 5 µL, 10 µL, and 15 µL, in different media (0.1 M PBS, and artificial sweat). As can be seen, the response of the sensors increased with the volume of LOx deposited, since more enzymes are available to catalyze the oxidation of lactate. For example, the sensitivity of the sensor was 10Ω/dec for a sensor prepared with LOx volume of 5 µL, whereas. For a volume of 15 µL, the sensitivity increase five folds to reach 51.13 Ω/dec.

Furthermore, PEDOT:PSS/PtNPs chemiresistor prepared without enzyme was also tested for L-lactate. The response of the sensor, represented in Figure 7.6F, shows that upon the addition of lactate, no change in the resistance was observed, indicating that the sensitivity to L-lactate is attributed to the presence of the LOx enzyme.

The measurement of the resistance can be conducted via 2-point method, as performed so far, or by 4-point method where the circuit utilized to apply the constant current is different from the one utilized for measuring the voltage drop. The latter method eliminates any contact resistance that may arise between the metallic leads and the electrodes. Figure S 7.5 shows a comparison between two calibration curves of lactate. The first was obtained via 2-point method, and the second was obtained by 4-point method. In terms of analytical performance, the sensors showed similar sensitivity and linear range, indicating that the contact resistance has a minor effect on the performance of the sensor.

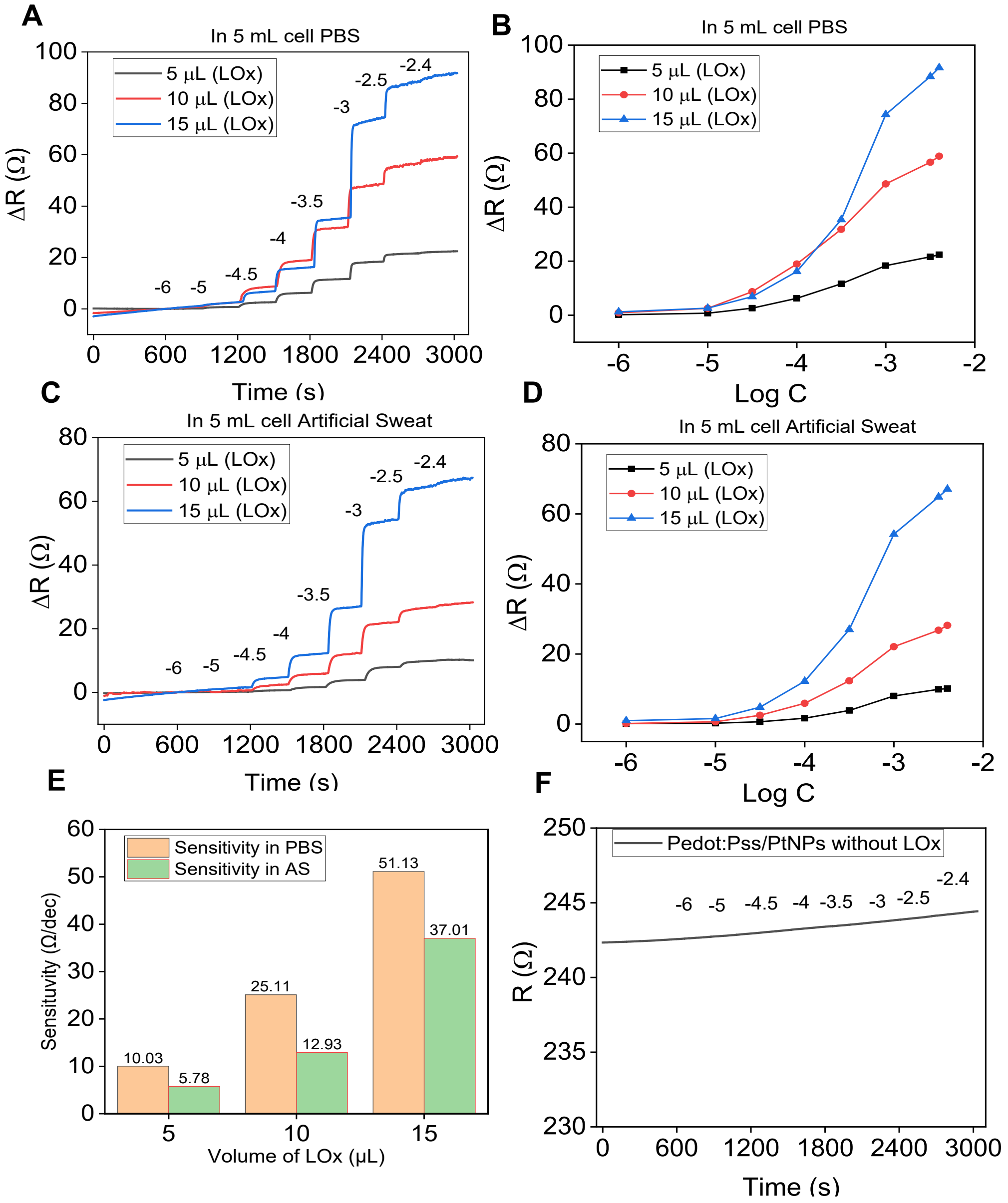

Figure 7.7. Time trace of ΔR featuring the L-lactate response of chemiresistors that were prepared with different volumes of LOx enzyme and tested in A) PBS (0.1 M) and C) artificial sweat. Corresponding calibration curves showing the resistance change plotted against the logarithm of L-lactate concentration in B) PBS (0.1 M) and D) artificial sweat. E) Sensitivity of the sensors to L-lactate versus the volume of LOx enzyme in PBS and artificial sweat (AS). F) Time trace of a chemiresistors prepared without LOx enzyme, showing no response to additions of L-lactate.

7.3 Conclusions

In conclusion, we have demonstrated a chemiresistor sensor based on PEDOT:PSS/PtNPs composite for the detection of hydrogen peroxide, and lactate in artificial sweat. The composite was processed by a simple and rapid method, and showed a well dispersed nanoparticles within the PEDOT:PSS matrix. The chemiresistor demonstrated an ohmic behavior with an excellent stability in air and in wet conditions. The chemiresistor could be equally operated in resistance or current configuration, which provides an additional degree of freedom for integrating the sensor for optimal performance. Moreover, the sensor showed an excellent sensitivity for hydrogen peroxide and lactate in 10 µL droplet in artificial sweat, which makes it suitable for point-of-need.

7.4 Supporting information

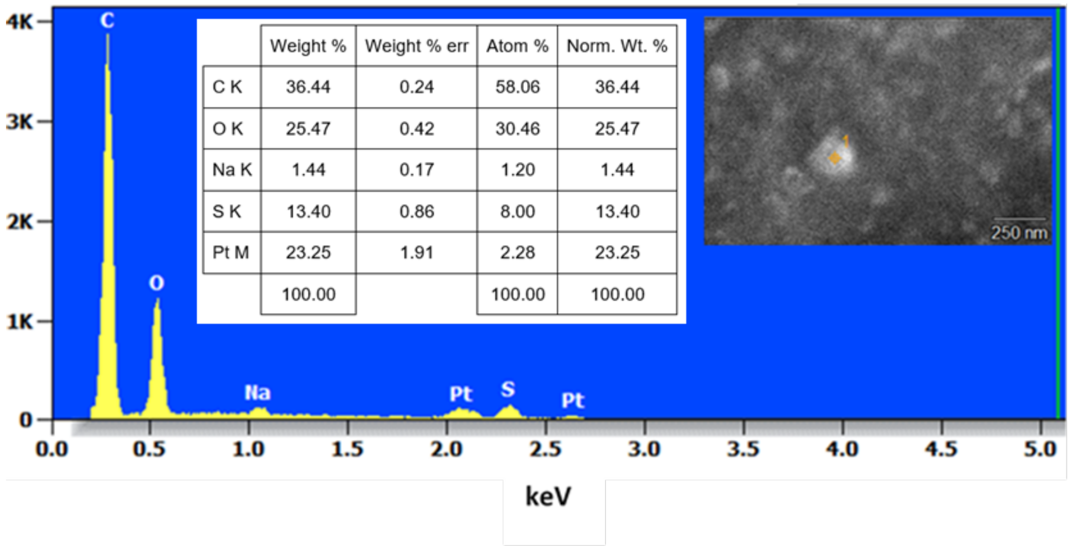

	Weight %	Weight % err	Atom %	Norm. Wt. %
C K	36.44	0.24	58.06	36.44
O K	25.47	0.42	30.46	25.47
Na K	1.44	0.17	1.20	1.44
S K	13.40	0.86	8.00	13.40
Pt M	23.25	1.91	2.28	23.25
	100.00		100.00	100.00

Figure S 7.1. EDX spectra of PEDOT:PSS/PtNP composite comprising PEDOT 0.1 %, and PtNPs 0.5 mg/mL.

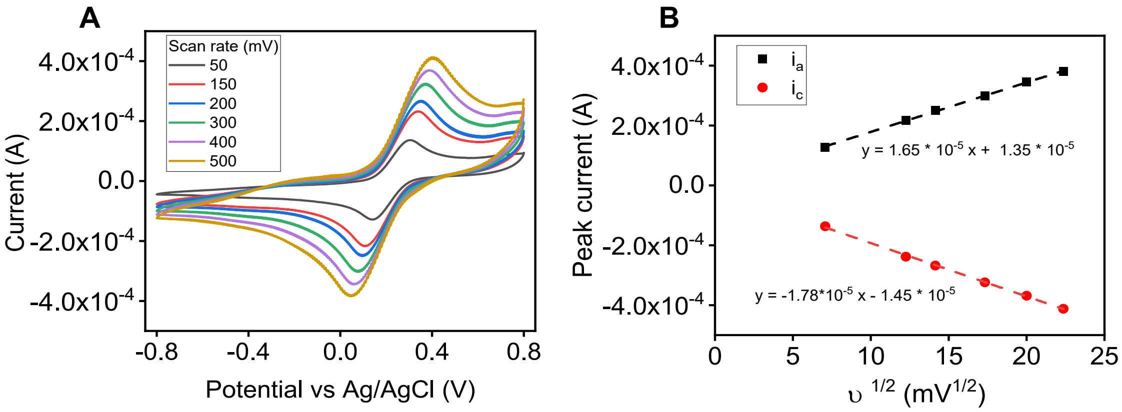

Figure S 7.2. A) Cyclic voltammetry of PEDOT:PSS/PtNPs at different voltage scan rates, B) plot of current peak against the square root of the scan rate.

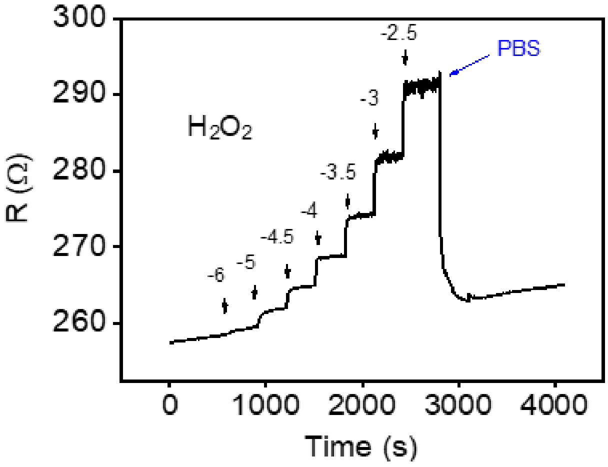

Figure S 7.3. Response of PEDOT:PSS/PtNPs chemiresistor to H_2O_2, showing the baseline after washing with PBS.

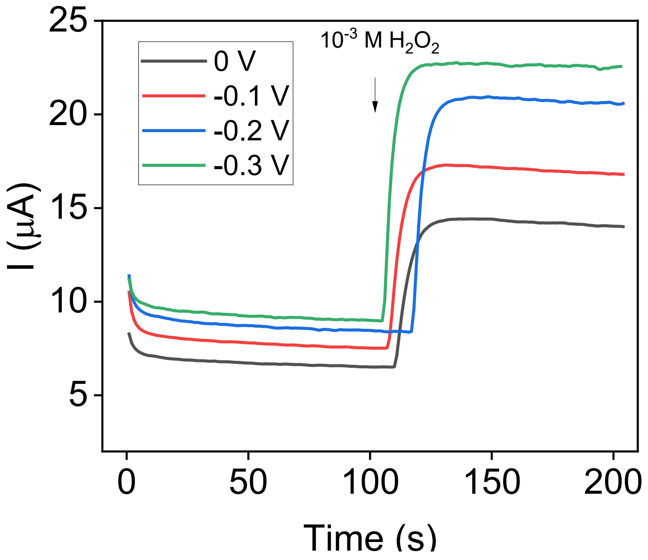

Figure S 7.4. Response of PEDOT:PSS/PtNPs composite to the addition of 1mM of hydrogen peroxide obtained using chronoamperometry at different voltages applied vs Ag/AgCl as a reference electrode, and a platinum wire as counter electrode.

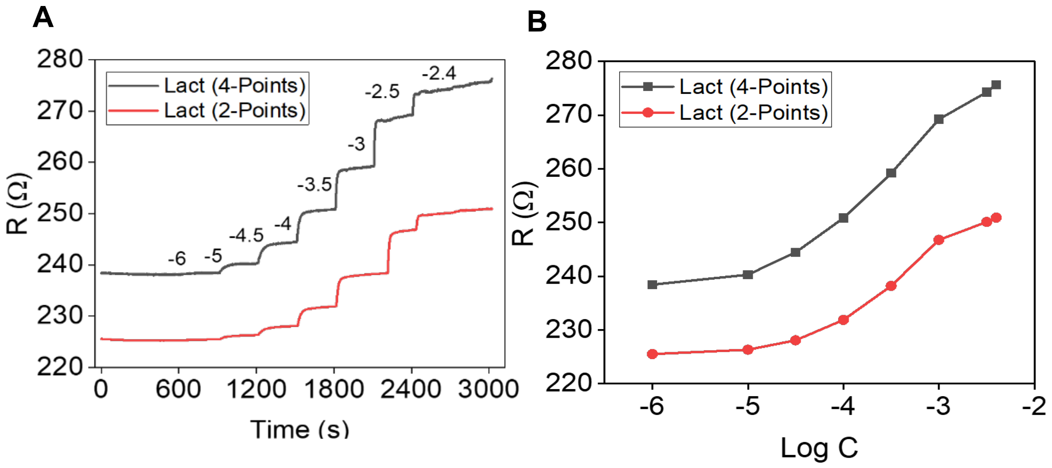

Figure S 7.5. Response of the PEDOT:PSS/PtNPs/LOX/Chitosan chemiresistor to L-lactate, showing A) the time trace of the resistance of the same sensor carried out via 2-point and 4-point methods. B) Resistance against the logarithm of the concentration of L-lactate.

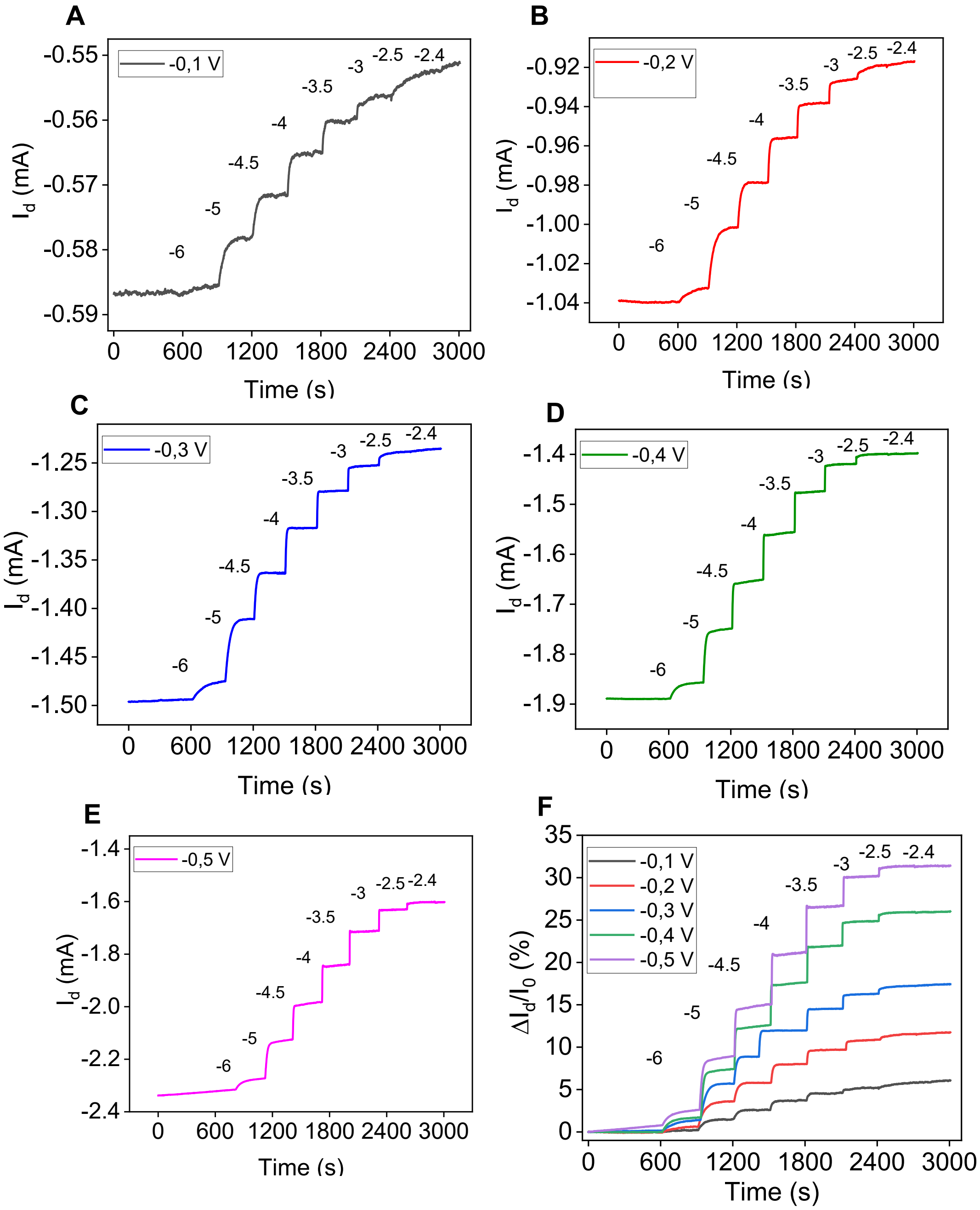

Figure S 7.6. Time response of the PEDOT:PSS/PtNPs /Lox/Chitosan chemiresistor showing the change of the current as L-Lactate is added for 10-6 M to 10-2.4 M, for different voltages applied, A) -0.1 V, B) -0.2 V, C) -0.3 V, D) -0.4 V, E) -0.5 V, and F) time trace displaying the % change in the current.

7.5 References

[1] Seiyama, T.; Kato, A.; Fujiishi, K.; et al., *Anal Chem*, **2002**, 34, 1502-1503.

[2] Ho, K.-C.; Tsou, Y.-H., *Sens Actuators B: Chem*, **2001**, 77, 253-259.

[3] John, A. T.; Murugappan, K.; Nisbet, D. R.; et al., *Sensors (Basel)*, **2021**, 21, 2271.

[4] Song, E.; da Costa, T. H.; Choi, J.-W., *Microsyst Technol*, **2016**, 23, 3505-3511.

[5] Jiang, Y.; Tang, N.; Zhou, C.; et al., *Nanoscale*, **2018**, 10, 20578-20586.

[6] Raguse, B.; Barton, C. S.; Müller, K.-H.; et al., *J Phys Chem C*, **2009**, 113, 15390-15397.

[7] Fratoddi, I.; Venditti, I.; Cametti, C.; et al., *Sens Actuators B: Chem*, **2015**, 220, 534-548.

[8] Kim, S. J.; Koh, H. J.; Ren, C. E.; et al., *ACS Nano*, **2018**, 12, 986-993.

[9] Canovas, R.; Blondeau, P.; Andrade, F. J., *Biosens Bioelectron*, **2020**, 163, 112302.

[10] Kimmel, D. W.; LeBlanc, G.; Meschievitz, M. E.; et al., *Anal Chem*, **2012**, 84, 685-707.

[11] Kim, Y. H.; Lee, K.; Jung, H.; et al., *Biosens Bioelectron*, **2017**, 98, 473-477.

[12] Parrilla, M.; Guinovart, T.; Ferre, J.; et al., *Adv Healthc Mater*, **2019**, 8, e1900342.

[13] Guo, S.; Yang, D.; Zhang, S.; et al., *Adv Funct Mater*, **2019**, 29,

[14] Sharma, S.; Sudhakara, P.; Omran, A. A. B.; et al., *Polymers (Basel)*, **2021**, 13, 2898.

[15] Kaur, G.; Adhikari, R.; Cass, P.; et al., *RSC Advances*, **2015**, 5, 37553-37567.

[16] Zaszczynska, A.; Gradys, A.; Sajkiewicz, P., *Polymers (Basel)*, **2020**, 12, 2754.

[17] Lian, H.; Tang, Z.; Guo, H.; et al., *J Mater Chem C*, **2018**, 6, 4903-4911.

[18] Balamurugan, A.; Ho, K.-C.; Chen, S.-M., *Synth Met*, **2009**, 159, 2544-2549.

[19] Saxena, N.; Čorić, M.; Greppmair, A.; et al., *Adv Electron Mater*, **2017**, 3, 1700181.

[20] Punnoose, D.; Rao, S. S.; Kim, H.-J., *Mater Res Bull*, **2018**, 102, 369-378.

[21] Yu, J. C.; Hong, J. A.; Jung, E. D.; et al., *Sci Rep*, **2018**, 8, 1070.

[22] Mjejri, I.; Rougier, A., *Materials Today: Proceedings*, **2020**, 33, 2470-2473.

[23] Ko, S. H.; Kim, S. W.; Lee, Y. J., *Sci Rep*, **2021**, 11, 21101.

[24] Liu, Y.; Turner, A. P. F.; Zhao, M.; et al., *Biosens Bioelectron*, **2018**, 100, 374-381.

[25] Plekhanova, Y.; Tarasov, S.; Reshetilov, A., *Biosensors (Basel)*, **2021**, 11, 332.

[26] Giaretta, J. E.; Oveissi, F.; Dehghani, F.; et al., *Adv Mater Technol*, **2021**, 6, 1-8.

[27] GIL J. L.; VICENTE V. I.; GUAL G. A.; et al. Alkane dehydrogenation nanocatalyst and process for its preparation. 2022.

[28] Jayakumar, S.; Modak, A.; Guo, M.; et al., *Chemistry (Easton)*, **2017**, 23, 7791-7797.

[29] Morais, R. M.; Klem, M. S.; Ozório, M. S.; et al., *Curr Appl Phys*, **2018**, 18, 254-260.

[30] Benoudjit, A.; Bader, M. M.; Wan Salim, W. W. A., *Sens Bio-Sens Res*, **2018**, 17, 18-24.

[31] Lee, Y. J.; Park, J. Y.; Kim, Y.; et al., *Curr Appl Phys*, **2011**, 11, 211-216.

[32] Nguyen, T. N. H.; Nolan, J. K.; Park, H.; et al., *Biosens Bioelectron*, **2019**, 131, 257-266.

[33] Chang, L. C.; Wu, H. N.; Lin, C. Y.; et al., *Nanoscale Res Lett*, **2012**, 7, 319.

[34] Jayaram, A. K.; Pitsalidis, C.; Tan, E.; et al., *Front Chem*, **2019**, 7, 363.

8 PEDOT:PSS/AgCl Chemiresistor For The Detection Of Chloride

Summary

In this chapter, the PEDOT:PSS channel was sensitized to chloride ions by electrodeposition of Ag nanoparticles and Ag/Cl, which resulted in a PEDOT:PSS/AgCl chemiresistor with enhanced sensitivity. The medical relevance of chloride ions, the working mechanism of the sensor, as well as its key analytical performance are discussed.

8.1 Introduction

Chloride ions (Cl^-) play an important role in supporting critical biological functions of the body. Being the major anion in extracellular fluids, Cl^- contributes in the regulation of key processes such as water balance, acid-base equilibrium, and osmotic pressure[1, 2]. The concentration of Cl^- varies significantly, depending on the nature of the biological fluid. For healthy adults, the typical concentration of Cl^- in sweat is less than 60 mmol/L[3]. In blood plasma, Cl^- is in the range of 96-106 mmol/L[4], while in urine it can be as high as 250 mmol/L[5]. For this reason, measuring the level of chloride ions in blood, urine, and sweat, can be used reliably for diagnosis and post-treatment surveillance purposes.

Indeed, the detection of Cl^- in sweat assists in the diagnosis of cystic fibrosis (CF); a condition associated with the malfunction of transmembrane conductance regulator protein (CFTR) which regulates the flow of Cl^- in and out of cells[6]. Furthermore, monitoring the levels of Cl^- along with creatinine in urine has proven to provide a valuable information for the diagnosis of kidney diseases[7]. Also, an imbalance of Cl^- in biological fluids can point to serious health issues such as alkalosis, hypochloremia, hyperchloremia, diabetes, and heart diseases[8]. Therefore, the development of simple analytical tools that enable the detection and monitoring of Cl^- over a wide range of concentrations can benefit both health professionals and patients.

Numerous analytical methods have been utilized for the detection of Cl^- including chromatography, induced coupled plasma mass spectrometry (ICP-MS), and spectrophotometry[9]. These methods require expensive equipment and are difficult to integrate in portable or point-of-care devices. Electrochemical methods such as amperometry and potentimetry have also been reported for building chloride sensors[10, 11]. Despite this variety of methods, chloride ion-selective membrane electrodes are widely accepted as the standard method for chloride testing in water samples[12]. On the other hand, compared to other platforms, chemiresistors provide an attractive alternative, not only because they have simple design, but also because these devices do not require a reference electrode, and can be easily miniaturized and multiplexed.

In the last decade, PEDOT:PSS/Silver based composites have gained considerable interest, owing to their flexibility, conductivity, transmittance, and catalytic properties. The high transmittance and conductivity of PEDOT:PSS/silver nanowires composites offer an attractive alternative to ITO for building transparent electrodes in solar cells and light emitting diodes[13, 14].For instance, Lim et al. have reported stretchable and transparent PEDOT:PSS/silver nanowires composite that was made by mixing PEDOT:PSS and silver nanowires suspensions[15]. Moreover, PEDOT:PSS/silver nanoparticles have also found applications in chemical sensing. For instance, Song et al. have developed a three-electrode chemiresistive sensor for H_2O_2 detection based on polyaniline-silver nanoparticles composite[16]. The composite was prepared by electrodeposition of the conductive polymer followed by drop cast of the AgNPs suspension. Gualandi et al. have demonstrated an OECT for chloride sensing, where PEDOT:PSS/AgCl composite was utilized to construct the channel and the gate electrode[17]. Bobacka and coworkers studied the potentiometric response of PEDOT:PSS films on glassy carbon before and after conditioning in $AgNO_3$ solution, and found the electrodes showed Nernstian response to KCl[18].

In this work, we have prepared membrane-free chloride sensors based on thick PEDOT:PSS doped with silver and silver chloride nanoparticles. The sensors were constructed by coating a thick film PEDOT:PSS with silver nanoparticles via electrodeposition from a silver nitrate solution. The electrodeposition process in terms of electrodeposition time and conditioning solution were optimized to improve the analytical performance of the sensors. The sensors were tested as chemiresistors (without a gate electrode), as well as OECTs by integrating a Ag/AgCl gate electrode.

8.2 Fabrication and working mechanism of the sensor

Fabrication of the sensor

The chloride sensor was built in three major steps: patterning of the electrodes, drop-cast of PEDOT:PSS, and electrodeposition of Ag/AgCl. First, two gold contacts that will serve as source and drain electrodes were patterned following the protocol described in chapter 3. Secondly, the PEDOT:PSS channel was prepared by drop-casting 3 µL of a commercial PEDOT:PSS aqueous solution (3-4%) on a circular window with 3 mm radius, defining the channel of the sensor. Next, the PEDOT:PSS is left dry for 20 min at 100 ºC.

Finally, silver and silver chloride nanoparticles were successively electrodeposited from a silver nitrate solution and potassium chloride solution, respectively. The electrodeposition of Ag and AgCl was conducted in a three-electrode cell via amperometry, wherein the channel served as the working electrode, a graphite rod was used as a counter electrode, and Ag/AgCl electrode as a reference electrode. The electrodeposition of Ag was achieved by immersing the PEDOT:PSS channels in $AgNO_3$ 0.1 M solution, then, applying a constant voltage of -0.2 V vs Ag/AgCl for different times. Next, the channels were rinsed in deionized water to remove any access of silver that was not well deposited. Next, the same setup was employed to electrodeposit AgCl from KCl (0.1 M) solution by applying +0.5 V for different times.

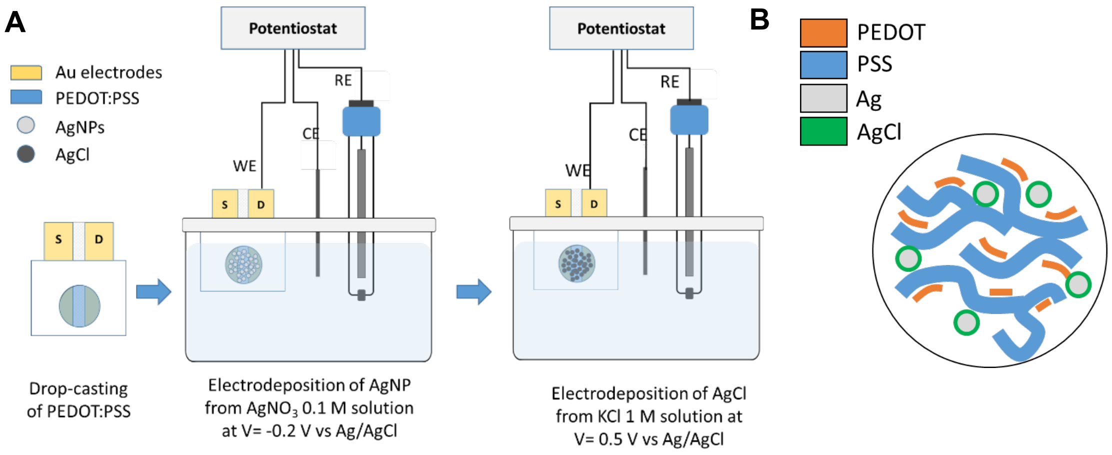

Figure 8.1. A) Fabrication steps of the chemiresistors showing the electrodeposition of Ag and AgCl on the PEDOT:PSS chanel. B) Illustration of the PEDOT:PSS/AgCl composite.

Working mechanism of the sensor

The high conductivity of the PEDOT:PSS/AgCl composite allows the operation of the chemiresistor under a small DC bias (≤ 0.3 V), avoiding the effects of water electrolysis and minimizing signal drift. Figure 8.1 illustrates the proposed working mechanism of the sensor, which is similar to the model reported by Gualandi et al. who expressed the conductivity of PEDOT:PSS/AgCl based OECT in terms of the concentration of Cl^- and the parameters of the conductive polymer[17]. The sensing mechanism of the chemiresistor relies on the detection of chloride ions based on the following reversible redox reactions.

At first, the redox reaction of Ag/AgCl is:

$$\mathrm{Ag_s + Cl^- \leftrightharpoons AgCl_s + e^-}$$ Equation 8.1

$$\mathrm{Ag^+ + Cl^- \leftrightharpoons AgCl_s} \qquad \text{so} \qquad [\mathrm{Ag^+}] = \frac{K_{ps}}{[Cl^-]}$$ Equation 8.2

$$\mathrm{Ag^+ + e^- \leftrightharpoons Ag_s}$$ Equation 8.3

Which allows to write:

$$\mathrm{E_{Ag^+/Ag} = E^0_{Ag^+/Ag} - \frac{RT}{F}\log(\frac{1}{[Ag^+]}) \ = \ E^0_{Ag^+/Ag} - 0.059\log\left(\frac{[Cl^-]}{K_{ps}}\right)}$$ Equation 8.4

Where $E^0_{Ag+/Ag}$ is the formal potential and K_{ps} is the solubility product of AgCl.

A change of the concentration of chloride ions from C1 to C2 (C1<C2) in the vicinity of Ag nanoparticles, induces a small potential difference ΔE that is proportional to the logarithm of the concentration:

$$\Delta \mathrm{E} = \ 0.059 \log\left(\frac{\mathrm{C1}}{\mathrm{C2}}\right)$$ Equation 8.5

On the other hand, PEDOT:PSS is a conductive polymer that demonstrates a high volumetric capacitance, hence, the number of charge carriers injected (n) can be expressed in terms of the volumetric capacitance C_v (F.cm^{-3}) and the bias applied ΔE.

$$\Delta n = \frac{C_v}{e}.\Delta E$$ Equation 8.6

Furthermore, the conductivity of PEDOT:PSS can be written in terms of the number of charge carriers and the charge carrier mobility μ (cm^2.V^{-1}.s^{-1}).

$$\Delta\sigma = \ \mathrm{e}.\mu.\Delta n$$ Equation 8.7

Assuming that the conductivity of the PEDOT:PSS/AgCl composite is mainly determined by the conductivity of the PEDOT:PSS matrix, merging equations 8.5, 8.7 and 8.8 yields the following expression of the conductivity :

$$\Delta\sigma = \ \mathrm{C_v}.\mu \times 0.059 \log\left(\frac{C_1}{C_2}\right)$$ Equation 8.8

It can be seen that a change in the concentration of Cl$^-$ induces a change in the conductivity of the composite.

At constant voltage V, the change in current ΔI can be expressed according to Ohm's law as function of the geometry of the channel (width W, length L, and thickness t) and its conductivity as follow:

$$\Delta \mathrm{I} = \frac{\mathrm{W.t}}{\mathrm{L}}.\mathrm{V}.\Delta\sigma \qquad \text{Equation 8.9}$$

Taking into account Equation 8.9, the change in current ΔI is:

$$\left|\Delta I\right| = 0.059 \times C_v.\mu.V.\frac{W.t}{L}.\log\frac{C2}{C1} \qquad \text{Equation 8.10}$$

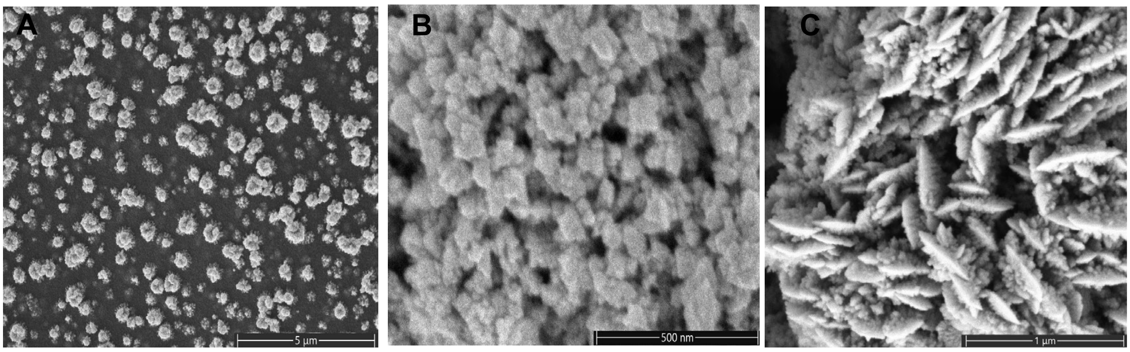

Figure 8.2. SEM images of three PEDOT:PSS/AgNPs composites prepared by electrodeposition of AgNPs and AgCl with different times A) 50 s, B) 200 s and C) 300 s.

8.3 Results and discussions

8.3.1 Morphology of the composite PEDOT:PSS/Ag

The amount and the morphology of Ag deposited can be controlled by adjusting the electrodeposition time of Ag nanoparticles (AgNPs)[19]. To have an insight into the morphology of the composite obtained, Figure 8.2 shows scanning electron microscopy (SEM) images of three PEDOT:PSS/AgNPs composites prepared with different electrodeposition times: 50 s, 200 s, and 300 s. The images show a network of Ag particles that covers the surface of PEDOT:PSST. This network increased in density with the increase of electrodeposition time. For instance, at 50 s, Ag nanoparticles were well dispersed over the entire surface of PEDOT:PSS. At 200 s, although the shape of the nanoparticles remained the same, their density and the size increased significantly, forming a porous layer that covers all the surface of PEDOT:PSS. At 300 s, the growth of the nanoparticles continued all over the PEDOT:PSS surface, leading to the formation of interconnected networks with high porosity. Therefore, depending on the deposition time, the morphology of the PEDOT:PSS/AgCl composite obtained can range between a well-dispersed nanoparticles to a porous network of particles with different sizes. This is in agreement with previous works, where a controlled increase of the electrodeposition time of Ag was shown to result in a complex dendritic morphology [19, 20].

8.3.2 Effect of Ag electrodeposition time on chloride sensitivity

To check how the morphology of the composite affects the sensitivity of the sensor toward chloride, four channels were constructed with different electrodeposition times of Ag (50 s, 100 s, 200 s, and 300 s), while the electrodeposition parameters of AgCl were maintained constant for all channels. In addition, a control channel made of pristine PEDOT:PSS without electrodeposition was also tested. Figure 8.3A represents the time trace featuring the response of the sensors to the addition of Cl$^-$ from 10^{-6} M to 0.1 M. All the sensors that undergone the electrodeposition step showed a decreasing current within the tested concentration range when Cl$^-$ was added, indicating that the channels were sensitized to Cl$^-$.

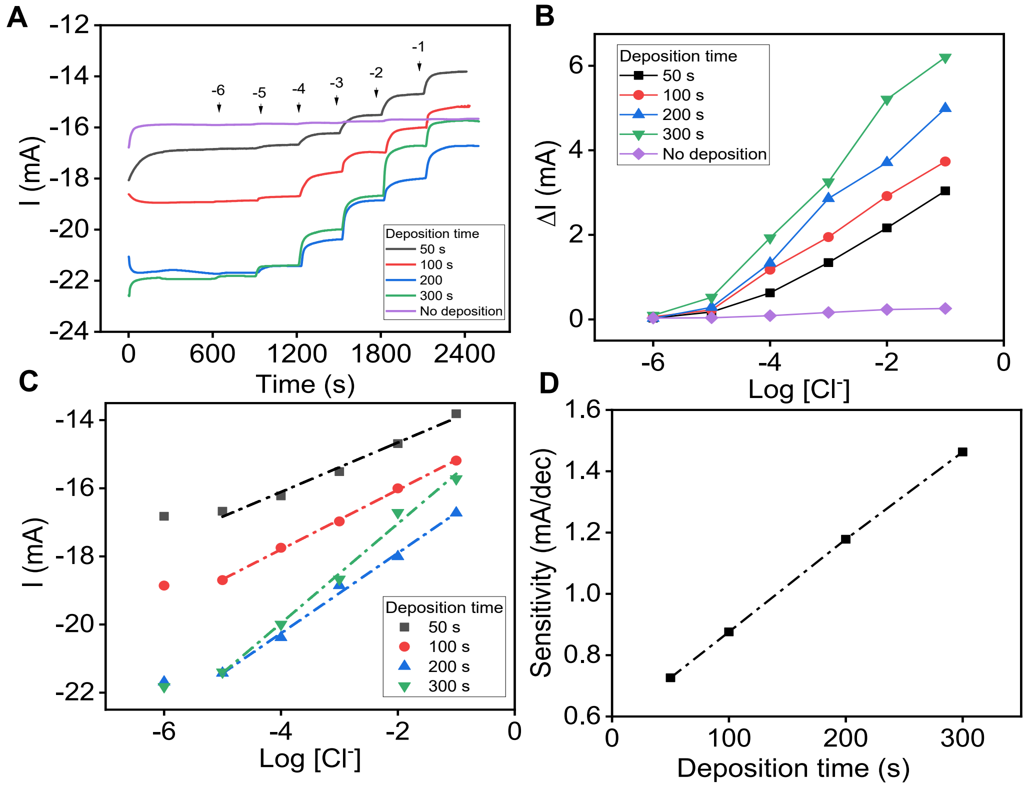

Figure 8.3. A) Time trace of the current I at V = -0.3 V, showing the response to chloride ions of five sensors constructed with different electrodeposition times of Ag. B-C) Corresponding calibration curves showing ΔI and I, respectively. D) Sensitivity of the sensors plotted against the deposition time.

In contrast, the control sensor without Ag/AgCl did not show any significant response, which confirms that the sensitivity of the devices is due to the electrodeposition of Ag and AgCl. Figure 8.3B and Figure 8.3C represent the calibration curves of the sensors, for which the analytical performance are summarized in Table 8.1.

On the other hand, the plot of Cl^- sensitivity against the electrodeposition time of AgCl showed a positive linear relationship (Figure 8.3D). Considering the morphology of AgCl observed for channels with electrodeposition times 200 s and 300 s (Figure 8.2B and Figure 8.2C), we hypothesize that the unique porous networks of AgCl increases the surface area of the sensor, which enables efficient contact with the solution.

Table 8.1. Analytical performance obtained for PEDOT:PSS/AgCl channels constructed with different Ag electrodeposition times.

Ag Electrodeposition time	**Sensitivity mA/dec**	**Linear range**	**R^2**
50 s	0.72	-5 to -1	0.98
100 s	0.87	-5 to -1	0.99
200 s	1.17	-5 to -1	0.99
300 s	1.46	-5 to -2	0.99

8.3.3 Electrodeposition of AgCl

Apart from Ag electrodeposition time, the formation of AgCl can be tuned by adjusting the concentration of KCl solution used for the electrodeposition of AgCl. For this reason, four channels were constructed in the same conditions of electrodeposition times and voltages, but with KCl solutions that had different concentrations (10^{-4} M, 10^{-3} M, 10^{-2}, and 10^{-1} M). Next, each sensor was tested for the detection of Cl^- under constant voltage (V= -0.3 V). As can be seen in Figure 8.4A and Figure 8.4B, all sensors responded to the addition of Cl^- and showed a linear range between -5 and -2/-1. However, the highest sensitivity (1.26 mA/dec) was demonstrated by the sensor prepared using the lowest concentration of KCl solution (10^{-2} M). This behaviour can be explained by the fact that high concentrations of KCl result in the formation of unstable thick/dense layer of AgCl deposited on top of Ag[21], which may hinder the access of Cl^- to the surface of Ag nanoparticles. In contrast, the electrodeposition of AgCl from diluted KCl leads to the formation of a thin layer AgCl, allowing easier access of Cl^- to the surface of Ag, hence, the high sensitivity of the sensor.

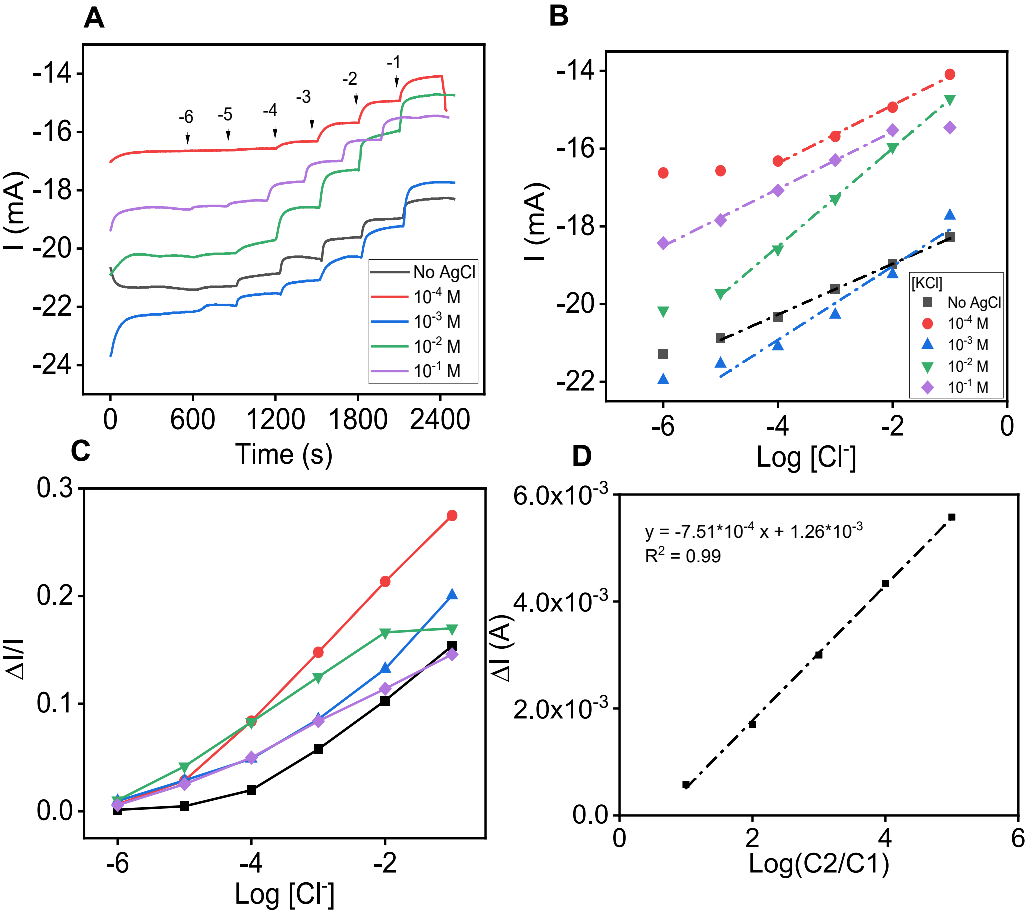

Figure 8.4. A) Time trace of the current showing the response to Cl^- (from 10^{-6} M to 0.1 M) of five sensors prepared with different concentrations of KCl electrodeposition solution, and B) corresponding calibration curves The. C) Normalized response of the sensors as function of the logarithm of [Cl^-]. D) ΔI-Log C2/C1 plot with fitting to Equation 8-9. The slope allows the extraction of Cv.µ.

As Equation 8.10 points out, the response of the sensor to Cl^- can be expressed in terms of the geometry of the channel (W, L, and t), the concentrations of chloride ions C1 and C2, and the product of the volumetric capacitance and the charger carriers mobility (C_v.µ) of the PEDOT:PSS/AgCl composite. Ideally, the plot of the current change ΔI versus Log(C2/C1) is expected to demonstrate a linear relationship, and the slope of the plot allows the extraction of C_v.µ. However, to fit the experimental data, it is necessary to adjust the model by adding a constant (B) that counts for an offset current. Therefore, Equation 8.10 becomes:

$$\left|\Delta I\right| = 0.059 \times C_v.\mu.V.\frac{W.t}{L}.\log\frac{C2}{C1} + B \qquad \text{Equation 8.11}$$

Figure 8.4D depicts ΔI-Log(C2/C1) plot and the corresponding fitting to Equation 8.11. The parameters extracted from fitting the experimental data allow the estimation of $C_v.\mu$, which is calculated to be 27.2 $F.cm^{-1}.V^{-1}.s^{-1}$. It is worth noting that this value is within the range of values reported in the literature for PEDOT:PSS (2 to 47 $F.cm^{-1}.V^{-1}.s^{-1}$)[22].

Table 8.2. Analytical performance obtained for PEDOT:PSS/AgCl channels constructed using different solutions of KCl.

KCl electrodeposition solution	**Sensitivity mA/dec**	**Linear range**	**R^2**
-	0.65	-5 to -1	0.99
10^{-4} M	0.74	-4 to -1	0.99
10^{-3} M	0.95	-5 to -1	0.96
10^{-2} M	1.26	-5 to -1	0.99
10^{-1} M	0.74	-6 to -2	0.99

8.3.4 Detection of chloride in OECT mode

The PEDOT:PSS/AgCl system can also be operated as an OECT by utilizing an external gate electrode. In this experiment, PEDOT:PSS/AgCl channel was prepared in the optimized conditions of Ag electrodeposition time (set to 300 s), and concentration of KCl (10^{-2} M). To evaluate the amplification of the device, the transfer curve was established first by varying V_d from -0.3 V to -0.05 V (0.05 V step), and V_g from -0.1 V to 0.6 V (0.1 V step) in KNO_3. Figure 8.5A and Figure 8.5B depict the time trace of I_d and the transfer curve at different values of V_d and V_g. At constant V_d, the graphs show that I_d decreases with the increasing V_g, which indicates the dedoping of the PEDOT:PSS. Moreover, the maximum transconductance recorded was 49.7 mS at V_d = -0.3 V and V_g = 0.4 V. This value is comparable to the transconductances obtained for OECTs built with only pristine PEDOT:PSS ($g_m \approx 45$ mS), indicating that the migration of cations in and out of the PEDOT:PSS/AgCl film takes place as efficiently as in PEDOT:PSS only. Therefore, the effect of AgCl on the process of dedoping PEDOT:PSS is minimal. Furthermore, the gate voltage at which the maximum transconductance was recorded (V_g = 0.4 V) is slightly higher compared to the voltage applied for pristine PEDOT:PSS channels (V_g = 0.2 V). This shift in V_g and g_m could be attributed in part to the nature of the electrolyte used KNO_3 instead of NaCl. Several works have reported that the cation size affects the performance of OECTs. Under the same operating conditions, cations with small radii such as Na^+, can be injected easily into the channel compared to cations with larger radii (e.g. K^+)[23].

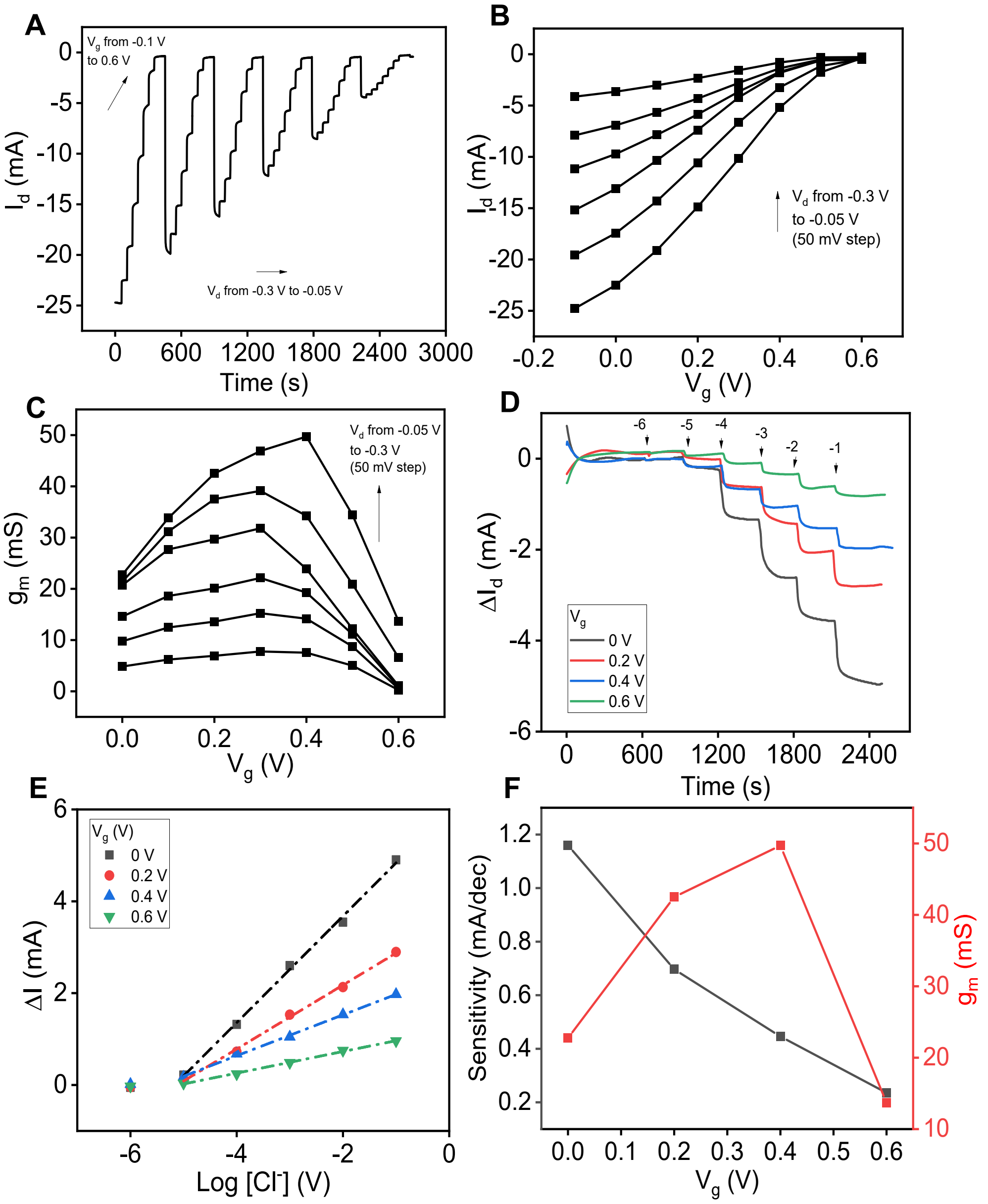

Figure 8.5. A) Time plot of I_d at different V_d and V_g of an OECT constructed with a PEDOT:PSS/AgCl channel (deposition time of AgClNPs set to 300 s) and an external Ag/AgCl gate electrode in KNO_3 (0.1 M). B) Corresponding transfer curve I_d-V_g. C) g_m-V_g plot showing the transconductance of the device at different gate voltages. D) Time trace of Id showing the response of an OECT to an increasing concentration of Cl^- at different gate voltages. The arrows indicate the logarithm of the concentration. E) Corresponding calibration curves of Cl^-. F) Sensitivity to Cl^- and transconductance plots of the device.

Next, the aforementioned OECTs were tested for the detection of Cl^- at different gate voltages in KNO_3 (0.1 M). As represented in the time trace and calibration curves (Figure 8.5D and Figure 8.5E, respectively), all OECTs responded to the increasing additions of Cl^- from 10^{-6} M to 0.1 M by a decrease in the conductivity of the channel, hence, decrease in I_d. Regardless of the gate voltage applied, the devices displayed a linear range between 10^{-5} M and 0.1 M, which suggests that the linear range is independent of the gate voltage. On the other hand, Figure 8.5F shows that the sensitivity of the devices decreased significantly as the gate voltage increased towards high positive values. At V_g = 0 V, the sensitivity to Cl^- was 1.16 mA/dec. while at V_g = 0.6 V the sensitivity dropped to 0.24 mA/dec, which represents a sensitivity loss of 95 %. This loss of sensitivity could be attributed to the ability of Ag/AgCl gate electrode to efficiently de-dope PEDOT:PSS, which reduces significantly the conductivity of the channel and lowers the baseline current. Therefore, in OECT mode, the sensor operates optimally at low gate voltages (V_g = 0 V), while an increase of V_g have negligible effect on the linear range and a detrimental effect on the sensitivity to Cl^-.

8.4 Conclusions

In summary, we have demonstrated simple membrane-free chloride sensors based on thick PEDOT:PSS/AgCl composite. The PEDOT:PSS film was drop-casted while the AgCl was introduced via successive electrodeposition of Ag nanoparticles and AgCl. The optimization of the electrodeposition process has shown that high electrodeposition times of Ag resulted in the formation of porous interconnected AgCl networks on top of the PEDOT:PSS film, while the electrodeposition of AgCl from diluted KCl solution is more suitable for higher sensitivity to Cl-. The sensors showed an excellent sensitivity that exceeded 1.5 mA/dec and a linear range between -5 and -1, which represents an attractive alternative to ion-selective membranes.

8.5 References

[1] Shcheynikov, N.; Son, A.; Hong, J. H.; et al., *Proc Natl Acad Sci U S A*, **2015**, 112, E329-E337.

[2] Yunos, N. M.; Bellomo, R.; Story, D.; et al., *Crit Care*, **2010**, 14, 226.

[3] Hall, S. K.; Stableforth, D. E.; Green, A., *Ann Clin Biochem*, **1990**, 27 (Pt 4), 318-320.

[4] Sonner, Z.; Wilder, E.; Heikenfeld, J.; et al., *Biomicrofluidics*, **2015**, 9, 031301.

[5] Pirkle, J. L. *Laboratory Procedure Manual - Sodium, Potassium, Chloride (Electrolytes)*; 2016.

[6] Macedo, A. N.; Mathiaparanam, S.; Brick, L.; et al., *ACS Cent Sci*, **2017**, 3, 904-913.

[7] Zhang, Z.; Xu, X.; Fan, H.; et al., *BMC Nephrol*, **2013**, 14, 235.

[8] Bandak, G.; Kashani, K. B., *F1000Res*, **2017**, 6, 1930.

[9] Wu, D.; Hu, Y.; Liu, Y.; et al., *Appl Sci*, **2021**, 11, 11137.

[10] Trnkova, L.; Adam, V.; Hubalek, J.; et al., *Sensors (Basel)*, **2008**, 8, 5619-5636.

[11] Choi, D. H.; Kim, J. S.; Cutting, G. R.; et al., *Anal Chem*, **2016**, 88, 12241-12247.

[12] ISO. *ISO 15682:2000 Water quality — Determination of chloride by flow analysis (CFA and FIA) and photometric or potentiometric detection*; 2000.

[13] Li, B.; Ye, S.; Stewart, I. E.; et al., *Nano Lett*, **2015**, 15, 6722-6726.

[14] Liu, Y.-s.; Feng, J.; Ou, X.-L.; et al., *Org Electron*, **2016**, 31, 247-252.

[15] Lim, J. E.; Lee, S. M.; Kim, S. S.; et al., *Sci Rep*, **2017**, 7, 14685.

[16] Song, E.; Choi, J.-W., *J Micromech Microeng*, **2014**, 24, 065004.

[17] Gualandi, I.; Tessarolo, M.; Mariani, F.; et al., *Sens Actuators B: Chem*, **2018**, 273, 834-841.

[18] Oña, J. P.; Mousavi, Z.; Sokalski, T.; et al., *Electrochimica Acta*, **2021**, 390, 138854.

[19] Liang, C. L.; Zhong, K.; Liu, M.; et al., *Nanomicro Lett*, **2010**, 2, 6-10.

[20] Cheng, Z. Q.; Li, Z. W.; Xu, J. H.; et al., *Nanoscale Res Lett*, **2019**, 14, 89.

[21] Suzuki, H.; Ozawa, H.; Sasaki, S.; et al., *Sens Actuators B: Chem*, **1998**, 53, 140-146.

[22] Inal, S.; Malliaras, G. G.; Rivnay, J., *Nat Commun*, **2017**, 8, 1767.

[23] Kumar, P.; Yi, Z.; Zhang, S.; et al., *Appl Phys Lett*, **2015**, 107, 053303.

9 Conclusions And Future Work

9.1 Conclusions

The ultimate goal of the present work was to develop simple and effective approaches for building thick film organic electrochemical transistors and chemiresistors based on PEDOT:PSS and its composites for point-of-need applications. Ease of fabrication, lean design, complexity-free, and user-friendly, among others, are key technical attributes that any point-of-need must demonstrate as off the bench diagnostic and healthcare tool. In chapter 4, thick-film OECTs were constructed via a simple, yet effective off-cleanroom approach, and then characterized electrically and electrochemically. The devices worked at low operating voltages and delivered relatively stable signal. Thick-film OECTs demonstrated an excellent electrical performance in terms of stability, transconductance, On-Off current ratio, and response time. Since these OECT parameters are interdependent, a trade-off must be made between those with upmost relevance for bio- and chemical sensing applications. Thick-film OECTs with low width-to-length ratios (W/L) were found to be relatively more stable, with high On/Off current, low gate current, and a good transconductance. In contrast, despite their excellent transconductances achieved, high W/L OECTs exhibited high gate currents and low and On/Off currents.

In chapter 5, OECTs were constructed through another approach, dip pen, which allowed also the realization of thick PEDOT:PSS films. Compared to drop cast, dip pen technique offered much more control over the thickness of the films obtained, via successive writing-curing cycles. In this way, PEDOT:PSS films with thicknesses up to 20 µm were easily obtained. Our group has mastered the fabrication of potentiometric bio- chemical sensors based on platinum electrodes. By combining this technology with thick film PEDOT:PSS, it was possible to build highly sensitive thick-film OECTs for the detection of hydrogen peroxide and glucose.

The next step, as elaborated in chapter 6, was to enhance the sensitivity of OECTs to H_2O_2 by evaluating two configurations, and explore reducing the complexity of the system by sensitizing the PEDOT:PSS via incorporation of nanomaterials. For this reason, different PEDOT:PSS/nanomaterials composites were introduced in an attempt to impart the conductive polymer with enhanced catalytic properties toward H_2O_2. In this regard, four PEDOT:PSS composites were prepared based on four different nanoparticles platinum, prussian blue, zinc oxide, and reduced graphene oxide. When tested for H_2O_2, PEDOT:PSS/Pt and PEDOT:PSS/PB exhibited good results in terms of sensitivity and linear range. The standard OECTs, where only the gate was functionalized, performed better that the dual OECT where both the channel and gate electrode were functionalized. Although PtNPs demonstrated superior analytical performance, PB and rGO are very attractive since they can provide cost effective alternative to platinum.

Chapter 7 was a direct application of the PEDOT:PSS/platinum nanoparticles chemiresistor to the detection lactate in artificial sweat. The immobilization of lactate oxidase on top of the channel via entrapment in nafion/chitosan provided the sensor with sensitivity to lactate.

In chapter 8, a chloride chemiresistor was constructed by adopting the same approach in the previous work. As result, the electrodeposition of Ag and AgCl nanoparticles on top of pristine PEDOT:PSS thick films sensitized the channel to chloride. The sensor demonstrated excellent analytical performance compared to the work reported in the literature.

9.2 Future work

The organic electrochemical transistor is a promising technology that can put at the service of scientists unique properties for developing novel point-of-need devices for diagnosis and health monitoring. From materials point-of-view, gold is the most common material used to make the electrodes of the device because it has similar work function as PEDOT:PSS ,and it is chemically stable. Despite that the literature is rich with examples of OECTs constructed with non-noble materials, such as PEDOT:PSS itself or carbon ink, their performance, reproducibility, and long term stability are very often a drawback. Screening studies should be conducted to select affordable materials that combine good conductivity, chemical stability, and compatibility with conventional fabrication methods. This is essential to build cost effective devices.

Sensitizing the channel instead of the gate electrode is a very attractive approach, particularly, for building multiplexed systems. In a typical OECT where the gate is functionalized, for instance, the number of electrodes needed to simultaneously detect three analytes would be 9. Whereas, in an OECT with sensitized channel, total number of electrodes required is only 7, since the individual channels will share the same gate electrode. In chapter 6 and 8, the analytical performance of the sensitized channels deteriorated when they were tested as OECTs. More comprehensive studies are needed to understand the mechanism underlying this behaviour, and eventually, minimize it.

Moreover, to further reduce the number of electrodes in a system with multiplexed OECTs, it would be interesting to explore whether it is possible to use one channel and three functionalized gate electrodes covered with membranes that exhibit different diffusion properties. In this way, the time will take the analytes to pass through the membranes will be different. As result, the response of the channel to the individual analytes will be delayed, which makes it easy to distinguish them. Combining this system with chemometrics analysis is also expected to improve the accuracy and ability of the device to provide reliable information.

Appendices

Appendix 1. List of Abbreviations and Acronyms

3Ps	Predictive, preventive and personalized medicines
μ	Charge carrier mobility
AgNPs	Silver Nanoparticles
AuNPs	Gold Nanoparticles
BIPV	Building Integrated Photovoltaics
CE	Counter electrode
CP	Conductive Polymer
Cv	Volumetric capacitance
DNA	Deoxyribonucleic acid
EGOFET	Electrolyte Gated Field Effect Transistor
EIS	Electrochemical impedance spectroscopy
ESEM	Environmental scanning electron microscopy
F	Faraday constant (96485 C/mol)
FET	Field Effet Transistor
GC	Glassy carbon
gm	Transconductance
Gox	Glucose oxidase
Id	Drain Current
Ig	Gate Current
ISM	Ion-selective membrane
IUPAC	International Union of Pure and Applied Chemistry
LOD	Limit of detection
OECT	Organic Electrochemical Transistor
OFET	Organic Field Effect Transistor
OLED	Organic Light Emitting Diode

OPD	Organic Photodiode
OPV	Organic Photovoltaic
OTFT	Organic Thin Film Transistor
PEDOT:PSS	Poly(3,4-Ethylenedioxythiophene) Poly(sodium 4-stryrene sulfonate)
POC	Point-of-care
PON	Point-of-need
PtNPs	Platinum Nanoparticles
R	Resistance
RE	Reference electrode
RFID	Radio-frequency identification
rGO	Reduced graphene oxide
S/D	Source/Drain
THF	Tetrahydrofuran
v	Scan rate
Vd	Drain Voltage
Vg	Gate Voltage
Vp	Pinch-off Voltage
WE	Working electrode
Z	Impedance magnitude
Z"	Imaginary part

Appendix 2. List of Tables

Appendix 3. List of Figures

Appendix 4. Scientific contribution

Publications directly resulting from this doctoral thesis

Adil Ait Yazza, Pascal Blondeau, and Francisco J. Andrade, Simple approach for building high transconductance paper-based organic electrochemical transistor (OECT) for chemical sensing, ACS Appl. Electron. Mater. 2021, 3, 1886−1895.

Adil Ait Yazza, Pascal Blondeau, and Francisco J. Andrade, Chemiresistive sensor based on PEDOT:PSS/Platinum nanoparticles composite for the detection of Lactate in sweat (Manuscript in preparation).

Publications indirectly resulting from this doctoral thesis

Marc Clua Estivill, Adil Ait Yazza, Pascal Blondeau, and Francisco J. Andrade, High-performance ion-selective organic electrochemical transistors for the determination of potassium in clinical samples (Manuscript submitted).

Conference attendance and poster presentation

Adil Ait Yazza, Pascal Blondeau, and Francisco J. Andrade, Chemiresistive sensor based on PEDOT:PSS/Platinum nanoparticles for the detection of lactate in artificial sweat. International Congress on Analytical Nanoscience and Nanotechnology (NyNA 2022), University of Castilla La Mancha, Ciudad Real, Spain, PP 03.